

Lightning inception by Hydrometeors

Citation for published version (APA):

Mirpour, S. (Accepted/In press). *Lightning inception by Hydrometeors: an experimental and numerical investigation*. Eindhoven University of Technology.

Document status and date:

Accepted/In press: 10/09/2021

Document Version:

Publisher's PDF, also known as Version of Record (includes final page, issue and volume numbers)

Please check the document version of this publication:

- A submitted manuscript is the version of the article upon submission and before peer-review. There can be important differences between the submitted version and the official published version of record. People interested in the research are advised to contact the author for the final version of the publication, or visit the DOI to the publisher's website.
- The final author version and the galley proof are versions of the publication after peer review.
- The final published version features the final layout of the paper including the volume, issue and page numbers.

[Link to publication](#)

General rights

Copyright and moral rights for the publications made accessible in the public portal are retained by the authors and/or other copyright owners and it is a condition of accessing publications that users recognise and abide by the legal requirements associated with these rights.

- Users may download and print one copy of any publication from the public portal for the purpose of private study or research.
- You may not further distribute the material or use it for any profit-making activity or commercial gain
- You may freely distribute the URL identifying the publication in the public portal.

If the publication is distributed under the terms of Article 25fa of the Dutch Copyright Act, indicated by the "Taverne" license above, please follow below link for the End User Agreement:

www.tue.nl/taverne

Take down policy

If you believe that this document breaches copyright please contact us at:

openaccess@tue.nl

providing details and we will investigate your claim.

Lightning Inception by Hydrometeors: an experimental and numerical investigation

PROEFSCHRIFT

ter verkrijging van de graad van doctor aan de Technische Universiteit
Eindhoven, op gezag van de rector magnificus, prof.dr.ir. F.P.T. Baaijens,
voor een commissie aangewezen door het College voor Promoties in het openbaar
te verdedigen op vrijdag 10 september 2021 om 16:00 uur

door

Shahriar Mirpour

geboren te Teheran, Iran

Dit proefschrift is goedgekeurd door de promotoren en de samenstelling van de promotiecommissie is als volgt:

voorzitter: prof.dr.ir. G.M.W. Kroesen
1^e promotor: dr.ir. S. Nijdam
2^e promotor: prof.dr. U.M. Ebert
copromotor: dr. H.J. Teunissen
leden: prof.dr. J.R. Dwyer (University of New Hampshire, Physics & Astronomy)
prof.dr. R. Brandenburg (Universität Rostock, Mathematisch-Naturwissenschaftliche Fakultät)
dr. M. Fullekrug (University of Bath, Department of Electronic & Electrical Engineering)
prof.dr.ir. A.J.M. Pemen

Het onderzoek dat in dit proefschrift wordt beschreven is uitgevoerd in overeenstemming met de TU/e Gedragscode Wetenschapsbeoefening.

This thesis was prepared with the L^AT_EX documentation system.
Printed by: Ipskamp, The Netherlands

This project has received funding from the European Union's Horizon 2020 research and innovation program under the Marie Skłodowska-Curie grant agreement 722337.



A catalogue record is available from the Eindhoven University of Technology Library.
ISBN: 978-90-386-5345-7

Copyright © 2021 S. Mirpour

Abstract

Although plenty of studies have been conducted over the years, the question of how lightning is initiated inside thunderclouds is still one of the biggest unsolved problems in lightning physics. The measured ambient electric field of a thundercloud is much lower than that of the well-known electric breakdown field. This thesis treats an experimental and theoretical investigation of discharge inception under different experimental conditions. In the first part, we investigate the role and availability of free electrons in the discharge inception process. Streamer initiation under repetitive pulsed discharges is studied for different gas compositions. In repetitive discharges, an important point is the role of leftover charges that may induce an in-homogeneous charge distribution in the discharge gap that can be source of free electrons production. To address this subject, we measured the inception times for hundreds of pulses which gives us some insights on the temporal and spatial distribution of the free electron sources. Next, we introduced a new method in which a low-voltage pulse is applied between the high-voltage pulses. With this method, we are able to manipulate the leftover charged species distribution in the gap and track its effects on the preceding discharges. The results show that the very first electron for discharge inception can originate from: 1) free electrons or electron detachment from negative ions close to the electrode, 2) a process that liberates electrons from immobile sources, or 3) the drift of a region of negative ions towards the ionization zone. We utilize this method while studying the CO_2 gas discharge as well and find a fundamental difference between the detachment process in CO_2 and air discharges which in CO_2 discharges electrons can be detached in low electric field region while in air discharges detachment occurs in high electric field region.

Next, a theoretical and experimental investigation of streamer initiation in the presence of artificial particles with different shapes is provided to investigate lightning inception near hydrometeors. A hydrometeor is simulated as an individual charged conductor in zero ambient field. In this model, the feasibility of corona inception from ellipsoidal hydrometers can be formulated based on the self-sustaining condition of electron avalanches. In the experimental evaluation, a plane-to-plane setup is used in which an ellipsoidal dielectric (TiO_2 , with dielectric properties close to those of ice) or metal particle is suspended between a pulsed high-voltage and a grounded electrode. We can conclude from the theoretical and experimental results that the streamer onset electric field in the presence of an elongated dielectric or metal particle decreases with the size of the particles and increases with tip sharpness.

Finally, we discuss the inception of streamers from a laser-induced spark. A local spark was created by focusing a high-power laser beam between two flat electrodes. A uniform electric field was applied over this laser discharge, leading to the initiation of a fast, wide, and diffuse discharge above and below the laser focal point. By varying experimental conditions, such as pressure, laser power, and high voltage amplitude, we can conclude that this method is not suitable for replacing traditional point-plane setups, as the streamers induced have very different properties. However, it can still be potentially useful in inducing diffuse streamers with high velocities at specific points in time and space.

All together, this thesis treats the problem of streamer inception by hydrometers to reveal some of the mysteries of lightning inception.

Contents

List of Abbreviations	vii
1 Introduction	1
1.1 Thunderstorms set the stage for lightning	1
1.2 Lightning inception: A very complicated problem	3
1.3 Discharge inception principles	3
1.4 RREA: Relativistic runaway electron avalanche theory	6
1.5 Lightning inception by hydrometeors	6
1.6 Seed electrons	9
1.7 Content of this thesis	10
2 Distribution of inception times in repetitive pulsed discharges in synthetic air	13
2.1 Introduction	14
2.2 Experimental Setup	16
2.2.1 Experimental conditions	16
2.2.2 Measuring inception time t_{inc}	17
2.2.3 ICCD imaging of streamers	18
2.3 Estimate of initial conditions	18
2.4 Simulation Model	22
2.4.1 Particle model	22
2.4.2 Electric field	24
2.4.3 Inception time t_{inc}	26
2.4.4 Drift and reaction times	26
2.5 Results and Discussion	27
2.5.1 Baseline Experiment	27
2.5.2 Baseline theory	29
2.5.3 The first peak	31
2.5.4 The second peak	34
2.5.5 The third peak	37
2.5.6 Streamer inception under different conditions	42
2.6 Summary and open questions	45

3	Investigating CO₂ streamer inception in repetitive pulsed discharges	47
3.1	Introduction	48
3.2	Set-up and Methods	49
3.2.1	Experimental conditions	49
3.2.2	Measuring inception time t_{inc}	50
3.3	Results and discussion	52
3.3.1	Baseline experiment and general phenomenology	52
3.3.2	Drift due to applying an LV pulse	52
3.3.3	Neutralization and ionization during longer LV pulse durations	60
3.4	Summary and conclusion	62
4	Lightning inception by hydrometeors: a numerical approach	65
4.1	Introduction	66
4.2	Model Description	69
4.3	Results and discussions	76
4.3.1	The effects of varying aspect ratio and volume of spheroidal hydrometeors on the corona inception criterion	76
4.3.2	Variation of the corona inception criterion with pressure	81
4.3.3	Dependence of the derived ambient electric field on the aspect ratio for thundercloud pressure	83
4.4	Summary, Conclusions and Outlook	84
5	Lightning inception by hydrometeors: an experimental approach	89
5.1	Introduction	90
5.2	Materials and Methods	92
5.2.1	Experimental conditions	92
5.2.2	Dielectric properties of TiO ₂	93
5.2.3	Inception voltage measurements	94
5.2.4	Streamers thickness and velocity measurement	95
5.3	Results and discussion	96
5.3.1	Streamer inception from particles	96
5.3.2	Streamer development from particles	99
5.4	Summary and conclusions	102
6	Discharge inception from a laser induced ionized patch	105
6.1	Motivation	106
6.2	Setup and Methods	107
6.3	Results and discussion	109
6.3.1	Laser-induced ionized patch evolution	109
6.3.2	Channel discharge initiation from the ionized patch	111
6.4	Summary and Conclusion	113

7 Conclusion	115
7.1 Summary and conclusions	115
7.2 Outlook	119
Appendices	
A Inception probability in air discharges	125
A.1 Analytic estimate for inception probability	126
B Derivations related to the hydrometeors model	127
B.1 Derivation of the distance ρ_0	128
B.2 Derivation of the distance ρ_{ab}	129
B.3 Derivation of the electric field $E(\rho, r, \theta)$	131
B.4 Derivation of the distance r_{max}	133
References	139
Contributions of the author	151
Acknowledgements	153
Curriculum Vitae	155
List of publications and awards	157

List of Abbreviations

t_{inc}	The streamer inception time
\tilde{t}_{inc}	Median of the inception times
HV	High Voltage, referred to the main high voltage pulses
V_{HV}	Main High voltage pulse amplitude
LV	Low Voltage, referred to a low voltage pre-pulse applied before the main high-voltage pulse.
V_{LV}	Low voltage pre-pulse amplitude
$t_{\text{LV}(-\text{dur})}$	Low voltage pre-pulse duration
$t_{\text{LV-sep}}$	Time interval between the low voltage pre-pulse and the main high voltage pulse
<i>Prob</i>	The probability of streamer inception
S	$t_{\text{LV}} \cdot V_{\text{LV}}$
δ	N/N_0 , where N and N_0 are the actual and standard gas densities
\mathbf{E}_k	Breakdown electric field (at STP conditions for air is ≈ 30 kV/cm)
\mathbf{E}_{bg}	Background electric field
\mathbf{E}_0	Onset electric field, the required electric field to initiate a streamer at the tip of the ellipsoidal particle
ρ_{ab}	The distance between the point of photoionization and the symmetry axis of the ellipsoid along the direction of the electric field in the point of photoionization
r_{max}	The distance from the tip of the prolate spheroid to the position where $E = E_k$
K	Ionization integral
C	The volume of the ellipsoidal particles ($= a \cdot b^2$, where a = major axis and b = minor axis lengths)
AR	Aspect ratio = b/a where a = major axis and b = minor axis lengths

1

Introduction

1.1 Thunderstorms set the stage for lightning

Lightning is one of the largest electrical discharge phenomena in nature and is produced by thunderclouds. A typical lightning bolt has an average current of 30 kA, a potential difference of 30 MV, and a total energy of 1 GJ, starting from clouds and extending a few kilometers to the Earth (figure 1.1.a). This discharge develops in different phases. The first phase, which is further discussed in section 1.2, is the initiation of the discharge. Following the initiation phase, self-propagating streamers begin to develop. Streamers are transient type of gas discharges that propagate with fast-moving ionization fronts and can branch during their development [1]. Through the streamer-leader transition, when the ambient electric field is high enough, multiple streamers combine to create a hot and conductive channel called the "lightning leader". When the leader reaches the ground because of the large potential difference between the clouds and the ground, a very high current starts to flow over the established leader channel. In this last phase, known as the "return stroke", we observe a very visible and bright flash [2], [3].

Besides the cloud-to-ground (CG) lightning and ground-to-cloud (GC), there are two other types of lightning: cloud-to-cloud (CC) and intra-cloud (IC); IC is the most common type of lightning [2]. In typical thunderclouds, a positive charge is generally accumulated at the top and a negative charge at the bottom, which means that the electric field in a thundercloud is approximately vertical and directed downward [4]. Lightning usually appears in thunderclouds with an altitude of 2-15 km (in the troposphere). Above this, in the stratosphere, mesosphere, and lower ionosphere, other electrical phenomena can occur. Sprite streamers (figure 1.1.b), blue jets, and elves are examples of transient luminous events (TLEs) that can rarely be seen but are capable of producing electrical phenomena high in the atmosphere [5].

Lightning is also detected on other planets where the atmosphere gas composition and cloud formation process differ from those of Earth. Emissions from electrical discharges during Martian dust storms were first detected by Ruf *et al.* in 2009 [6]. With more or less the same atmospheric composition as that of Mars (about 95 % CO₂), lightning has been detected on Venus as well [7].

Because of the large scale of lightning, it is not possible to recreate this phenomenon in laboratories at full scale. However, the early stage of lightning development, streamers, can be studied in labs. Streamers are produced in a gap with high voltage between two electrodes. Often, one electrode has a pointed tip, connected to the high voltage, and the other, a flat plate or pin electrode, is connected to the grounded electrode [1].



Figure 1.1: a) CG lightning strokes near Milad tower [8] b) red sprites above thunderstorm clouds [9] c) streamers in the laboratory conditions. To watch them in action with a high frames per second rate, scan the QR code right below the images. Note that the videos are published by different authors than the figures.

1.2 Lightning inception: A very complicated problem

In the lightning scientific community, "lightning inception" is considered as the one of the most difficult unsolved problems in lightning physics. For the first time, this controversial topic arose in 1945 because of the measurements of a B25 airplane from active thunderclouds which showed that the maximum ambient electric field is not higher than 0.4 MV/m [10]. This is far less than the classical breakdown threshold, E_k , which is 1.5 MV/m at 500 mbar (a typical altitude for lightning inception [11]). Later, more sophisticated balloon measurements confirmed the previous claims: no measured electric field was higher than 1/5 of E_k [12], [13]. And that was the beginning of the problem. Before going deep into the challenge, one issue that may arise here is that invasive in-situ devices (balloons, rockets, aircraft, etc.) have been used for electric field measurements. Furthermore, not all measurements were taken during lightning strike occurrence. Recently, indirect VHF emission measurements from the discharge region at an altitude of 9.5 km showed an average pre-breakdown ambient electric field of 0.1-0.15 MV/m [14]. **In another study [15], SEVAN particle detectors were used to measure the particle-flux rates of electrons, gamma rays, and muons that arrived at detectors during thunderstorm activity. The study established a correlation between the electric field strength and changes in particle-flux acceleration and found that, at an altitude of 3 km, the maximum strength of the potential difference is about 500 MV.**

1.3 Discharge inception principles

The main component in discharge inception is the electron avalanche process. In an electric field, electrons start to accelerate and gain energy. As the electrons drift, they experience direct impact with neutral molecules and atoms. If the energy is high enough, the transferred energy from the electron collision will ionize the neutral molecules, meaning that the neutral molecules can release electrons and become ionized with an ionization coefficient α . The liberated electron can produce another electron in the same manner. However, electrons are not only produced by ionizing collisions but also lost by attachment processes to neutral molecules, forming negative ions. If electrons attach with an attachment coefficient of η , then $\alpha > \eta$ leads to an increase in the number of electrons and consequently an electron avalanche. The critical electric field, E_k , is defined as the field where $\alpha = \eta$ [16]. The ionization region (zone) is defined as the region where the electric field is

higher than the critical electric field ($E > E_k$). α and η depend on the electric field and pressure for each gas composition; hence, both are described as a function of the reduced electric field (E/N). Excited molecules can be produced from electron impact with neutral molecules in an avalanche and consequently emit photons. In air, these photons can photo-ionize other gas molecules, meaning that the gas molecules absorb the photons and liberate electrons (photo-ionization). In the ionization region, the primary electron avalanche is the first group of electrons that collide with gas molecules, produce required photons for photo-ionization process. The secondary group of electrons that are generated from photo-ionization is known as the secondary electron avalanche. An inception process is self-sustained when the number of electrons created by primary and secondary avalanches is equal. This criterion was introduced by Naidis *et al.* [17] for spherical conductors and later extended to various pressures and humidity levels by [18] (figure 1.2) .

When the number of electrons in an avalanche reaches a critical value, the left-behind positive space charge can give rise to an additional electric field, causing the positive charge to grow and drift in the direction of the electric field. This is called a "streamer" [16]. This critical value was quantified by Meek [19]. His criterion states that an avalanche-to-streamer transition will take place when the positive ion space charge density is equal to K . The value of K can be obtained by evaluating the following integral:

$$\int_0^x \alpha_{eff}(z) dz, \quad (1.1)$$

where x is the distance which the avalanche can travel and $\alpha_{eff} = \alpha - \eta$ is the effective ionization coefficient. The Meek criterion has been revisited using diffusion correction by Montijn *et al.* [20]. Furthermore, Dubinova in [21] showed that Meek number of 10 around a dielectric body is sufficient for streamer initiation.

Streamers can propagate with a positive ion front (positive streamers) or electron front (negative streamers). A positive streamer moves in the direction of the electric field E . The mechanism of propagation is as follow: electron avalanches develop towards the streamer head and leave behind a region of positive ions, neutralizing the head. Now the positive region is the new streamer head and this process repeats, leading to the propagation of positive streamers in the direction of the electric field. In this mechanism to initiate electron avalanches, positive streamers need electron source in front of them. A possible way to produce free electrons is the photo-ionization process. The excited molecules in the positive streamer head emit energetic photons, which leads to photo-ionization of front-head neutral molecules. With this process, an electron can liberate from neutral and initiate

an electron avalanche. For negative streamers, the streamer head constitutes a surplus of electrons and propagates in the opposite direction of the electric field [1]. It should be noted that photo-ionization process is also occurring in negative streamers, however, since they propagate with electrons, it is not so essential as it is for positive streamers.

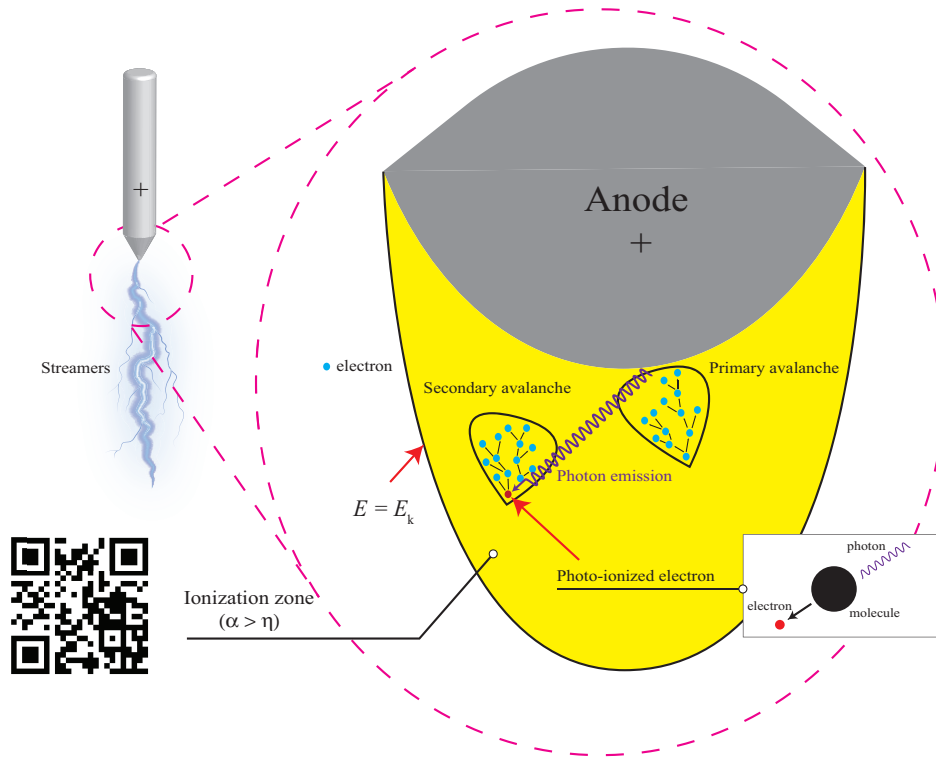


Figure 1.2: Streamer initiation from a positive sharp tip electrode (anode) based on the Naidis criterion [17]. To watch a video abstract of inception process scan the QR code.

Thus, to initiate a discharge, two main components are crucial: **electric field enhancement over a large enough distance** (to satisfy $E > E_k$) and the **availability of free electrons**. In thunderclouds, a mechanism is needed for field enhancement to increase the ambient electric field by 10 times. Griffiths and Phelps in 1976 [22] suggested a model that describes a system consisting of a few successful positive streamers and can lead to a significant electric-field enhancement at their origin. Though their model is still one of the most plausible hypotheses for the lighting-inception problem, one question remains unanswered: *How is the first streamer initiated under sub-breakdown conditions?* Here we introduce two available theories: lightning inception by RREA and by hydrometeors.

1.4 RREA: Relativistic runaway electron avalanche theory

Electrons can gain energy through an electric field and accelerate within this field. They can also lose energy through collisions, a process often called air friction. In this balance, when the average energy gain exceeds the average losses, which happens for electric fields $E_{RREA} \approx 0.285 \text{ MV/m}$, the electron can "run away" in the field and gain large amounts of energy [23]. A recent correction on the classical friction curve by Diniz *et al.* [24] using a Monte Carlo approach showed that when the field is close to 30 MV/m , electrons can reach energies of 1 keV which is enough to overcome the barrier and run away in the field. The signature of runaway electrons was predicted in 1925 by Wilson, who found that electrons can gain a large amount of energy through a static electric field via this mechanism [25]. Many years later, Gurevich *et al.* [26] suggested that runaway electrons, because of their high energy, can initiate an avalanche process through electron-air collisions and referred to it as the relativistic runaway electron avalanche (RREA) process. Because this process can occur in fields relatively close to thundercloud electric field, RREA was a major candidate for lightning inception. However, it was associated with some issues. The main issue was that RREA requires distances on the order of a kilometer for a significant increase in runaway electrons. Dwyer in two famous papers [23], [27] proposed another form of the RREA mechanism in which feedback positrons produced in the head of an avalanche can drift back in the opposite direction of avalanche growth and initiate a secondary avalanche (Figure 1.3). This process can sustain the avalanche on a relatively small scale. This scenario may solve the length problem, However, it opens up another challenge: discharge propagation velocity in this model is an order of magnitude lower than hydrometeor-initiated positive streamer development speed [28].

Testing this mechanism in the laboratory is very challenging because of the small gaps available in the experimental setups. One of the only efforts in this case is Kochkin [29], where 300 keV electrons produced in a meter-scaled gap discharge were detected using a 1 MV Marx generator.

1.5 Lightning inception by hydrometeors

Above, we stated that a mechanism is needed to enhance the ambient electric field to initiate a streamer. Hydrometeor-assisted field enhancement can offer a solution. Hydrometeors are water droplets or ice particles with a large distribution

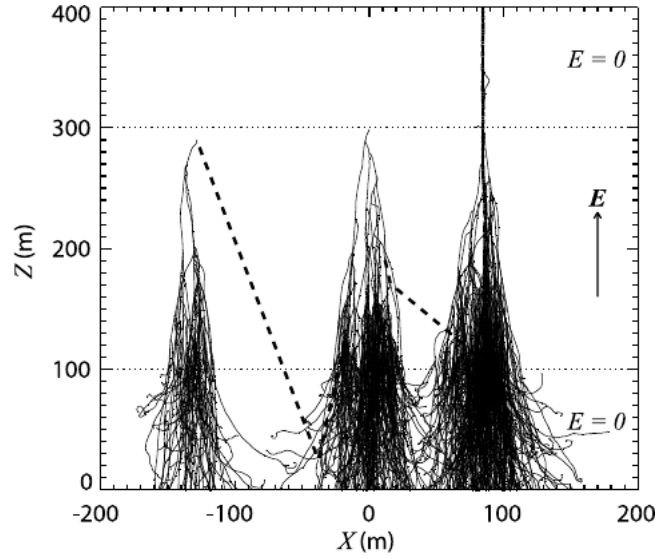


Figure 1.3: Partial results of the Monte Carlo simulation that show the relativistic feedback mechanism developed by Dwyer. Image from [30].

in size and density. They are key elements for the electrification mechanism during thundercloud development [31]. Because of the high dielectric permittivity of ice ($\epsilon = 90$ at low frequencies), the electric field can be enhanced in the vicinity of a hydrometeor tip, possibly exceeding E_k . Loeb in 1966 [32] suggested hydrometeors as possible candidates for field enhancement in thunderclouds. At that time, a major challenge was the hydrometeor shape. Spherical hydrometeors are not sharp enough to enhance the field at the edges by 10 times. Hence, hydrometeors with elongated shapes or other mechanisms might be needed, such as colliding raindrops as proposed by Crabb *et al.* [33]. The latter was a result of an experimental study showing that collisions of water droplets can decrease the breakdown of the electric field below 0.35 MV/m. Though all the hypotheses seem to shape plausible theories for lightning inception by hydrometeors, Griffiths [34] demonstrated that below -18°C , the corona current decreases by three orders of magnitude (no more than $10\ \mu\text{A}$) which is not enough for streamer initiation. This could lead to the rejection of all previous theories because the actual temperature in thunderclouds at high altitudes is far below -18°C [35].

This knot was untied about 30 years later by Petersen *et al.* [36], who used a laboratory investigation to show that positive streamers can be initiated from ice crystals at temperatures as low as -38°C . Multiple streamers produced at such low temperature are enough to start the streamer system mechanism described by Griffiths and Phelps [22]. Apparently the concern related to temperature is unnecessary and gives us hope that streamer initiation from hydrometeors is a plausible theory. Now it is time to challenge that by in-situ thunderclouds observations.

The first convincing evidences of lightning initiation by hydrometeors has been presented by Rison *et al.* [37] who observe very fast ($\approx 4\text{-}10 \times 10^7 \text{m/s}$) positive streamers. These fast positive streamers trigger a structure dubbed a "Narrow Bipolar Event (NBE)" close to the place where hydrometeors are located within the thunderclouds. They conclude that the initiation of all lightning flashes starts with an NBE. Later, Marshall *et al.* [38] argued that paper stating that not all lightning flashes are initiate by an NBE but most of them are initiated by much shorter and weaker events. In a recent paper by Kostinskiy *et al.* [39], they observe that if hydrometeors are able to enhance the electric field to $E \geq 3 \text{MV/m}$, they can be a candidate for the inception, otherwise small-scale hydrodynamic instabilities can initiate positive streamer flashes. As we already know, field enhancement near hydrometeors depends on the hydrometeor shape and length which need to be clarified.

Therefore, the dependency of the inception field on hydrometeor shape and size is an important matter. Dubinova [21] modeled streamer inception near ellipsoidal ice particles and found that a thin and elongated hydrometeor can decrease the inception electric field to $0.15 E_k$. They showed that the requirements for hydrometeor size and shape resulting from the modeling is very close to the approximate distribution of ice particles in real thunderclouds. Furthermore, according to their modeling, streamer development is faster with a fixed dielectric constant of 93 than it is with ice, where at higher frequencies ($\approx 10^4 \text{Hz}$) the dielectric constant decreases to about 3. In line with Dubinova's results, Peterson *et al.* in a laboratory investigation with real ice crystals showed that longer and sharper crystals required a lower externally applied electric field to initiate a positive streamer [40]. However, more controllable ice crystals with respect to the size and shape were demanded for such research. For instance, artificial hydrometeors produced from metal or dielectrics can be an option. This idea was employed in the hydrometeor-based lightning inception experiments where researchers used an array of spherical conductors suspended in an induced electric field [41], [42]. Mazur *et al.* [41] observed bipolar leader formation from suspended metal balls where positive streamers were initiated first, followed by negative streamers. The authors did not report any results about the streamer initiation and development phases. Petersen in an unpublished PowerPoint file [43] proposed using a large parallel-plate electrode gap with suspended simulated ice crystals. In line with the previous suggestions we aimed to test the Dubinova modeling in a laboratory using **suspended artificial ellipsoid hydrometeors between two parallel-plate electrodes** (see figure 1.4).

Now we have a theory on field enhancement near hydrometeors, but we should not forget the second most important component in a discharge initiation: seed electrons.

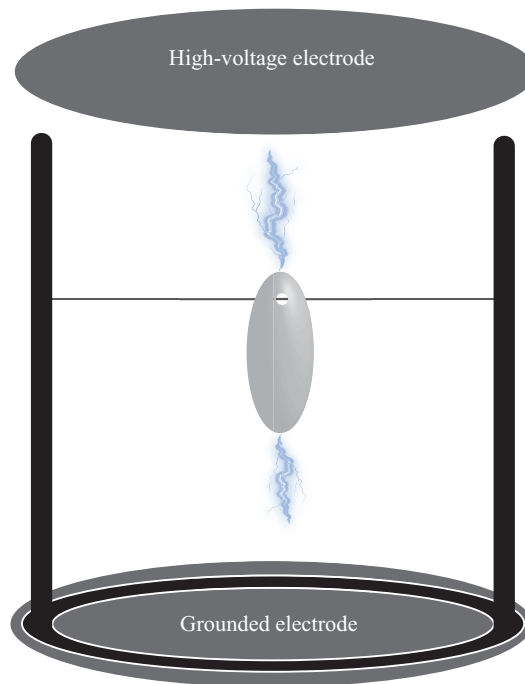


Figure 1.4: Idea of using ellipsoid dielectric particles suspended between two plane electrodes to test lightning inception by hydrometeors theory.

1.6 Seed electrons

Having at least one initial electron to start a discharge inception is a must. Without such a seed electron, it is impossible to initiate a discharge even if the electric field is far above E_k . The first thought about the source of free electrons in thunderclouds would be cosmic rays. These are energetic particles originating from outer space which can liberate electrons from gas molecules via direct impact. However, the average electron density created by such events is low (1 m^{-3}). Moreover, the fast attachment ($<100 \text{ ns}$, see chapter 2 - section 2.4.4) of electrons to O_2 molecules quickly eliminates free electrons from the environment. Rutjes [44] introduced another mechanism in which extensive air showers can provide these free electrons with a density of 100 cm^{-3} . These are enough electrons to initiate discharges near hydrometeors. Lowke proposed electron detachment from metastable O_2 as another possible electron source for the inception process [45]. At a much lower altitude than thunderclouds, in the laboratory, we have a different situation and perhaps an easier job to find free electrons. In addition to cosmic rays, other sources like radioactivity and detachment from negative molecules can also provide free electrons in experimental setups. Without these, discharges are unlikely to be initiated, but then we also can use a UV lamp to liberate electrons from metal surfaces and thereby start discharges more easily. Usually, streamer experiments

are done under repetitive pulsed discharge conditions. This can induce another effect in which long-lived species left over from one discharge could influence the subsequent discharge inception. In the literature, this is called the "memory effect". The memory effect may depend on various parameters such as applied voltage conditions and gas composition. We can trace the footprint of this effect on the measurement of streamer inception time, which is sometimes referred to as a "jitter" or "delay" in the literature. Though we expect to observe stochastic behavior in discharge inception with a large jitter, the charged species created during repetitive pulses can induce localized charged patches that can produce electrons and break the randomized nature of inception.

Hence, this thesis aims to 1) investigate the possible sources of free electrons in repetitive pulsed discharges in synthetic air and CO₂ gas. This will give us insight on how memory effect influences the discharge inception in different gas composition. 2) present a detailed numerical and experimental evaluation on the lightning inception by ellipsoidal hydrometeors theory.

1.7 Content of this thesis

This thesis is set up in 5 chapters. Chapter 2 and 3 focus on streamer inception in repetitive-pulsed discharges. Chapter 2 focuses on discharge inception in point-to-plane geometry in synthetic air and compares the experimental results with modeling. The modeling of this work was performed by M.S. Andy Martinez from Centrum Wiskunde & Informatica (CWI). We found a huge discrepancy between modeling and experimental results, which apparently originated from the memory effect in repetitive pulsed discharges that were not implemented in the modeling. This leads us to establish a novel and original experimental method that enables us to manipulate the leftover charges between two high-voltage pulses.

In chapter 3, we use the idea of the previous chapter to investigate the sources of free electrons in CO₂ gas. This gas has a large number of applications in industry as well as in fundamental science, for example related to streamers on Mars and Venus. The experiments gave unexpected results as we found a big asymmetry in results when the applied voltage bias polarity was inverted. Later, we found that it occurred mostly because of different gas chemistry and detachment procedures between air and CO₂.

Chapter 4 analytically investigates discharge inception near hydrometeors. This chapter was developed in collaboration with B.S. Silke Peeters. We extended the hydrometeor discharge inception model introduced by Naidis [17] for ellipsoidally

shaped hydrometeors. The results of this chapter enable us to enhance our knowledge on the influence of the shape and size of hydrometeors on the inception criteria.

Chapter 5 targets the main question proposed in this thesis. We suspended a ceramic dielectric particle with a dielectric profile similar to that of ice, between two parallel electrodes. We studied the inception voltage and streamer development parameters and compared them with those of the metal particles. The results of this chapter can provide a great deal of information related to the lightning inception problem.

In chapter 6, we investigate streamer inception from laser-induced ionized patch. The main aim of this chapter is to create an ionized patch using a powerful laser between two parallel electrodes. When the electric field is applied over the gap, we expect to observe streamers initiated from the ionized patch. This work was performed in collaboration with M.S. Wouter Slot. One of our goals was to bridge the gap between modeling and experimental works because, in the most of the streamer modeling studies, streamers are initiated from an ionized patch, whereas in experiments streamers are initiated from a pin electrode.

2

Distribution of inception times in repetitive pulsed discharges in synthetic air

Abstract

Knowing which processes and species are responsible for discharge inception is important for being able to speed up, delay, or completely avoid it. We study discharge inception in 500 mbar synthetic air by applying 10 ms long 17 kV pulses with a repetition frequency of 2 Hz to a pin-to-plate electrode geometry with a gap length of 6 cm. We record inception times for 600 pulses by measuring the time delay between the rising edge of the high-voltage pulse and the signal from a photo-multiplier tube. Three characteristic time scales for inception are observed: 1) 20 ns, 2) 25 μ s, and 3) 125 μ s. To investigate the underlying processes, we apply a low-voltage pulse in between the high-voltage pulses. These low-voltage pulses can speed up or delay discharge inception, and our results suggest that the three time scales correspond to: 1) free electrons or electron detachment from negative ions close to the electrode, 2) a process that liberates electrons from (quasi)-neutrals, and 3) the drift of an elevated density of negative ions to the ionization zone. However, each of these explanations has its caveats, which we discuss. We present a theoretical analysis of the distribution of inception times, and perform particle simulations in the experimental discharge geometry. Some of the observed phenomena can be explained by these approaches, but a surprising number of open questions remain.

This chapter is based on [S.Mirpour, A. Martinez, J. Teunissen, U. Ebert, and S. Nijdam. "Distribution of inception times in repetitive pulsed discharges in synthetic air." *Plasma Sources Science and Technology* 29.11 (2020): 115010.]

2.1 Introduction

The properties of streamer discharges (velocity, electric field at the tip, electron/ion densities in the body and at the tip, branching, etc.) have been widely studied, see e.g. [1], [46]–[53]. Streamers are important in various fields like high-voltage engineering, atmospheric discharge phenomena (e.g. lightning), etc. The streamer inception voltage and the influence of the voltage rise time on this inception voltage were studied in [54]–[56]. Briels *et al.* [57] used time resolved optical measurements to investigate the inception of positive streamers in air. The analysis was focused on the streamer inception voltage and the reduced streamer diameter. Nevertheless, the current understanding of the complex interplay of factors governing streamer inception is still very limited. In the present work we investigate the streamer inception process in more detail.

As shown in figure 2.1, a positive streamer discharge can start when the electric field around a conductor or dielectric rises, free electrons move opposite to this field and travel towards positively charged tips or electrodes. When these electrons enter a region where the electron impact ionization rate is greater than the electron attachment rate they can form an avalanche. The electrons replicate rapidly due to direct impact ionization until the electron density becomes so high that space charge effects become important. The avalanche(s) can then transform into a streamer discharge. The so-called Meek criterion [20], [58] is an estimate for the number of electrons required for this avalanche-to-streamer transition.

We can identify several questions related to streamer inception: Where do the streamer-starting electrons come from? What can the inception time between an applied high-voltage and the start of the streamer discharge tell us? Are there ways to manipulate the inception of a streamer discharge without changing quantities like pressure, gas composition, applied high-voltage? Answers to these questions can be useful in high-voltage engineering applications where the inception of streamer discharges is unwanted or better control over the streamer development is needed. Somewhat related is a more poorly understood fundamental question [28], [59]: How does lightning initiate inside thunderstorms when the background electric field is below breakdown? A big difference with lightning inception and repetitive pulse discharge inception is that lightning inception is not a repetitive process. Nevertheless, answering the posed questions in a lab setting with a repetitive pulse is a first step towards better understanding of the lightning inception process.

Streamer-starting electrons can be provided by a cosmic ray ionization event, by radioactivity from surrounding material, by gas specific electron sources, and by

charges in the gap leftover from previous discharges. For N_2/O_2 -mixtures, processes like detachment from O_2^- and O^- [60]–[62], can provide electrons to start a streamer discharge. Li *et al.* [63] investigated how the time between two high-voltage (HV) pulses influences positive streamer inception and propagation. It was found that for short times between two HV pulses positive streamers starting on the second pulse would follow the paths of the streamers developed during the first pulse. The general physical mechanism is understood, but the mechanism that provides electrons for these second-pulse streamers is not clear yet.

The time delay between applying an HV pulse to an electrode and the inception of a streamer discharge was investigated by Wang *et al.* [55]. They split the streamer inception time into two components: the time to reach the inception voltage, and a statistical time delay due to the random nature of having an electron in the right circumstances to trigger a discharge. They conclude that the density and lifetime of O_2^- are the two main factors that determine the statistical delay, and that the statistical delay using a positive lightning impulse voltage follows a Rayleigh distribution.

Fengbo *et al.* [64] investigated the voltage recovery rate in spark gaps. They developed a repetitive nanosecond pulse source and found that by applying a +1 kV DC bias between two high voltage pulses to their trigger electrode they could reduce the effect of residual electrons in the discharge gap. This reduction increased the voltage recovery rate of the pulse source. Moreover, they showed that a higher DC bias voltage does not change the voltage recovery rate because of the shielding effect around the electrode. Zhao *et al.* [65] investigated the influence of memory effect agents on the streamer evolution in a nanosecond repetitive discharge. They showed that by applying a superimposed DC voltage bias the number of pulses required to get breakdown is reduced. This is further reduced by increasing the DC bias until a minimum is reached. They stated that at high HV repetition frequency the electrons are attracted towards the anode by a positive DC bias. At low repetition frequency, they showed that the number of pulses before breakdown decreases. Also, they observed that the inception moment is delayed under a negative DC voltage bias.

In this work, we have taken these prior investigations as a basis for new advanced experiments and numerical models. These will give a more detailed insight into the relevant mechanisms and species involved in the inception of repetitively pulsed discharges in synthetic air. We experimentally studied the statistical distribution of the inception time (t_{inc}) and how this distribution can be manipulated. We have detected three distinct peaks in the distribution of t_{inc} which implies three different processes for triggering a discharge in the experiment.

We also found that the histogram of inception times t_{inc} could be manipulated by applying a low-voltage (LV) pulse between two HV pulses. This LV pulse influenced the residual charged species in the discharge gap. This method allowed further investigations of the processes responsible for each peak in the t_{inc} histogram. We investigate possible sources of the three peaks: free electrons or quickly detached electrons from negative ions, Penning ionization, and drift of negative ions to the ionization zone.

A particle model for the electrons with Monte-Carlo based collision sampling (MCC) was used to further substantiate the arguments made for the sources of each peak in the t_{inc} histogram. The particle model is described in [66] except that in the current investigation of the avalanche phase, the electric field does not change in time. We have also tracked O_2^- as particles drifting in the electric field and eventually detaching electrons.

This chapter is organized as follows: In section 2.2 we describe the experimental setup, applied conditions, and diagnostic methods. Section 2.3 discusses estimates of initial conditions for the simulation model. Section 2.4 explains the simulation model. Section 2.5 shows the results and discussion of the baseline experiment and different variations of the LV pulse parameters (polarity, width, and time between it and the HV pulse). Finally, in section 2.6 we summarize the chapter and list the open questions.

2.2 Experimental Setup

2.2.1 Experimental conditions

All experiments in this study are performed with a point-to-plane electrode geometry (shown in figure 2.2) in which the electrodes are separated by a distance of 60 mm. The powered electrode, anode (with a tip radius of about 100 μm), is connected to the HV circuit which consists of an HV solid state push-pull switch (Behlke HTS 301-10-GSM) and a 200 pF capacitor. This produces voltage pulses with amplitudes of 17 kV, pulse widths of 10 ms, and rise times of about 40 ns. The pulses were applied with a repetition rate of 2 Hz. We chose this frequency to have a shorter acquisition time. The background pressure level in the vessel was 1 mbar and the working pressure was 500 mbar. Synthetic air (80% N_2 + 20% O_2) with less than 1 ppm impurity was used. The humidity level outside of the vessel was measured at around 47%. During the entire experimental period the vessel was kept closed. We have not seen any noticeable changes in the tip curvature and the obtained results were well reproducible (the baseline experiment was the same in each experiment).

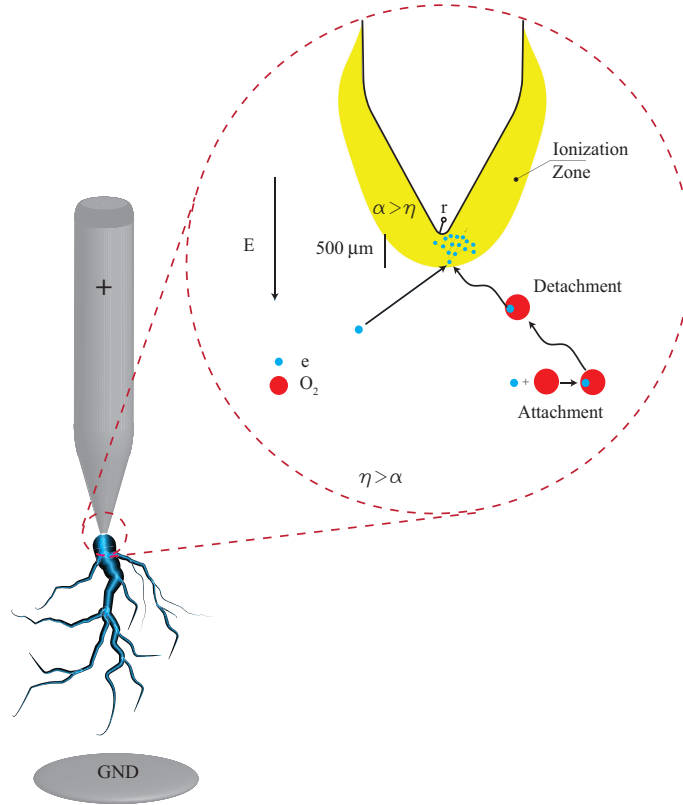


Figure 2.1: The inception process in which a free electron or an electron detached from a negative ion can enter the ionization zone and trigger the inception process (not to scale, $r = 100 \mu\text{m}$). α and η represent the ionization and attachment coefficient respectively.

To study how residual charges influence the streamer inception, in most experiments we applied an LV pulse between each two HV pulses. This was possible via a second custom-built push-pull switch which can apply a bias to the negative side of the HV switch. With that, we were able to make a bias with variable voltage (V_b), width ($t_{\text{LV-dur}}$), and time before the HV pulse ($t_{\text{LV-sep}}$). In the case of $t_{\text{LV-sep}} = 0$, the LV pulse attaches to the HV pulse. The applied V_b was always plus or minus 300 V.

2.2.2 Measuring inception time t_{inc}

A photo-multiplier tube (PMT, Hamamatsu H6779-04) was placed behind a window of the vessel to capture photons produced by the discharge around the anode tip. The PMT has a response time of less than 2 ns (according to the datasheet) and can measure the photons emitted in the inception process. The output signal was collected by a 12 bit HD 6104 Teledyne Lecroy oscilloscope with a maximum sample rate of 500 MS/s. Such a measurement was generally done for 600 cycles per setting. We consistently observed only one inception for each 10 ms HV pulse. From these results we established for each cycle the temporal delay between the moment the HV

pulse reaches 10% of its maximum and the moment that the PMT reaches 10% of its maximum, which would indicate streamer inception. We call this temporal delay the inception time t_{inc} and have indicated it in figure 2.3. The estimated total error in t_{inc} is less than 5 ns. Next, a histogram of the t_{inc} values was made. For histograms with logarithmic bins we used a binning function which divided the data into 700 bins in a logarithmic scale starting from 10 ns to the logarithm of the maximum of the t_{inc} (with the MATLAB function of `logspace(log10(0.01), log10(max(data)), 700)`), and for the linear bin histogram (figure 2.13) we divided the data into 100 bins. Note that for low-time bins (ns time range) the histogram is sparsely filled due to the limitation of the oscilloscope memory in long-acquisition windows. This results in a coarser effective bin spacing for these conditions.

2.2.3 ICCD imaging of streamers

An intensified CCD (ICCD, Andor Technology iStar) with nanosecond gate and a Nikkor UV 105 mm lens f/4.5 was used to image the discharges. The images presented in figure 2.2c-e are rendered in a false-colour scale for clarity.

The criterion used for detecting streamer inception is the moment when the PMT shows a peak which is three times higher than the average background noise of the PMT signal which may be originated from ambient light or electronic noise. Note that the very first few pulses after starting the experiment were not included in the measurements to avoid any start-up effects. We found that in all cases exactly one discharge inception event per HV cycle was observed. This means that the discharge inception probability was 100% for all experiments done. The criterion for streamer inception detection was tested using the ICCD camera. In all cases, we found that whenever the PMT detected streamer inception, the ICCD images also showed a developed streamer. The images also show that most of the streamers reach the grounded electrode (see below).

Every time an experimental parameter was varied (pressure, applied voltage, pulse duration, etc.) the system was evacuated to a background pressure of about 1 mbar and then refilled with synthetic air. This procedure removed any species produced by preceding experiments.

2.3 Estimate of initial conditions

Figure 2.2c-d shows ICCD images of streamers with and without applying an LV pulse. The inception cloud, which has been introduced in [57], is smaller when an LV pulse with $t_{\text{LV-sep}} = 0$ and $t_{\text{LV-dur}} = 50$ ms is applied before the HV pulse. Note that

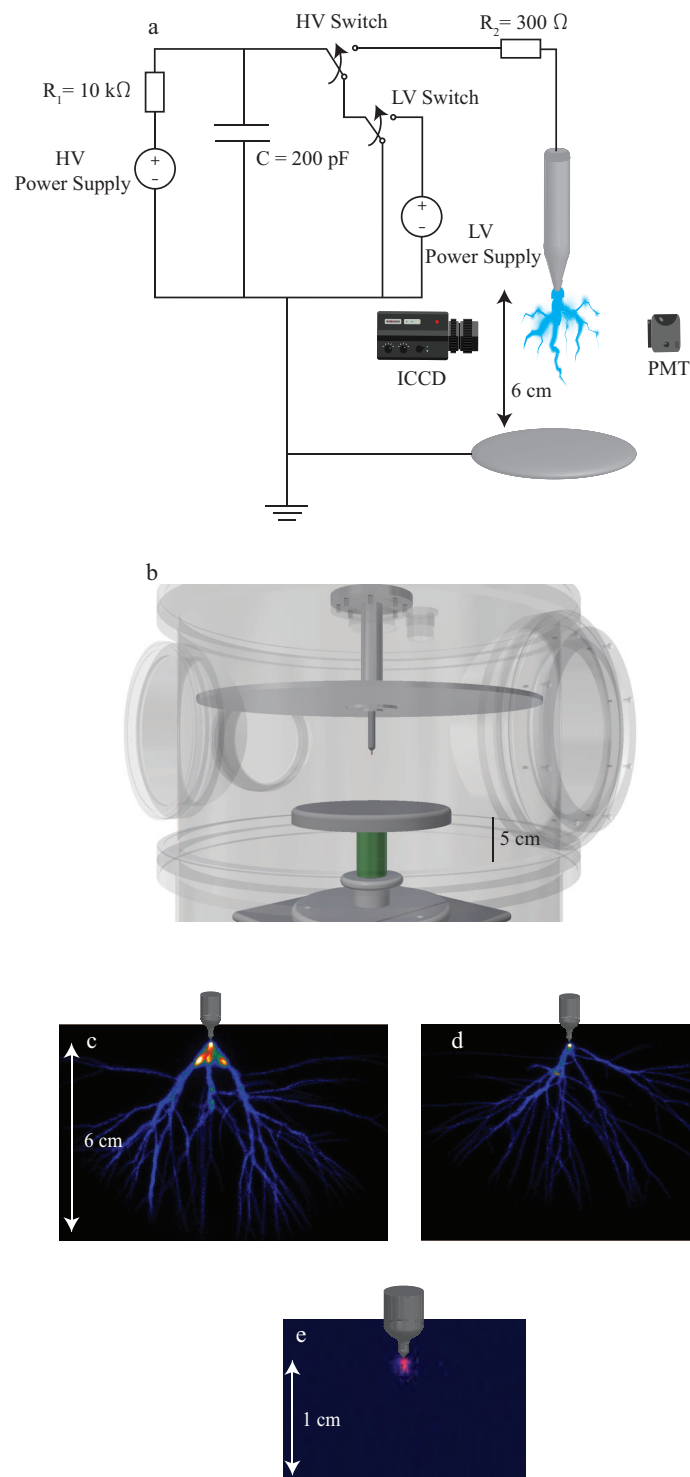


Figure 2.2: a) Schematic view of experimental setup with HV power supply connected to the anode (not to scale), b) schematic of experimental vessel. The large disc above the anode tip is a teflon disc to separate the high-voltage from the top of the vessel. c-e) Discharges in 500 mbar synthetic air with HV amplitude of 17 kV and repetition rate of 2 Hz. c) without applying LV pulse, d) with applying positive LV pulse $t_{LV-sep} = 0$ and $t_{LV-dur} = 50 \text{ ms}$. The gate time of the camera is $10 \mu\text{s}$. e) Glow observed after a streamer burst, the glow lasts for the remaining duration of the HV pulse.

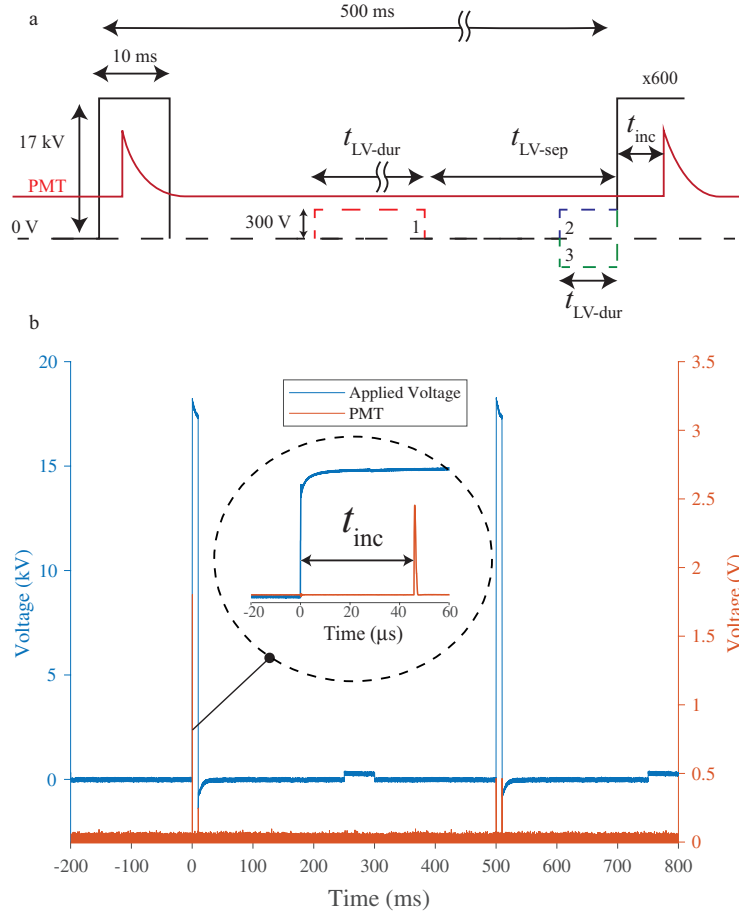


Figure 2.3: a) Scheme of applied HV pulse with three different LV pulse configurations: 1. Positive LV pulse between two HV pulses (red) 2. Positive LV pulse attached to the HV pulse (blue) and 3. Negative LV pulse attached to the HV pulse (green). b) Typical applied HV and LV voltage with PMT signal output.

later we will discuss that after the application of such a positive 50 ms LV pulse (see figure 2.11e) most discharges occur during the rise-time of the HV pulse, i.e., within the first inception peak (to be defined later). Based on these observations, we may conclude that the negative ions which accumulate around the anode during the LV pulse initiate the discharge faster and hence the inception cloud breaks up already during the rise-time of the HV pulse, and hence stays smaller, as the maximal radius is given by voltage over break-down field [57]. A more comprehensive explanation will be given in the coming section. Except for this observation, no significant differences in streamer propagation and branching were found in the streamer images with or without application of a LV pulse. There were also no differences observed between the images of streamers initiated in the first, second, and third peak.

After the streamer burst we observed a DC glow (figure 2.2e), often called Hermstein glow [67], which lasts during the remaining duration of the HV pulse and

uniformly covered the powered electrode tip [68]. The DC glow contains negative charges, screens the local electric field near the electrode tip, and prevents the onset of a new streamer. Generally, the DC glow together with the streamer channel leave ions and excited species behind which can play a significant role in the emergence of streamers during the next HV pulse.

Here we estimate the density and distribution of the ions left behind by a streamer channel at the beginning of the next HV pulse. Electrons are not taken into account in this estimation (and future simulations) since they will attach very quickly after they have been produced (see also figure 2.8). At ground level the majority of background ionization is produced by radioactive decay [69], mainly by radon which produces alpha particles which in turn create electron-ion pairs by disintegration. This process can produce a background ionization level of 10^3 – 10^4 cm^{-3} (predominantly in the form of positive and negative ions). Since we perform our experiments in a metallic vessel which stops alpha particles after tens of μm , the background ionization due to radon decay inside the experimental vessel will be substantially lower. Cosmic ray ionization events can still occur inside the metallic vessel, but for the free electrons to have an effect on the discharge inception, before they become attached, they would need to be present in the small ionization zone around the HV pin electrode (yellow zone in figure 2.3) at the moment the HV pulse is turned on (or before the attachment time on the order of ns).

Following the arguments in [70], the ion density changes due to diffusion and recombination

$$\partial_t n_i = D_{ion} \cdot \nabla^2 n_i - k_{rec} \cdot n_i^2 \quad (2.1)$$

where n_i denotes the density of both positive and negative ions, and net charges and electric fields are neglected. $D_{ion} = 0.1 \frac{\text{cm}^2}{\text{s}}$ and $k_{req} = 2.6 \cdot 10^{-6} \frac{\text{cm}^3}{\text{s}}$ are diffusion coefficient and recombination rate at 500 mbar in air, respectively [70]. Note that we assumed that the positive and negative ion densities are equal. It is possible that there may be a small or local imbalance in charged species densities which would be able to severely affect the recombination rate. The initial condition for this equation consists of a Gaussian streamer channel centered around $r = 0$ with $n_i = n_{channel} \cdot e^{-r^2/R^2}$ with $n_{channel} = 10^{14} \text{ cm}^{-3}$ and $R = 0.3 \text{ mm}$, and an initial background ionization of 0.1 cm^{-3} . These values are derived from an actual streamer observed by an ICCD camera and described in [70]. Fig. 2.4 shows this estimated initial ion density after the end of the HV pulse as $t = 0$ and its temporal evolution under diffusion and recombination until the next HV pulse at $t = 0.5 \text{ s}$. Within these 0.5 s between the pulses, the ionization density decreases to about 10^5 cm^{-3}

on the streamer axis and the spatial profile becomes wider due to diffusion. The ionization density stays approximately constant up to a radius of 0.5 cm. (We remark that we used $\partial_r n_i = 0$ as a boundary condition at $r = 1.5$ cm, which imitates the next streamer channel being at 3 cm distance.)

The calculated initial ion density of 10^5 cm^{-3} is several orders of magnitude larger than the largest initial O_2^- -ion density of 10 cm^{-3} used in the simulations presented in this chapter. The results for these simulations are shown in figure 2.14c and will be discussed in a later section. The main point to be discussed here is that if a density of 10 cm^{-3} (or larger) is used as an initial homogeneous O_2^- -ion density, all inception times t_{inc} are smaller than $1 \mu\text{s}$ which does not match with experiments.

A possible explanation for this discrepancy is the formation of O_3^- and NO_3^- . Popov [71] has shown that already after 10 ms of diffusive expansion of a streamer channel in air at atmospheric pressure the main negative ions are O_3^- and NO_3^- with other ions like O_2^- having a substantially lower contribution to the total negative ion density. O_3^- and NO_3^- have an electron bonding energy 4 and 7 times higher than O_2^- respectively. This means that detachment from these negative ions does not occur as easily as from O_2^- .

O_3^- and NO_3^- will serve as an effective electron sink. The result is that when the next HV pulse is applied, only a small fraction of negative ions (mainly the O_2^- ions) will be able to detach an electron which can initiate the discharge. Further chemical modelling is needed to investigate this in the future.

2.4 Simulation Model

2.4.1 Particle model

We have developed a particle model to simulate the inception behavior. In this model, electrons and negative oxygen ions (O_2^-) are tracked as particles moving through a constant background of N_2 and O_2 molecules under the influence of the local electric field. Table 2.1 shows the plasma-chemical reactions included in the model; they include electron impact ionization, electron attachment and detachment and photo-ionization.

The electrons were moved with a 3D particle model using a Monte-Carlo based collision sampling (MCC) technique, as described in [66], to take collisions with the neutral background gas into account. A Velocity Verlet scheme was used to advance the electrons. The axisymmetric electric field was kept static throughout the simulations. This field was interpolated to the particle positions by converting the Cartesian particle coordinates (x, y, z) to (r, z) coordinates.

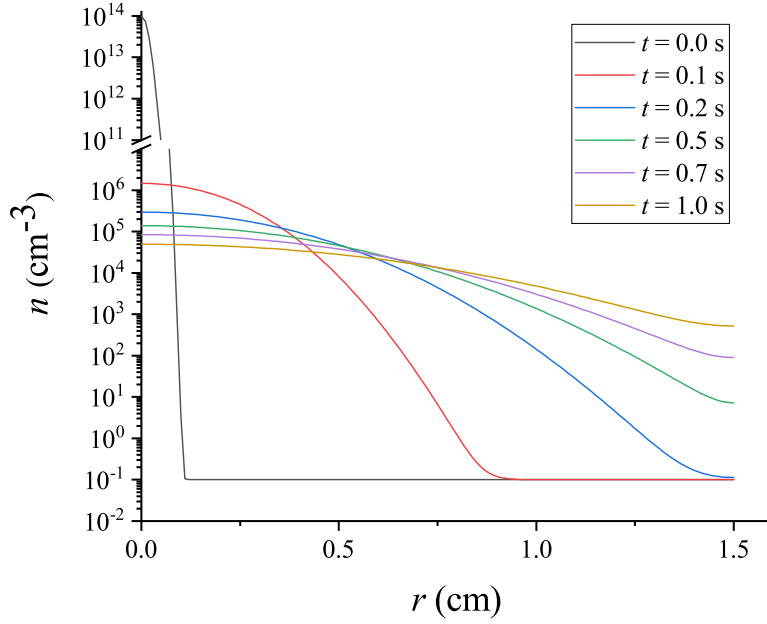


Figure 2.4: Ionization density n_i as a function of radius r for different times t after the streamer discharge, as described in the text.

The availability of cross sections for O_2^- collisions with neutral gas molecules is limited. The motion of these ions was therefore modeled by using a mobility coefficient μ . Their drift velocity is then given by $\mathbf{v} = -\mu\mathbf{E}$, where \mathbf{E} is the electric field at the location of the O_2^- ion. This drift approximation was deemed acceptable since the O_2^- ions only serve as an electron source through detachment.

The mobility of O_2^- as a function of the reduced electric field was taken from the VIEHLAND database [79]. This mobility is reported for air at STP conditions and was scaled to a pressure of 500 mbar using $\mu = \mu_{STP} \frac{N_{STP}}{N}$, with μ and μ_{STP} the mobility at 500 mbar and at 1 bar respectively, and N and N_{STP} the number density of the gas at 500 mbar and at 1 bar respectively. This tabulated database was linearly interpolated to obtain mobilities corresponding to electric fields which are not explicitly included in the database.

Experimentally measured detachment rates were fitted by Pancheshnyi [61] to obtain the following approximation for the electron detachment rate from O_2^- : $r = N_{gas} k_0 \exp \frac{-\Delta\epsilon}{\theta}$. Here, N_{gas} is the number density of the gas, and $k_0 = (1.22 \pm 0.07) 10^{-11} \text{ cm}^3\text{s}^{-1}$ and $\Delta\epsilon = 0.78 \pm 0.03 \text{ eV}$ are the fit parameters used for the Arrhenius approximation. Furthermore, θ is the effective ion temperature calculated as $\theta = \frac{\pi}{2} m_{ion} v_{ion}^2 + k_B T_{gas}$ where m_{ion} and v_{ion} are the mass and velocity of the ion respectively, k_B is Boltzmann's constant and T_{gas} is the temperature of

Elastic	$e^- + N_2 \rightarrow e^- + N_2$ (*) $e^- + O_2 \rightarrow e^- + O_2$ (*)
Ionization	$e^- + N_2 \rightarrow 2e^- + N_2^+$ $e^- + N_2 \rightarrow 2e^- + N^+ + N$ $e^- + N_2 \rightarrow 3e^- + N^{2+} + N$ $e^- + O_2 \rightarrow 2e^- + O_2^+$ $e^- + O_2 \rightarrow 2e^- + O^+ + O$ $e^- + O_2 \rightarrow 3e^- + O^{2+} + O$
Attachment	$e^- + O_2 + O_2 \rightarrow O_2^- + O_2$ (\diamond) $e^- + O_2 \rightarrow O^- + O$
Excitation	$e^- + O_2 \rightarrow$ (*) $e^- + N_2 \rightarrow$ (*)
Photo-Ionization (\ddagger)	1) $e^- + N_2 \rightarrow e^- + N_2^*$ 2) $N_2^* \rightarrow N_2 + \gamma$ 3) $\gamma + O_2 \rightarrow e^- + O_2^+$
Detachment (Δ)	$O_2^- + M \rightarrow O_2 + e^- + M$

Table 2.1: Reactions included in the particle model with $M = N_2$ or O_2 . Cross sections were taken from the Itikawa database [72]–[74]. (\diamond) 3-body attachment was taken from the Phelps database [75] and was only taken into account for the case where O_2 is the third body. According to reaction rates for 3-body attachment reported in [76] the 3-body attachment with O_2 as third body is almost 50 times higher than with N_2 as the third body. (*) Elastic momentum transfer cross sections were taken from the Itikawa database to use as elastic scattering cross sections. Since the particle model only has isotropic elastic scattering this is a valid approximation to make. (*) All excitation reactions for N_2 and O_2 which were listed in the Itikawa database [72] were taken into account; listing them here would clutter the reaction list. (\ddagger) Photo-ionization was included using a stochastic version of Zheleznyak’s model [77], as was done before in [78] and [66]. (Δ) The detachment reaction rate was taken from [61].

the gas. The detachment rate is used as a collision frequency for the O_2^- -ions so that the null collision method can be used to stochastically determine if a detachment reaction takes places in a given timestep for a given O_2^- -ion.

2.4.2 Electric field

The electrode geometry, shown in figure 2.5a, was drawn in a CAD program according to the dimensions of the experimentally used electrode. To calculate the electric field distribution, this CAD drawn electrode geometry was imported into COMSOL [80] where the cylindrical symmetry of the problem was used. The boundary conditions for the scalar potential ϕ were set to: $\frac{\partial\phi}{\partial r}|_{r=0} = 0$, $\frac{\partial\phi}{\partial r}|_{r=7.5\text{ cm}} = 0$, $\frac{\partial\phi}{\partial z}|_{z=13\text{ cm}} = 0$, $\phi|_{z=0} = 0$, and $\phi|_{\text{pin}} = V$ (where V is the applied voltage to the pin electrode). The rise time of the experimentally used voltage source was not taken into account in the simulations. Since we only have negative ions as initial condition in section 3

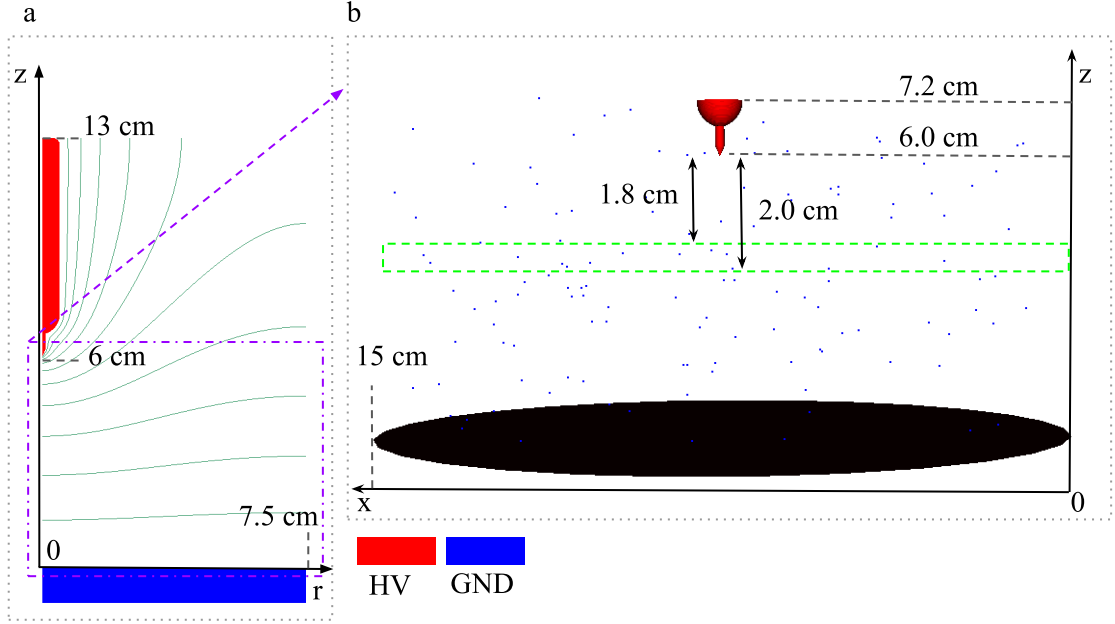


Figure 2.5: The computational domain for a) the electric field computation with COMSOL (included are scalar potential contour lines), and b) the particle model. The COMSOL domain uses cylindrical coordinates while the particle model uses 3D cartesian coordinates in a box of $15 \times 15 \times 7.2 \text{ cm}^3$. The coloured spheres in b) represent O_2^- ions placed homogeneously in the simulation box (in this particular figure a density of 0.1 cm^{-3} was used which equals 128 ions). The green highlighted area represents the position where an inhomogeneous distribution of O_2^- -ions was placed in some simulations to obtain the histograms in figure 2.14d.

the rise time of tens of ns would not have a substantial effect. In choosing these boundary conditions we neglected the influence of the teflon disc above the needle electrode at $z = 13 \text{ cm}$. Because the teflon disc is so far away from the discharge region and the dielectric constant of teflon is only around 2, we can assume that it would not influence the discharge considerably. The reduced electric field on the axis of the discharge gap is shown in figure 2.6, for the case of an applied voltage of 300 V (the LV pulse) and of 17 kV (the HV pulse).

This electric field was imported into the particle model and assumed to remain constant in time during the inception phase, i.e., space-charge effects as they occur later in the streamer phase are neglected. The simulation domain is shown in figure 2.5b; it is a cube of $15 \times 15 \times 7.2 \text{ cm}^3$ which completely covers the 15 cm diameter grounded electrode and the full discharge gap.

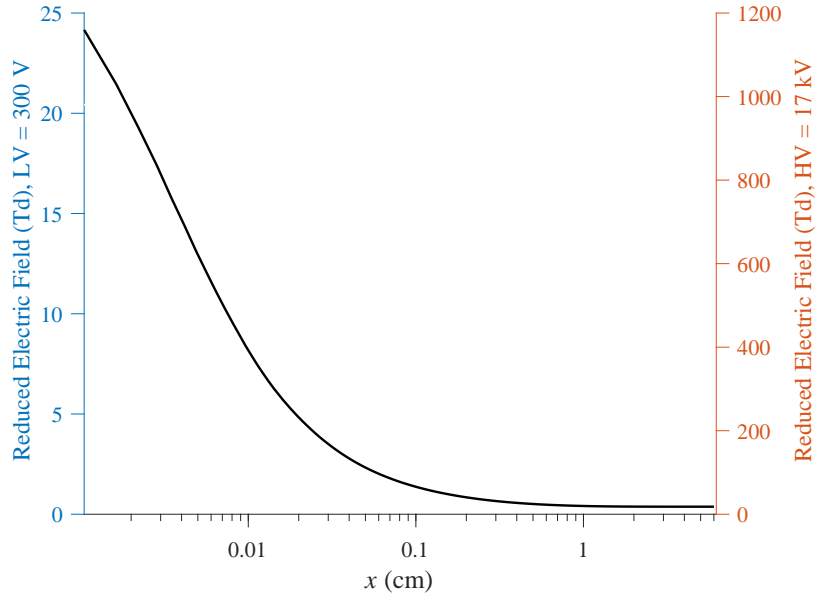


Figure 2.6: The reduced electric field E/N (where N is the gas number density) in Townsend on the axis of the gap for 500 mbar synthetic air at 300 K. Blue (left) y-axis shows the values for an applied potential of 300 V, red (right) y-axis shows the values for an applied potential of 17 kV. The maximum reduced electric field at the tip of the pin electrode ($x = 0$) was 24 Td for 300 V applied and close to 1200 Td for 17 kV applied. The bottom grounded electrode is at $x = 6$ cm.

2.4.3 Inception time t_{inc}

In the experiments, the inception time t_{inc} was measured as the time from the application of the high voltage pulse until the time of light emission from the discharge. In the simulations, the presence of 10^6 electrons was used to determine the moment of inception, as was also done in previous inception simulations [81]. We assume the presence of 10^6 electrons indicates rapid and continued discharge growth, due to additional electron avalanches caused by photo-ionization.

2.4.4 Drift and reaction times

To guide the interpretation of the experimental results, we here discuss relevant drift and reaction times.

Figure 2.7 shows the drift time $t_{\text{drift}}(x)$ of electrons and O_2^- ions from a distance x to the pointed electrode at $x = 0$ on the axis of symmetry. It is calculated as

$$t_{\text{drift}}(x) = \int_0^x \frac{1}{\mu(E)E(x')} dx', \quad (2.2)$$

where μ is the mobility of the respective species, and $E(x)$ the electric field on the axis, see figure 2.6. The two axes on the left of Figure 2.7 show the drift time of

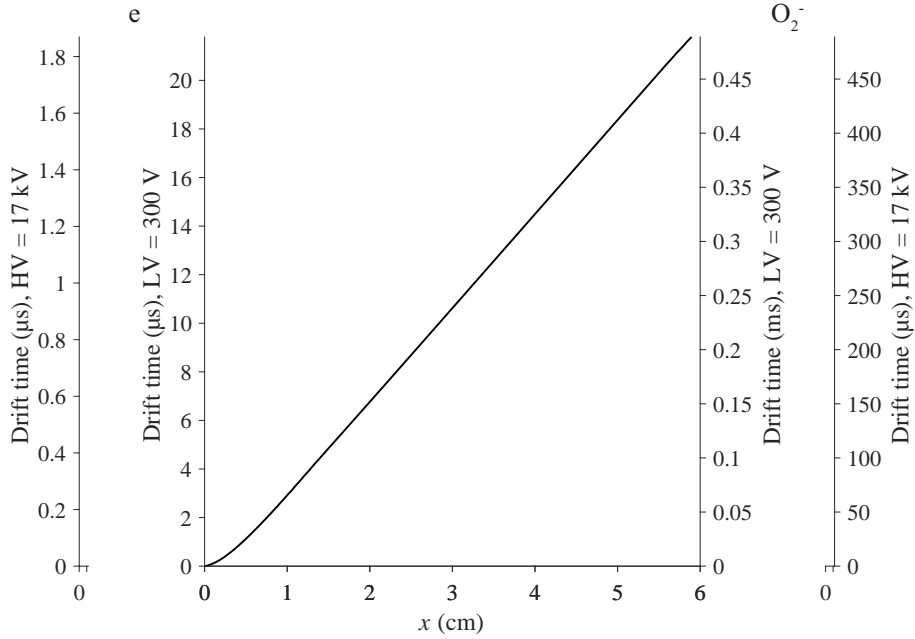


Figure 2.7: Drift time on the axis of symmetry of an electron (left) or an O_2^- ion (right) from a distance x to the pointed electrode at $x = 0$ when a voltage of 300 V (inner y-axis) or 17 kV (outer y-axis) is applied across the gap. Calculated using (2.2). Only a single line is drawn because the different mobilities and voltages only change the slope of the drift time curves which can be reflected in the y-axis scale.

electrons either in the high voltage (HV) of 17 kV or in the low voltage (LV) of 300 V, and the two axes on the right show the same for O_2^- ions, in the inverse order of LV and HV. To cross the gap of 6 cm on the axis of symmetry, electrons need around $1.8 \mu\text{s}$ under HV conditions and $20 \mu\text{s}$ under LV conditions, and O_2^- ions need around $490 \mu\text{s}$ (HV) and 27.5 ms (LV).

The charged species do not only drift in the field, but they also react, and characteristic times for electrons as a function of reduced electric field are plotted in Figure 2.8, namely the attachment time, the detachment time and the impact ionization time as a function of the reduced electric field. The breakdown field is indicated as well; for higher fields electron avalanches grow.

2.5 Results and Discussion

2.5.1 Baseline Experiment

In our baseline experiment, we applied HV pulses of 17 kV with a duration of 10 ms to artificial air at 500 mbar, and we repeated this 6000 times with a repetition frequency of 2 Hz. The histogram of inception times t_{inc} is displayed in figure 2.9a

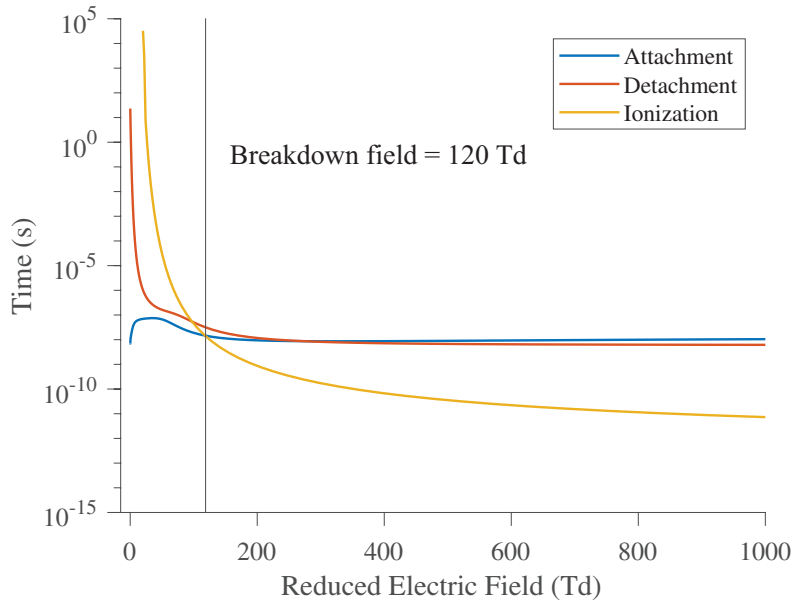


Figure 2.8: Attachment, detachment and ionization time of electrons in an 80/20 N_2/O_2 mixture at 500 mbar. The detachment time from O_2^- was calculated from formulas given in [61]. The attachment and ionization time was calculated from cross sections of Itikawa [72]–[74] and for the 3-body attachment from Phelps [75] which were input into BOLSIG-[82], [83] to calculate reaction rates.

on a logarithmic scale for the time, where the size of the time bins is scaled as $\log t$. The histogram shows that there are three distinct peaks in this distribution, namely at around 20 ns, 25 μs , and 125 μs . The aim of the chapter is to study the conditions for these three peaks to form and to understand their physical nature as far as possible — though puzzles remain.

It is clear that a discharge starts from an impact ionization avalanche of electrons in the high field zone near the pin electrode. And our simulations confirm that one initial electron in this region can start sufficient electron multiplication to start a discharge, at least when it is initially near the symmetry axis of the set-up. So the relevant question is: where do these initial electrons come from, when and how many? And the fact that there are three distinct inception time peaks suggests, that there might be three distinct sources for these electrons.

In a first step, we have checked whether there is any temporal correlation between discharges of the three different peaks. Figure 2.9b shows the t_{inc} histogram for the discharges immediately before a discharge with a t_{inc} in the first peak, and panels c and d show the same for the second and third peak. We see that the histograms in figure 2.9b-d all retain the same structure as the baseline figure 2.9a, up to differences due to the different total number of discharges. This means that the inception times t_{inc} for two consecutive discharges are uncorrelated.

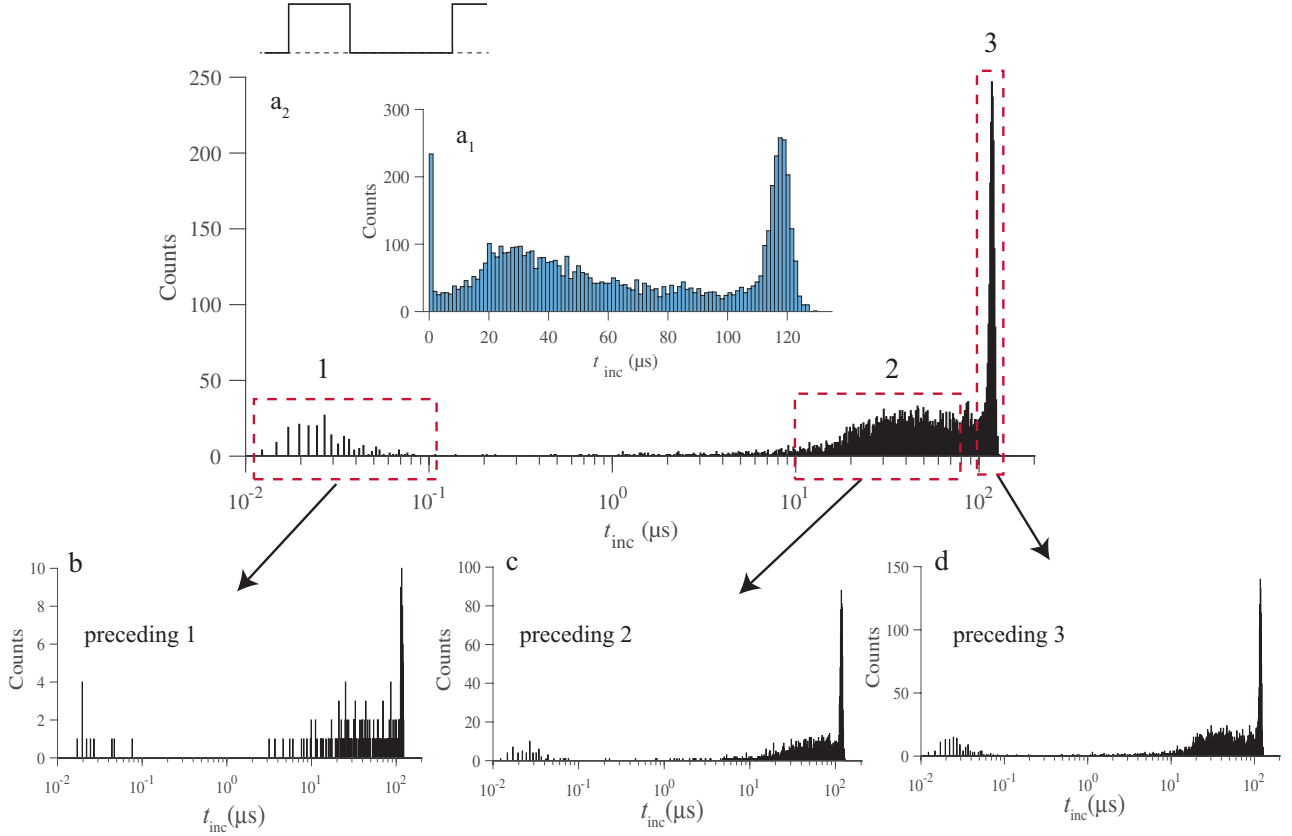


Figure 2.9: Histogram of discharge inception times t_{inc} with a_1) linear and a_2) logarithmic bins for 6000 discharges in the baseline experiment. For the logarithmic plot the bin size scales with $\log t$, but note that for the smallest timescales most bins are empty due to sparse oscilloscope sampling (low sampling rate). The graph in the upper left corner of panel a) indicates the voltage wave form, a sequence of high voltage pulses. The graphs in the second row show the histogram of t_{inc} for the pulse preceding b) the first peak, c) the second peak, and d) the third peak. The contribution of the first, second, and third peak is 3.4%, 60.9%, and 31.8%, respectively. Note that the second peak is not covering all of the data between the first and the third peak.

2.5.2 Baseline theory

Before embarking into a more detailed discussion of the experiments, let us first state what we expect in the simplest case: a homogeneous distribution either of electrons or of O_2^- ions.

Let us assume in a first step that electron reactions like impact ionization or attachment as well as electron diffusion can be neglected. In this case the electron flux \mathbf{j} in an electric field \mathbf{E} is $\mathbf{j} = \mu_e(E)\mathbf{E} n_e$ where n_e is the electron density. We can neglect space charge effects on the inception process itself because space charge densities of such magnitudes that they have a significant effect on the electric

field contradict with the observed stochastic behaviour of the inception delay. If the mobility μ_e does not depend on the electric field, and if there are no space charges $\nabla \cdot \mathbf{E} = 0$, then a homogeneous electron density will stay homogeneous while drifting in the field, as

$$\partial_t n_e = -\nabla \cdot \mathbf{j} = -\nabla \cdot (\mu_e \mathbf{E} n_e) = 0, \quad (2.3)$$

according to the conservation law of electrons and to the assumptions above. This means that at any moment in time the same flux of electrons passes at any point in space, independently of the precise electric field configuration. In particular, the electron flux arriving at the high field zone near the electrode is constant in time.

As shown in A.1, the probability density of inception can then be approximated by

$$f(t) = N/t_{\max} (1 - t/t_{\max})^{N-1}, \quad (2.4)$$

where N denotes the initial number of electrons (or O_2^- ions) equally distributed in some volume around the electrode and t_{\max} is the maximal drift time of these particles towards the electrode. As discussed in A.1, equation (2.4) depends to a good approximation on the ratio N/t_{\max} , which can be interpreted as the number of particles reaching the electrode per unit time. Figure 2.10 illustrates the dependence of equation (2.4) on N and t_{\max} . In all cases, the probability of inception decreases with time, but this happens more rapidly for larger values of N/t_{\max} . The mean inception time given by equation (2.4) is $t_{\max}/(N + 1)$; this time scale decreases approximately like the inverse of N/t_{\max} .

The above analysis applies to both electrons and O_2^- ions, but with a longer time scale for O_2^- ions due to their smaller mobility. These ions will drift in the field until they reach the high field zone, where they detach an electron that can start an avalanche and a discharge. In the experiments, we expect to have mostly negative ions at the beginning of the HV pulse, since the time scale for electron attachment in the absence of an electric field is on the order of 10 ns, see figure 2.8.

Comparing the analytical estimate for the histogram of inception times t_{inc} in figure 2.10 with the experimentally observed histogram in figure 2.9 we see that there is a strong deviation from the analytical estimate, with three peaks in the distribution rather than one continuous decrease. Therefore at least one of the assumptions above must be wrong. This could for example happen when:

- There is more than one species involved.
- The species are initially not homogeneously distributed.

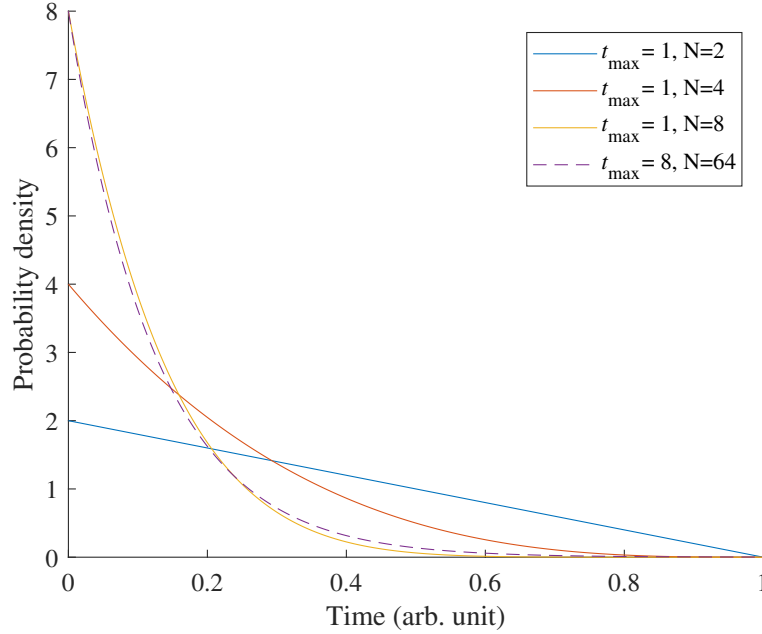


Figure 2.10: Analytic estimate of the inception probability versus time as given by equation (2.4). N represents the initial number of particles and t_{\max} their maximal drift time to the electrode, see the text for details. Note that the inception probability depends, to a good approximation, on the ratio N/t_{\max} . Surprisingly, our experimental results do not resemble the curves shown here.

- Attachment or ionization reactions cannot be neglected along the path of the charged species or there is another reaction liberating or binding free electrons under specific conditions.
- There are space charge effects, hence $\nabla \cdot \mathbf{E} \neq 0$.
- The mobility of the species is strongly field dependent.

In the following sections we will discuss each peak in the distribution of inception times, and how and why they deviate from the analytical estimate above.

2.5.3 The first peak

In the inception time histogram, shown in figure 2.9a with a statistics over 6000 discharges, the first peak occurs between 10 ns and 100 ns which is several orders of magnitude earlier and shorter than the two other peaks. The first peak accounts for about 3.4% of all inception events.

There are essentially two possible sources for this early peak: either free electrons are already available when the HV pulse starts, or there are particles, e.g., O_2^- ions, that rapidly release electrons at that moment.

Electrons are quite unlikely to be present at the beginning of the HV pulse, since according to figure 2.8 they attach to oxygen on a timescale of 10 to 100 ns for electric fields well below the breakdown value. Therefore electrons produced during a previous HV pulse will attach between the pulses. It is reasonable to assume that free electrons already present in the gap when an HV pulse is applied were not produced by a previous discharge, but by rare events like cosmic rays or radioactive decay of materials present in the lab.

O_2^- -ions could be a source of free electrons as figure 2.8 shows that a detachment time smaller than 100 ns occurs for a reduced electric field larger than 120 Td. Figure 2.6 shows that this reduced electric field is found for distances smaller than 0.06 cm from the pin electrode when a potential of 17 kV is applied. This shows that ions very close to the pin electrode can detach an electron sufficiently rapidly to produce the first peak. The region of space extending to a distance of 0.06 cm will be called the active zone for the rest of the discussion of the first peak. The following discussion will assume O_2^- -ions to be the main contributor to the discharges belonging to the first peak (in principle any detaching negative ion can contribute to the discharge inception, but for our experimental conditions O_2^- will be the most prevalent [61]).

Hypothesis: electrons detaching from O_2^- in the active zone as the source of the first peak

To test whether O_2^- -ions were present before an HV pulse, we applied a positive LV pulse of 300 V with a duration of $t_{LV-dur} = 1$ ms or longer and immediately before the HV pulse ($t_{LV-sep} = 0$). The goal was to pull all negative ions in the gap towards the pin electrode during the LV pulse without triggering a discharge.

The histogram of inception times for 600 repetitions of the pulse experiment is shown in figure 2.11b; it shows that the first peak is removed. The removal of the first peak can be explained in the following manner: As O_2^- -ions are drawn closer to the electrode at a certain point they will be too close to the surface of the electrode for a detached electron to produce a large enough avalanche to initiate a discharge.

A new question arises when we follow this reasoning: Why wouldn't O_2^- coming from further in the discharge gap 'replace' the O_2^- that are now pulled too close to the pin electrode and thus keep the first peak unchanged? This can only happen if the density of O_2^- -ions is higher in the active zone than in the region of space from which O_2^- -ions could travel towards this active zone during the LV pulse. It remains unsolved as to what would cause such a difference in O_2^- density. A possible source of a higher density of O_2^- ions close to the pin electrode could be the continuous

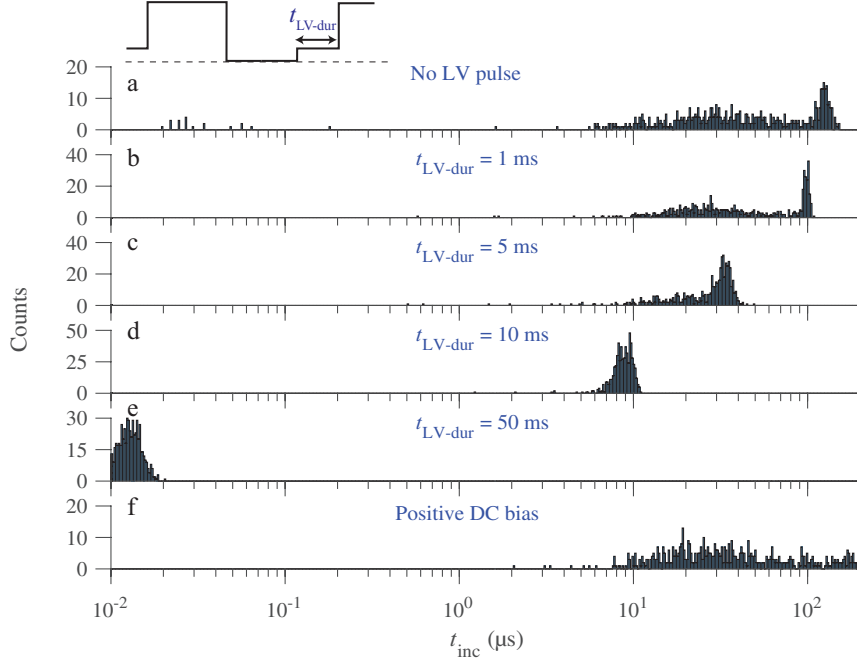


Figure 2.11: Histograms of discharge inception time t_{inc} for 600 discharges produced a) for no LV pulse and by applying a 300 V pulse for $t_{\text{LV-dur}} =$ b) 1, c) 5, d) 10, and e) 50 ms, f) a DC bias before a 17 kV pulse of 10 ms with a repetition frequency of 2 Hz.

glow discharge observed after a discharge has been triggered but before the HV pulse is turned off. This glow discharge has been discussed in section 3.

Figure 2.12 shows the effects that a -300 V LV pulse has on the t_{inc} histogram. For any duration $t_{\text{LV-dur}}$ (1 ms, 5 ms, 10 ms, 50 ms, and DC) of the LV pulse, O_2^- should drift out of the active zone according to the calculated drift times in figure 2.7. This would mean that the first peak should not be present anymore in the t_{inc} histogram or be shifted to higher t_{inc} accounting for the drift time of O_2^- -ions. Figure 2.12b-f shows that the first peak remains present for times below 100 ns, just as without an LV pulse.

A possible explanation is that the electric field off-axis of the discharge gap is much lower which would keep at least some O_2^- -ions in the active zone during a negative LV pulse. This is a reasonable explanation for the short LV pulses ($t_{\text{LV-sep}} \leq 10$ ms), but should still not be able to explain the results for $t_{\text{LV-sep}} = 50$ ms or negative DC.

Another explanation can be the emission of electrons from the electrode due to impact/absorption of the positive ions. The kinetic energy of the positive ions will be much lower than the work function of the electrode, but if the positive ions

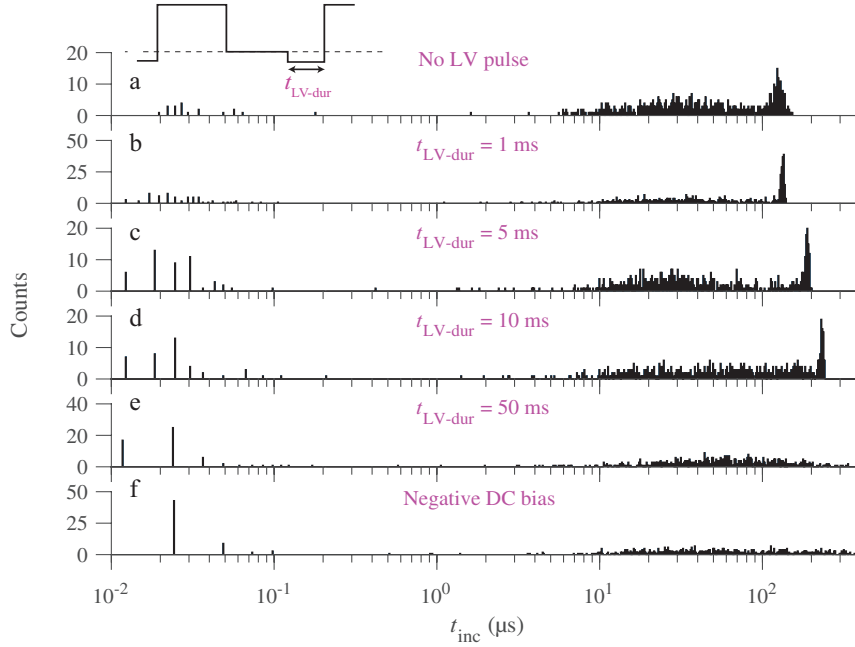


Figure 2.12: Histograms of discharge inception time t_{inc} for 600 discharges produced by applying a -300 V pulse for $t_{\text{LV-dur}} =$ b) 1, c) 5, d) 10, and e) 50 ms, for a) no LV pulse and f) a DC bias before a 17 kV pulse of 10 ms with a repetition frequency of 2 Hz. Note: The y-axis of each histogram is different which can give the impression that the first peak strongly changes in height depending on $t_{\text{LV-dur}}$ which it does not.

are in a more energetic state (increased internal energy) then a surface reaction might occur which emits an electron.

2.5.4 The second peak

Experimental evaluation

The second peak in the inception time histogram in figure 2.9 occurs around $25\ \mu\text{s}$. We re-plot this data in figure 2.13a in a linear scale to better investigate this source of discharge inception. The results of applying a positive or negative LV pulse, with different $t_{\text{LV-dur}}$, before the HV pulse ($t_{\text{LV-sep}} = 0$) are plotted on a linear scale in figure 2.13b-f.

We see in figure 2.13b-f that the second peak does not shift significantly to lower or higher t_{inc} . The first and third peak shift substantially more and, in figure 2.13d, the shifted third peak 'eats up' part of the second peak. These results suggest that the source of the second peak is not measurably influenced by the electric field produced by the LV pulse.

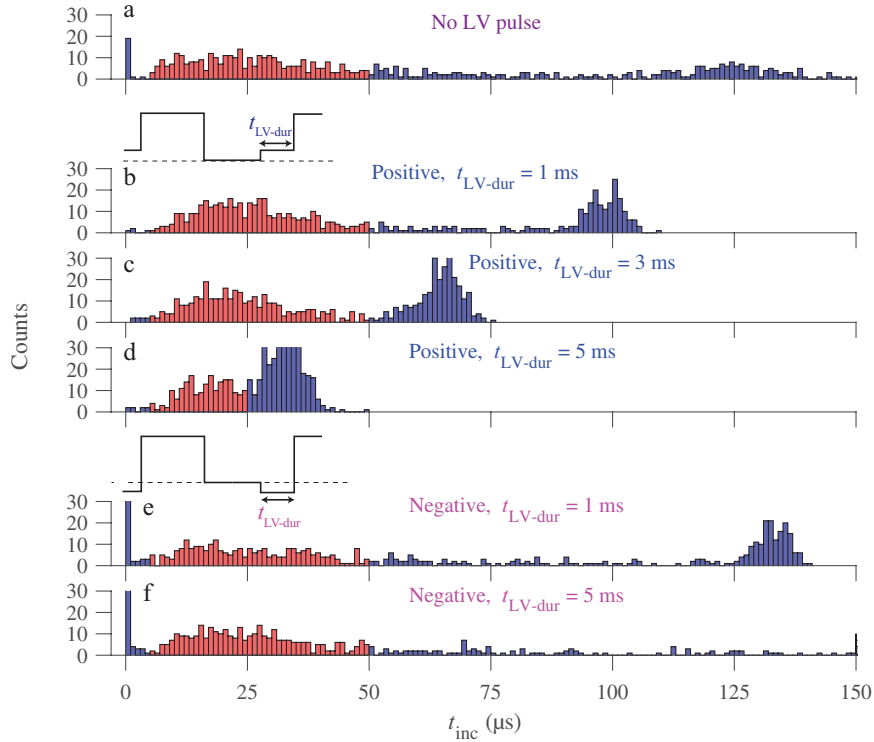


Figure 2.13: Characterization of second peak (red bars) after applying positive (b-d) and negative (e-f) LV pulses with 300 V amplitude and varying t_{LV-dur} . Note: The peaks of this histogram are clipped at 30 counts. This figure is mainly to show relative shifts of the second peak to the other peaks. For absolute counts refer to figure 2.11 and 2.12.

For one set of 600 discharges we decreased the repetition frequency of the HV pulses to 0.2 Hz to investigate its effects on the second peak. Figure 2.17a shows the effect that this repetition frequency change had on t_{inc} . We see that decreasing the repetition frequency causes the first and third peak to completely disappear while keeping the second peak intact. The source of the second peak seems to be able to live for at least 5 seconds without an applied electric field.

We would also like to remark that we had to open up the vessel once for maintenance. When we closed the vessel and pumped the pressure down to 500 mbar, the second peak was completely removed from the t_{inc} histogram. After pumping the vessel down for a week we measured the t_{inc} histogram again and found the histogram as in figure 2.9 again. We think that by opening the vessel we allowed H_2O to enter the vessel. From [45] we know that H_2O is an effective quencher of excited O_2 and N_2 states which could correspond with the removal of the second peak. Since H_2O is not easily pumped out of the vessel we required a week to obtain the original synthetic air composition of 80% N_2 and 20% O_2 .

In the following section we will discuss several hypotheses which could explain the different experimental observations about the source of the second peak (No

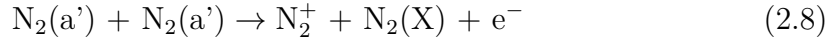
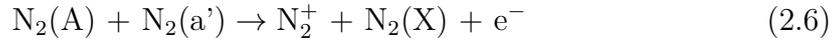
measurable effect of an LV pulse, only peak which remains when the repetition frequency is reduced to 0.2 Hz, and removal of only this peak when the vessel was briefly opened).

Hypothesis

The first peak has been argued in the previous section to be caused by discharge inception by free electrons or O_2^- already present in the discharge gap when the HV pulse is applied (or created shortly thereafter).

Since the first peak is influenced strongly by applying an LV pulse before the HV pulse and the second peak is not, we think it is likely that the second peak is caused by electron creation processes involving only neutral species.

One hypothesis would be the production of electrons due to Penning ionization. We worked in an N_2/O_2 gas mixture so we can identify various Penning ionization reactions from literature [84]:



However, the lifetime of the excited states $N_2(A)$ and $N_2(a')$ are determined by quenching reactions with O_2 as shown in [85]. At a pressure of 500 mbar these quenching reactions will have a timescale on the order of 10 to 100 ns. Taking these quenching reactions into account we can assume that the density of $N_2(A)$ and $N_2(a')$ will be very low after the 100s of ms that the HV pulse was off and thus cannot explain the second peak.

Another possible explanation for the second peak could be that there are quasi-neutral patches of charged species which, due to their space charge effects, cannot be pulled apart by the field created by the LV pulse (or DC), but the large charge densities required for this are not consistent with the observed stochastic inception behaviour.

2.5.5 The third peak

Source of Electrons

The third peak in the baseline experiment occurs around 125 μs . The histogram obtained when we applied a 300 V pulse for 1 ms before the HV pulse, shown in figure 2.11b, shows that the third peak shifted to lower t_{inc} . This shift can mean one of two things: either the source of electrons shifts closer to the electrode, or the process to produce an electron is sped up.

Theoretical results obtained by assuming that the third peak is caused by a source of electrons which can move due to the application of an LV pulse match well with the experimental observations. For this reason the following analysis will start from this assumption.

Hypothesis: Drift time of O_2^- as the characteristic time of the third peak

Assuming that the inception time for the third peak is caused by the drift time of a negative ion (e.g. O_2^-) we can calculate whether the shift of the third peak, when applying a positive LV pulse, corresponds to the movement of negative ions during the positive voltage pulse. In the following calculations the drift of the negative ions is calculated directly on the axis of the pin electrode. The electric field will be slightly different off-axis and so results will change when ions are allowed to drift off-axis.

Without a positive LV pulse the third peak occurs at 122.8 μs . We assume that this is the average drift time of an O_2^- -ion to get to the HV pin electrode. In principle it is sufficient for the negative ions to travel to the ionization zone, but for calculation purposes it is easier to take the HV pin electrode as endpoint. We therefore find the distance Δx from the HV electrode at which the negative ions start by applying equation 2.2, where t_{inc} is the average inception time of 122.8 μs , $E(x)$ is the applied electric field between the electrodes (on the axis), and $\mu_I(E(x))$ is the O_2^- -ion mobility at 500 mbar at position x . We obtain $\Delta x = 1.73$ cm. This means that if the inception time of 122.8 μs of the third peak is caused by the drift time of negative ions to the HV electrode, they would need to have started at a distance of 1.73 cm from the pin electrode.

When we applied a positive LV pulse with $t_{\text{LV-dur}} = 1$ ms and $t_{\text{LV-sep}} = 0$, the third peak shifted to 98.3 μs . Performing the same calculation as before, we find that the negative ions started at a distance of 1.45 cm from the HV pin electrode. Indicating that during the LV pulse the negative ions moved 0.28 cm towards the pin electrode.

Now we can calculate the distance that an O_2^- -ion would travel during this LV pulse. Starting from a position of 1.73 cm from the pin electrode the O_2^- -ion

t_{LV-dur} (ms)	t_{inc} (μ s)	Δt_{inc} (μ s)	x_{start} (cm)	Δx_{start} (cm)	Δx_{LV} (cm)
Positive LV					
0	122.8		1.73		
1	98.3	24.5	1.45	0.28	0.20
5	32.52	90.28	0.66	1.07	1.04
10	9.1	113.7	0.3	1.43	>1.73
Negative LV					
0	122.8		1.73		
1	132.3	-9.5	1.84	-0.11	-0.2
5	184.6	-61.8	2.45	-0.72	-1.03
10	228.3	-105.5	2.95	-1.22	-2.02

Table 2.2: Table with experimentally observed shifts (Δt_{inc}) of the third peak in the t_{inc} histograms shown in figure 2.12 when applying an LV pulse with variable t_{LV-dur} . If the t_{inc} of the third peak corresponds to the drift time of O_2^- -ions then x_{start} would be the average starting position of the O_2^- -ions. The shift in starting position due to the LV pulse is represented by Δx_{start} . The distance that O_2^- can travel during the LV pulse is calculated using Eq.(2.2) and represented here as Δx_{LV} .

will drift for a time t_{LV-dur} in the field of the LV pulse. In this case $t_{LV-dur} = 1$ ms and using Eq.(2.2) we find $\Delta x = 0.20$ cm.

We see that the difference in travel distance (1.73 cm - 1.45 cm = 0.28 cm) of the negative ions for the experiments with and without this positive LV pulse corresponds to the distance O_2^- -ions can travel during this LV pulse (0.20 cm). These calculations suggest that O_2^- -ions cause the third peak and that the values of t_{inc} correspond to the average drift time of the O_2^- -ions to the HV pin electrode.

A comparison of the shift of the third peak caused by the application of a positive LV pulse with various t_{LV-dur} and the distance negative ions can travel during this LV pulse is given in table 2.2. In this table we can observe that for $t_{LV-dur} = 10$ ms the O_2^- -ions should have already reached the pin electrode, but their starting position seems to still be 0.3 cm from the pin electrode. A possible explanation is that the electric field of the LV pulse is not the only force in the gap. Space charge effects could reduce the distance that the negative ions can drift in the field of the LV pulse.

We also applied a negative LV pulse with various t_{LV-dur} and $t_{LV-sep} = 0$. Figure 2.12e shows the histogram obtained from these experiments. We can see that the third peak is now shifted to higher t_{inc} . Table 2.2 shows the experimental and calculated shifts of the third peak for different t_{LV-dur} . We can see that the calculated shifts match pretty well with the experimentally observed shifts. The presented results seem to agree with the idea that the third peak is mainly caused by the drift of negative ions, likely to be O_2^- -ions.

Note that there is a sharp drop after the third peak of around $125\ \mu\text{s}$. An interpretation could be that up to a distance of around $1.7\ \text{cm}$ there are sufficient negative ions to have a near unity probability of inception. The results should not be interpreted as if there are no ions after this distance of $1.7\ \text{cm}$, they simply do not get a chance to be the cause of inception.

Producing the Third Peak

Here, we discuss how the third peak appears in linear and log scaled histograms of t_{inc} obtained from particle simulations with different initial conditions. The goal is to understand what the initial conditions of the particle simulations have to be to obtain a comparable result to experiment. Homogeneous ion densities of $0.1\ \text{cm}^{-3}$ to $10\ \text{cm}^{-3}$ were used as initial conditions. Only O_2^- -ions were placed since from figure 2.8 we can see that most electrons should have attached already during the $490\ \text{ms}$ HV pulse off-time. A fourth particle simulation was done where a homogeneous ion density of $10\ \text{cm}^{-3}$ was placed together with an extra patch of ions at a distance of around $1.9\ \text{cm}$ from the pin electrode as shown as the green rectangle in figure 2.5. This extra patch of ions contained 3 times as many ions as in the rest of the domain (124 in the domain, 354 in the extra patch). Each initial condition was run 600 times to obtain statistics on t_{inc} from the simulation results. An initial homogeneous distribution of $0.1\ \text{cm}^{-3}$ O_2^- resulted in a probability of inception within $1\ \text{ms}$ of 91%, all other initial conditions had a 100% inception chance.

We can see in all initially homogeneous cases that the experimentally observed peak around $125\ \mu\text{s}$ is absent from the linear scaled histograms shown in figure 2.14a-c.

The log scaled histogram shown in figure 2.14a₂ contains a peak $> 125\ \mu\text{s}$ which would naively be matched with the third peak observed in figure 2.9. A property of the log scaled histogram is that the bins on the x-axis increase in size as we move along the x-axis. This property causes a peak to show up in log scaled histograms fairly easily. However, note that in the experimental observations of the third peak, it is also visible on a linear scale.

For these simulations there was only one assumption which was that the initial ion density was distributed homogeneously. Since we are investigating the discharge inception for repetitive pulses it is possible that the initial density for the next pulse is not homogeneously distributed. Figure 2.2c shows a typical discharge during one of the HV pulses. We can see that it is not unreasonable to assume an initial inhomogeneous distribution of ions as we move away from the HV pin electrode.

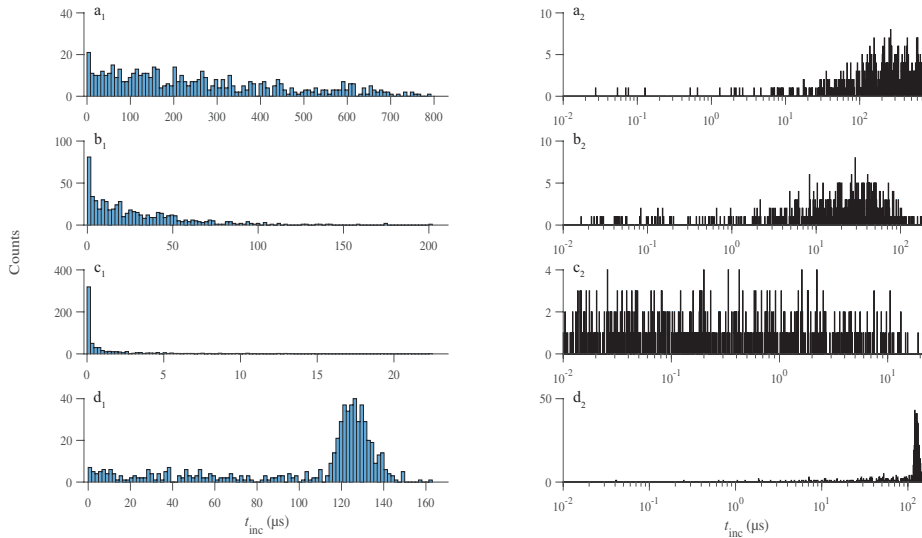


Figure 2.14: Histograms of t_{inc} from particle simulations with a sample size of 600. Histograms on the same row depict the same simulation results but left side is linear and right side is logarithmic. The initial homogeneous density of O_2^- -ions were: a) 0.1 cm^{-3} ($N = 124$), b) 1 cm^{-3} ($N = 1238$), c) 10 cm^{-3} ($N = 12364$), and d) 0.1 cm^{-3} ($N = 124$) with an extra patch of O_2^- -ions ($N = 354$) placed between 1.8 cm and 2.0 cm from the pin electrode (green highlighted area in figure 2.5). All simulations have an inception probability of 1 except for a) which has an inception probability of 0.92.

Figure 2.14d shows the histograms of t_{inc} for the simulations with an extra patch of O_2^- -ions placed between 1.8 cm and 2.0 cm from the pin electrode. Due to this inhomogeneous distribution of O_2^- -ions we can see in these histograms that a peak is not only present in the logarithmic scale but also in the linear histogram.

From these results it seems that some inhomogeneity in the spatial distribution of O_2^- -ions is needed to produce the experimentally observed third peak in the histogram of t_{inc} .

Increasing duration between LV and HV pulse

In this section we investigate the influence of increasing the time between the LV pulse and the next HV pulse. We apply an LV pulse of 300 V for a duration of 50 ms at $t_{\text{LV-sep}}$ ms before the next HV pulse i.e. if $t_{\text{LV-sep}} = 0$ ms then the LV pulse is attached to the next HV pulse which is the same situation as shown in figure 2.11e. An LV pulse duration of 50 ms was chosen because this is a sufficient time to pull all negative ions in the discharge gap towards the HV pin electrode.

Figure 2.15 shows a collection of histograms of t_{inc} for different values of $t_{\text{LV-sep}}$. We see that for small values of $t_{\text{LV-sep}}$ (5 - 10 ms, figure 2.15b-c) a peak is moving from small t_{inc} to higher t_{inc} and for high values of $t_{\text{LV-sep}}$ (150 - 250 ms, figure

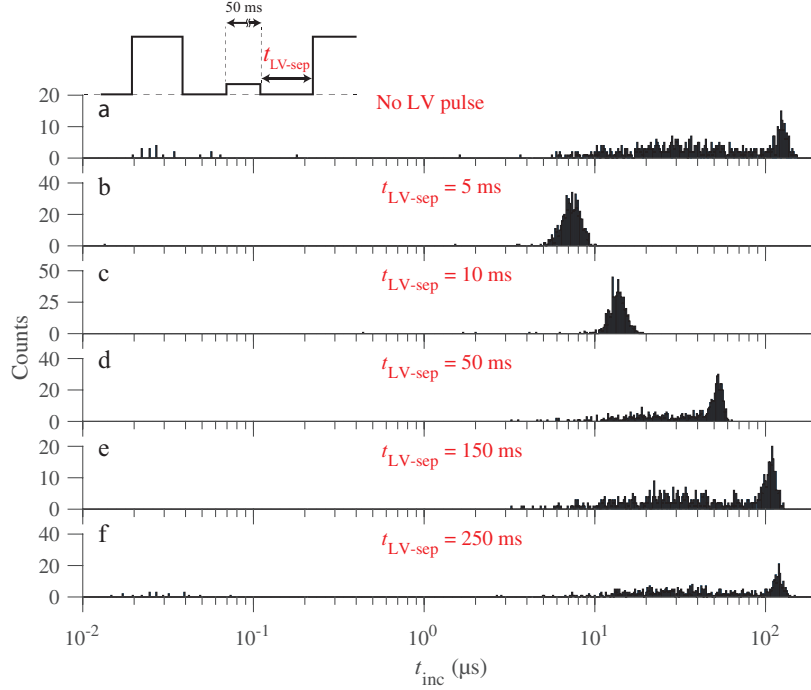


Figure 2.15: Histograms of discharge inception time t_{inc} for 600 discharges produced by applying a 300 V pulse for 50 ms and $t_{\text{LV-sep}} = b)5, c)10, d)50, e)150, f)250$ ms before a 17 kV pulse of 10 ms with a repetition frequency of 2 Hz.

2.15e-f) the histogram resembles the baseline experiment histogram (figure 2.15a). We can make sense of this behavior by noting that the 50 ms LV pulse of 300 V not only pulled all negative ions towards the HV pin electrode, but also pushed positive ions away from it. When the applied potential is now turned off, the separation of these charged species can create an electric field which pulls the charged species back towards their starting position.

If $t_{\text{LV-sep}}$ is not long enough (5 - 10 ms, figure 2.15b-c) we see that the negative ions did not have enough time to return back to their starting position and are still relatively close to the HV pin electrode. Because they are still close to the HV pin electrode they can trigger a discharge quickly (μs) after the application of the HV pulse. If $t_{\text{LV-sep}}$ is long enough (150 - 250 ms, figure 2.15e-f) we can see that the charged species were able to return back to their starting position since the histograms now resemble the baseline experiment (figure 2.15a).

Increasing LV Pulse Duration

In this section we investigate the influence of high values of $t_{\text{LV-dur}} (\geq 50 \text{ ms})$ for the same voltage configuration as for the experiment in figure 2.11. Figure 2.11

and figure 2.16 show that for t_{LV-dur} up to 50 ms the third peak moves to the left (the discharge starts faster). For higher values of t_{LV-dur} , the third peak disappears and the second peak seems to re-emerge.

When $t_{LV-dur} = 50$ ms, the negative ions can gather around the HV pin electrode. When an HV pulse is then applied, right after this LV pulse, the negative ions no longer have to travel towards the HV pin electrode. The only process that needs to happen to trigger a discharge is the detachment of an electron from the negative ion which can then start the discharge.

Increasing t_{LV-dur} keeps the negative ions against the pin electrode for a longer time. During this time the negative ions can neutralize [86]. Inception becomes slower as t_{LV-dur} increases since more negative ions are neutralized. The result of applying any positive LV pulse is that negative charges are being removed from the discharge gap. For the LV pulse applied in this work: the free electrons need $t_{LV-dur} \geq 1$ ms, and the negative ions need $t_{LV-dur} \geq 50$ ms.

If the LV pulse is on during the entire time between two HV pulses (positive DC bias), we see in figure 2.16f that the third peak is almost completely removed. The counts that are still present around the third peak timescale (125 μ s) could still be caused by leftover negative ions, but they can also be due to the long tail of the second peak. The height of the second peak remains relatively unchanged from the base experiment (2.16a).

2.5.6 Streamer inception under different conditions

The experiments described above show that in a specific condition, 17 kV HV amplitude with a repetition frequency of 2 Hz and a working pressure of 500 mbar, an electron which initiates a streamer can originate from three different sources. The question that we now need to address is whether these conclusions are generic or only valid for these specific experiment conditions. Hence, we repeated some of the experiments for combinations of a different repetition frequency (0.2 Hz), pressure (250 and 750 mbar), and voltage (12 kV) to see whether the observations still hold.

Figure 2.17a shows that for a repetition frequency of 0.2 Hz only one peak is present in the t_{inc} histogram. The sources for the first and third peak in figure 2.9 do not seem to play a role when the repetition frequency is decreased. This may be due to the increased time between HV pulses where no electric field is applied across the gap. During this time ion recombination processes can remove the detaching negative ion species. This again indicates that the source of the second peaks has a long lifetime.

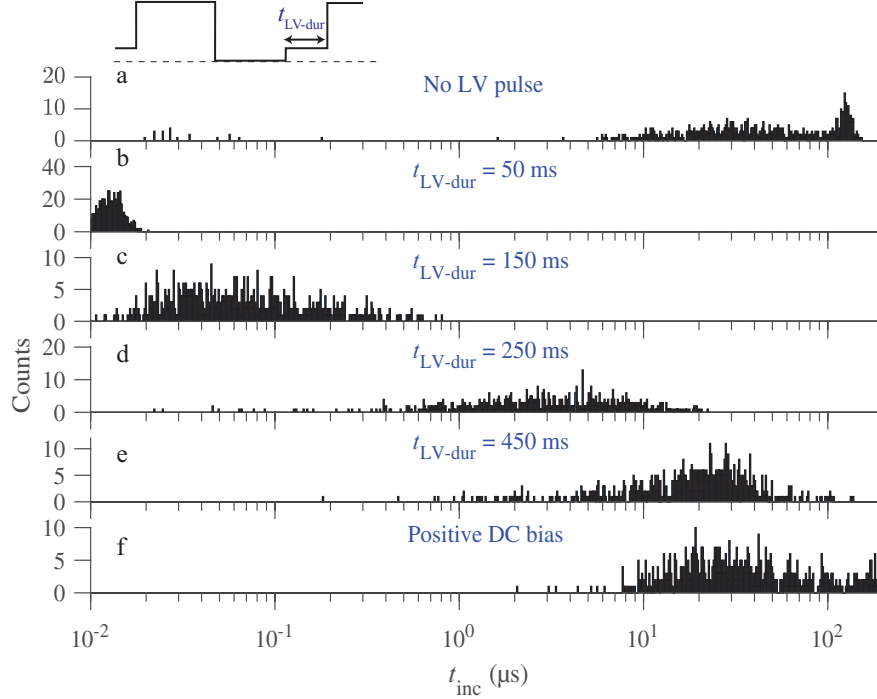


Figure 2.16: Histograms of discharge inception time t_{inc} for 600 discharges produced by applying a 300 V pulse for $t_{\text{LV-dur}} =$ b) 50, c) 150, d) 250, and e) 450 ms, for a) no LV pulse and f) a DC bias before a 17 kV pulse of 10 ms with a repetition frequency of 2 Hz.

Figure 2.17b shows the t_{inc} histogram for an increased pressure of 750 mbar. We observed similar peaks as in the baseline experiment (figure 2.9), but the third peak shifted to higher t_{inc} . The drift time of ions will scale inversely with the pressure which can explain the shift of the third peak to higher t_{inc} for a higher pressure. When the pressure is lowered to 250 mbar we see that most inception takes place at $t_{\text{inc}} < 0.1 \mu\text{s}$. It does not seem reasonable to attribute this shift of t_{inc} from $125 \mu\text{s}$ to $0.1 \mu\text{s}$ due to a halving of the pressure. The attachment time would also not be decreased enough to allow for free electrons to exist when an HV pulse is applied and thus triggering a fast inception of the discharge. A possible explanation is that the detaching negative ions are not converted to O_3^- (stable) or neutralized through recombination reactions as quickly. This would result in more detaching negative ions to remain from the previous discharge. The density of detaching negative ions would increase over time (also in the ionization zone) which will increase the chance of fast discharge inception.

When a lower HV (12 kV) is applied (still higher than the inception voltage, probability of inception = 100%), the first peak seems to have almost disappeared,

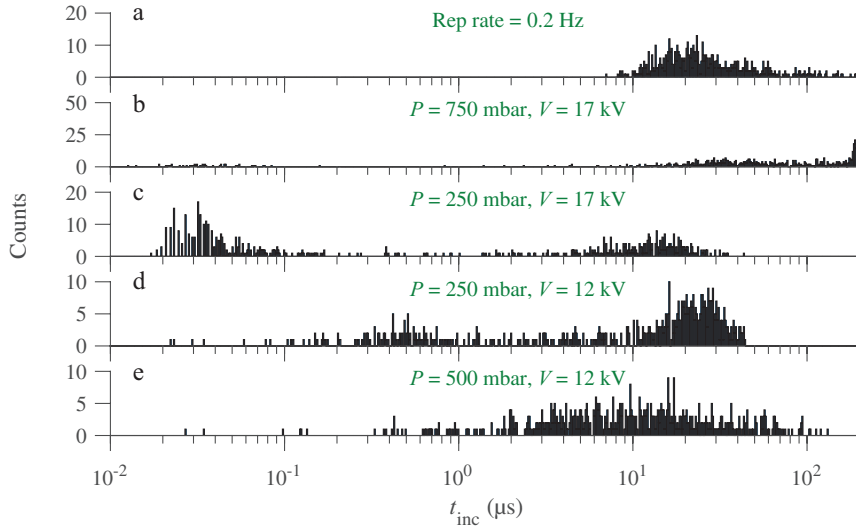


Figure 2.17: Histograms of discharge inception time t_{inc} for 600 discharges with a different experimental setup than the rest of the experiments. a) A repetition frequency of 0.2 Hz instead of 2 Hz, b) A pressure of 750 mbar instead of 500 mbar, c) A pressure of 250 mbar instead of 500 mbar, d) A pressure of 250 mbar and HV of 12 kV instead of 500 mbar and 17 kV, e) an HV of 12 kV instead of 17 kV.

as shown in figures 2.17c and d. This may be caused by the smaller ionization zone around the pin electrode which would reduce the chance of having a detaching negative ion in this zone when an HV pulse is applied. This would reduce the occurrences of fast discharge inception (first peak).

In summary, any change in experimental setup which would change the density and distribution of species in the streamer channel will have an effect on the t_{inc} histogram. Parameters that can be changed and will have an influence are: gap distance, applied voltage, gas pressure, repetition frequency, etc.

2.6 Summary and open questions

We investigated the inception process of repetitive pulsed discharges by measuring the distribution of discharge inception times t_{inc} after the start of the HV pulse. We applied 17 kV pulses of 10 ms duration with a repetition frequency of 2 Hz to 500 mbar synthetic air and produced a histogram of inception times t_{inc} , which shows three distinct peaks. By applying LV pulses between the HV pulses, these peaks could be shifted in time or changed in magnitude. We provide theoretical arguments and numerical calculations aimed at identifying different electron producing processes that would explain each peak. However, open questions remain.

We start with two theoretical considerations.

First, in section 2.5.2 it is argued that a single uniformly distributed electron source would create only one early peak, with an initial increase related to the voltage rise time or to the electron detachment time from an oxygen ion, and then with a continuous decay of the inception probability in time. So the different peaks suggest different physical mechanisms.

Second, after a streamer discharge in synthetic air, electrons attach to oxygen molecules on a time scale of 10 to 100 ns between the HV pulses, and the negative oxygen ions can rapidly detach electrons and start a discharge in the high field zone near the electrode during the next HV pulse. We estimate the O_2^- density in a decaying streamer channel as 10^5 cm^{-3} at the beginning of the next HV pulse. This number is based on the assumption of fast electron attachment to form O_2^- , and on diffusion and recombination of positive and negative ions. However, to reach inception times comparable to experiment, the O_2^- density needs to be as low as 10 cm^{-3} , i.e., 4 orders of magnitude smaller. A possible explanation is that more plasma chemistry has to be added, in particular, that further ion conversion takes place to form the ozone ion O_3^- and NO_3^- . These ions are rather stable, and therefore an effective electron sink. This question needs further investigation in the future.

Concerning the physical processes causing the distinct peaks, we find that the first and the third peak are susceptible to LV pulses, consistent with the drift of negative oxygen ions; in the high field zone near the electrode these ions can detach an electron and create an ionization avalanche. However, to form these two peaks, the ions need to be quite inhomogeneously distributed. The first peak would be caused by a large ion concentration in the high field zone near the electrode (possibly due to the glow during most of the previous HV pulse), and the third peak would be caused by another large ion concentration starting at a distance of about 1.5 cm from the electrode. However, to create the well separated peaks, the two regions

with high ion density would need to be clearly separated by a region with very low ion density. It is not clear how such a concentration profile would arise.

The second peak does not shift in time with an LV pulse, which suggests that this electron source is electrically neutral. A continuous, field independent electron source due to Penning ionization could be an explanation, but the lifetime of the Penning ionizing species $N_2(A)$ and $N_2(a')$ are determined by quenching reactions with O_2 and these have timescales on the order of 10 to 100 ns which makes Penning ionization an unlikely hypothesis. Another explanation could be the presence of quasi-neutral ion patches which cannot be separated by an LV pulse due to space charge effects. The negative ions in these patches can drift in the HV field towards the pin electrode and initiate a discharge by detaching an electron. It is not clear yet if such quasi-neutral patches would be created by a discharge.

Applying a negative LV pulse did not remove the first peak which we argument to be caused by negative ions close to the pin electrode. Secondary emission from the electrode could happen due to impact of positive ions, but in the electric field of the LV pulse the kinetic energy of these ions would be much lower than the work function of the electrode material. Other secondary emission reactions will need to be investigated in the future to understand this observation better.

The open questions which arose from this research are listed as follows:

1. If the first peak is caused by detaching O_2^- -ions, why can it be removed by applying a positive LV pulse? O_2^- -ions from further away in the gap should move towards the pin electrode.
2. If the first peak is caused by detaching O_2^- -ions, why can it not be removed by applying a negative LV pulse (or even a negative DC bias)?
3. What causes the second peak? It seems to not be influenced by any LV pulse applied. It is the only peak present when the repetition frequency is decreased to 0.2 Hz. It accounts for 61% of the discharge inceptions.
4. Simulations show that the third peak can be produced by an inhomogeneous O_2^- -ion distribution. What causes this spatial inhomogeneity?

3

Investigating CO₂ streamer inception in repetitive pulsed discharges

Abstract

In this study, we investigate the responsible species and processes involved in repetitive pulsed streamer inception in CO₂. We applied a 10 kV high-voltage pulse with a repetition frequency of 10 Hz and pulse width of 1 ms to a pin electrode which is placed 160 mm apart from the grounded plane electrode. We measured the inception times (delay between the rising edge of the high-voltage pulse) by a photo-multiplier tube for 600 high voltage cycles. We observed one peak in the histogram of inception times with a median of 1.2 μ s. To identify the source of this peak, we applied a negative or positive LV pulse before the main HV pulse to manipulate the leftover space charges. Three different phenomena are observed: 1) drift, 2) neutralization, and 3) ionization in the LV pulse. At low LV amplitude and pulse width, the peak starts to drift toward the faster and slower inception times under a positive and negative LV pulse, respectively. However, under the same LV pulse configuration for positive and negative LV pulse, the observed shift in inception times is not the same. We present a hypothesis to explain this asymmetry based on the difference of the detachment processes between air and CO₂.

This chapter is based on [S. Mirpour and S. Nijdam. "Investigating CO₂ streamer inception in repetitive pulsed discharges." submitted to Plasma Sources Science and Technology]

3.1 Introduction

Streamers are widely explored in different gases because of their importance in various fields such as high-voltage engineering and atmospheric electricity [1], [47], [51], [87]–[91]. Recently, CO₂ gas has been considered as a possible candidate for high-voltage switchgear, since the gas currently used for insulation and switching, SF₆, is an extremely strong greenhouse gas [92], [93]. Also, there is strong evidence that lightning might exist in the Martian atmosphere which mostly consists of CO₂ [6], [94]. Hence, it is important to understand the physics behind streamer inception and development processes in this gas. Streamer inception voltage and time have been mostly studied in air [57], [66], [95], [96]. There are not many studies of discharge inception in CO₂ (see below), and the current understanding of the streamer inception process is very limited. This study investigates the streamer inception process in CO₂ in more detail.

By applying positive high-voltage pulses to an electrode, electrons start to drift opposite to the electric field. When such an electron reaches an area where the ionization rate is higher than the attachment rate, it can start to replicate, although this is of course a stochastic process. The electron density then grows until the formed space-charge becomes large enough to transform into a streamer. The number of electrons required for this transition can be derived from the so-called Meek criterion [20], [58]. In our previous work [95], we hypothesized that in synthetic air, the very first electron to trigger the streamer inception process can come from three different sources: free electrons, O₂⁻ detachment, or from reactions of neutral species. We showed that, in repetitive discharges, the leftover charges from the streamers likely build up an in-homogeneous distribution of ions in front of the anode, which produces a peak in the streamer inception distribution times histogram. By adding a low-voltage (LV) pre-pulse before the main high-voltage (HV) pulse we could manipulate and drift this in-homogeneous ion cloud towards or away from the anode, depending on the LV pulse polarity. Thus, the ions will be at a new position at the beginning of the HV pulse which results in a shift of the observed peak in the time distribution histogram. From these shifts, we can derive the mobility of ions and identify the source. Photoionization is another well-known source of initial seed electrons in air. However, no efficient photoionization mechanism is known for CO₂ due to the rapid absorption of photons in this gas [97]. Therefore, in CO₂, detachment of electrons from negative ions is the most probable source of initial free electrons.

The statistical time lag for CO₂ discharges has been studied by Seeger et al. [98]. They showed that, at pressures higher than ambient pressures, by increasing the applied voltage, the discharge inception time lag decreases and reaches as low as 100 ns. They found a fairly good agreement between the theoretical prediction of streamer inception fields (considering the ionization integral as 13) and actual observations. However, that study offers little in the way of examining which species are playing an important role in inception.

Wang et al. [99] investigated the critical breakdown field for CO₂ discharges at elevated temperatures. They showed that at room temperature the reduced breakdown electric field in CO₂ is about 86 Td. Increasing the temperature leads to CO₂ dissociation, which leads to more collisions between CO and O⁻ creating electrons through associative detachment. This will influence the effective ionization rate, contributing to a significant drop in the critical breakdown field. At room temperature this mechanism is insignificant due to the low dissociation degree. Furthermore, O⁻ is turned into a relatively stable ion, CO₃⁻, by the cluster stabilization process. Hence, the main electron source and sink are electron impact ionization and dissociative attachment to CO₂ through $e^- + \text{CO}_2 \rightarrow \text{CO} + \text{O}^-$.

This study aims to clarify the role of different species in the streamer inception process in CO₂ by adding a pre-pulse to manipulate the charge distribution before applying the main HV pulse. The effects on these on inception time histograms can give great insights in the relevant processes. This chapter is organized as follow: In section 3.2 we describe the method, section 3.3 discusses the results and gives an hypothesis based on the different LV pulse configurations. Finally, in section 3.4 we summarize the chapter and provide the conclusion.

3.2 Set-up and Methods

3.2.1 Experimental conditions

All experiments in this study were performed in a point-to-plan geometry (figure 3.1) in which the powered electrode, (anode with a tip radius of about 100 μm), is separated 160 mm from the grounded electrode. The anode is powered by a circuit comprising an HV solid state switch (Behlke, HTS 651-15-SiC-GSM) and a 1 nF capacitor. With this configuration, we can produce repetitive pulsed waveforms with an amplitude of 10 kV, pulse widths of 1 ms, rise times of 40 ns, and repetition rates of 10 Hz. The reason we chose this repetition rate and pulse duration is to have only one discharge within the duration of an HV pulse and 10 kV was close to the streamer inception voltage. We did not observe any dependency of

streamer inception on pulse duration at this frequency. The background pressure was 10^{-6} mbar, and for each experiment the vessel was filled to 300 mbar with CO_2 (purity level of 99.9999 %).

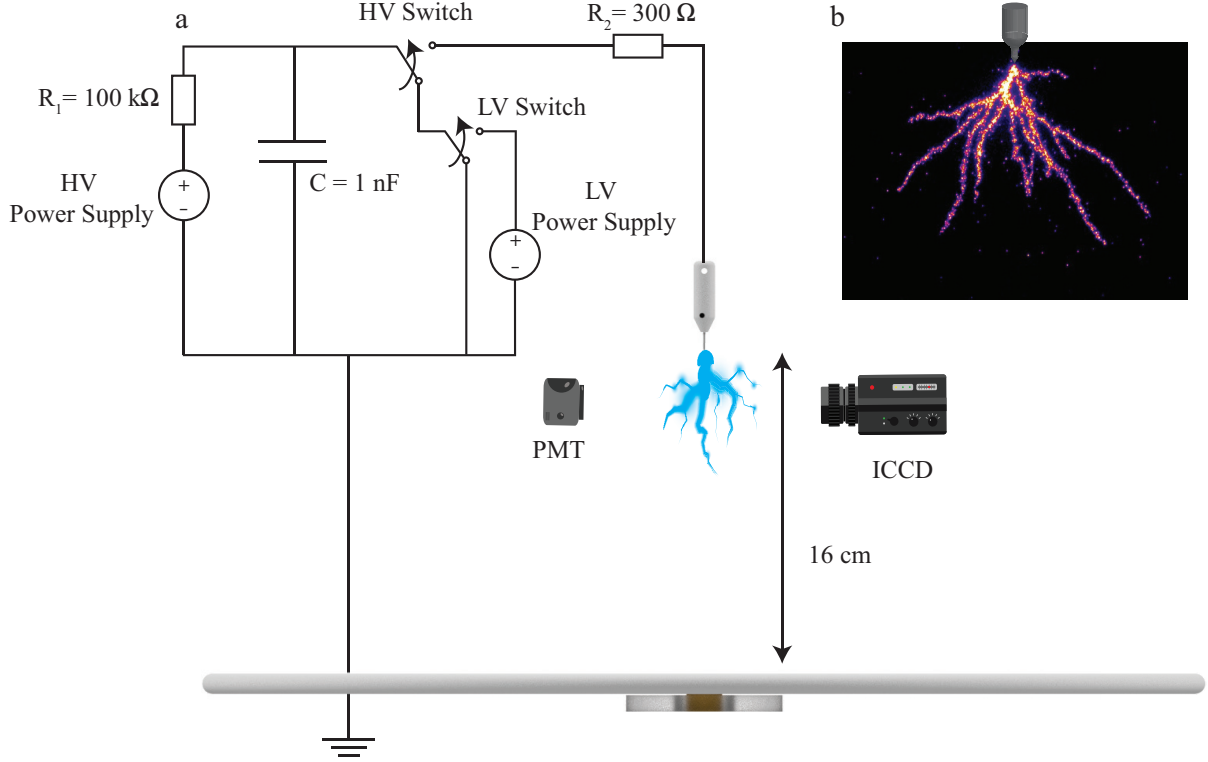


Figure 3.1: a) Schematic view of the experimental setup with HV power supply connected to the anode (not to scale). b) ICCD image of the CO_2 discharge at 300 mbar with HV amplitude of 10 kV and repetition frequency of 10 Hz.

To investigate the influence of residual charged species on streamer inception, an LV pre-pulse was applied before each HV pulse. To apply the LV pre-pulse, the negative input of the HV pulser was connected to a second pulser, comprised of another solid-state HV switch (Behlke, HTS 181-01-HB-C) and a 1 nF capacitor. This could produce a pre-pulse which attaches to the main HV pulse and has an amplitude V_{LV} between 0 and 8 kV and a pulse width t_{LV} between 0 and 100 ms (c.f. figure 3.2).

3.2.2 Measuring inception time t_{inc}

To measure the streamer inception time (t_{inc}), we used a photo-multiplier tube (PMT, H10720-1 10 Hamamatsu) placed behind a window of the vessel. The response time of the PMT is less than 2 ns. The output signal was transferred to a 12-bit HD

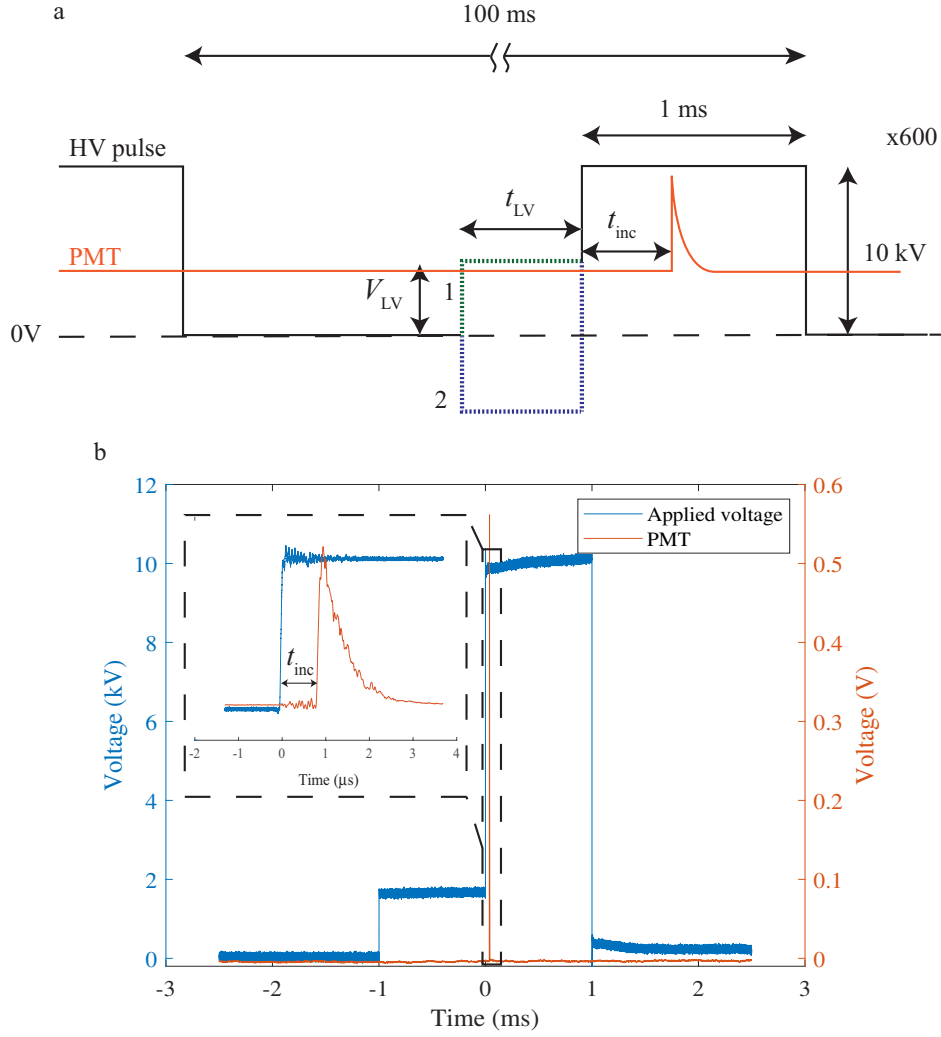


Figure 3.2: a) Scheme of applied HV waveform with 1. positive and 2. negative attached LV pulse. b) Typical applied HV and LV voltage with PMT waveform output.

6104 Teledyne Lecroy oscilloscope with a sample rate of 1 GS/s. We repeated this measurement for 600 HV cycles per setting. Note that we consistently observed only one discharge inception event per 1 ms HV pulse. For each cycle, t_{inc} was determined as the temporal delay between the HV pulse reaching 10% of its maximum and the PMT waveform reaching 10% of its maximum (see figure 3.2). The total error in t_{inc} is estimated at less than 10 ns. Streamer inception is here defined as an HV pulse in which the PMT signal shows a peak three times above the average background noise.

From the measured t_{inc} values, a histogram is made using a logarithmic binning function, MATLAB function: `logspace(log10(0.01), log10(max(data)), 700)`, which divides the data into 700 bins starting from 10 ns. The acquisition window was 1 ms for all experiments. In the histogram figures, we indicate the inception probability ($Prob$), which is the number of pulses for which streamer inception was

detected, divided by the total number of HV pulses (600). An intensified CCD (ICCD, Stanford Computer Optics 4QuickE) with a nanosecond time gate and a Nikkor UV 105 mm lens f/4.5 was used to image the streamers. The streamers in figure 3.1.b are rendered in a false-colour scale for clarity. We found that in each case that a peak was detected by the PMT, the ICCD image always showed a developed streamer.

3.3 Results and discussion

3.3.1 Baseline experiment and general phenomenology

To gain an overview of phenomenology, we applied an HV pulse (10 kV amplitude with a duration of 1 ms) and an LV pre-pulse (with a duration of 25 μ s and varying V_{LV}) to the electrode. We repeated this 600 times at a repetition frequency of 10 Hz. Figure 3.3 shows the histogram of t_{inc} on a logarithmic scale where the size of the time bins is scaled as $\log t$. Figure 3.3.a shows the baseline experiment with no LV pulse where t_{inc} forms a single peak around 1-2 μ s. Application of a positive LV pulse before the main HV pulse led to three observations. For V_{LV} up to 500 V (Drift, figure 3.3.a-c) the t_{inc} peak started to shift to lower values, below 70 ns. Increasing V_{LV} more (Neutralization, figure 3.3.d-g) caused the peak to shift to higher values around 150 ns. Finally, an LV pulse of 8 kV (Ionization during LV pulse, figure 3.3.h) again shifted the peak to 50 ns. Note that this phenomenon depends on an interplay between V_{LV} and t_{LV} and therefore we introduce $S = t_{LV} \cdot V_{LV}$ as the main parameter in the phenomenology. Below, each of the observed phenomena is elaborated in a separate section.

3.3.2 Drift due to applying an LV pulse

Since we mostly observe one peak in the t_{inc} histogram, the median values (\tilde{t}_{inc}) were calculated and are plotted against V_{LV} in figure 3.4). To test the role of leftover charges on the inception, we applied both positive and negative LV pulses immediately before the main HV pulse. Figure 3.4 shows the effects of these LV pulses on \tilde{t}_{inc} , where for negative the LV pulses, a pulse width t_{LV} of 10 ms was used, while for the positive LV pulses this was 10 μ s, a factor 1000 lower. In the electric field imposed by a positive LV pulse, the negatively charged species will drift towards the electrode and thereby initiate discharges quicker after the HV pulse is applied. The results show that for every 100 V of applied positive LV pulse, we observed a 94 ns shift in \tilde{t}_{inc} .

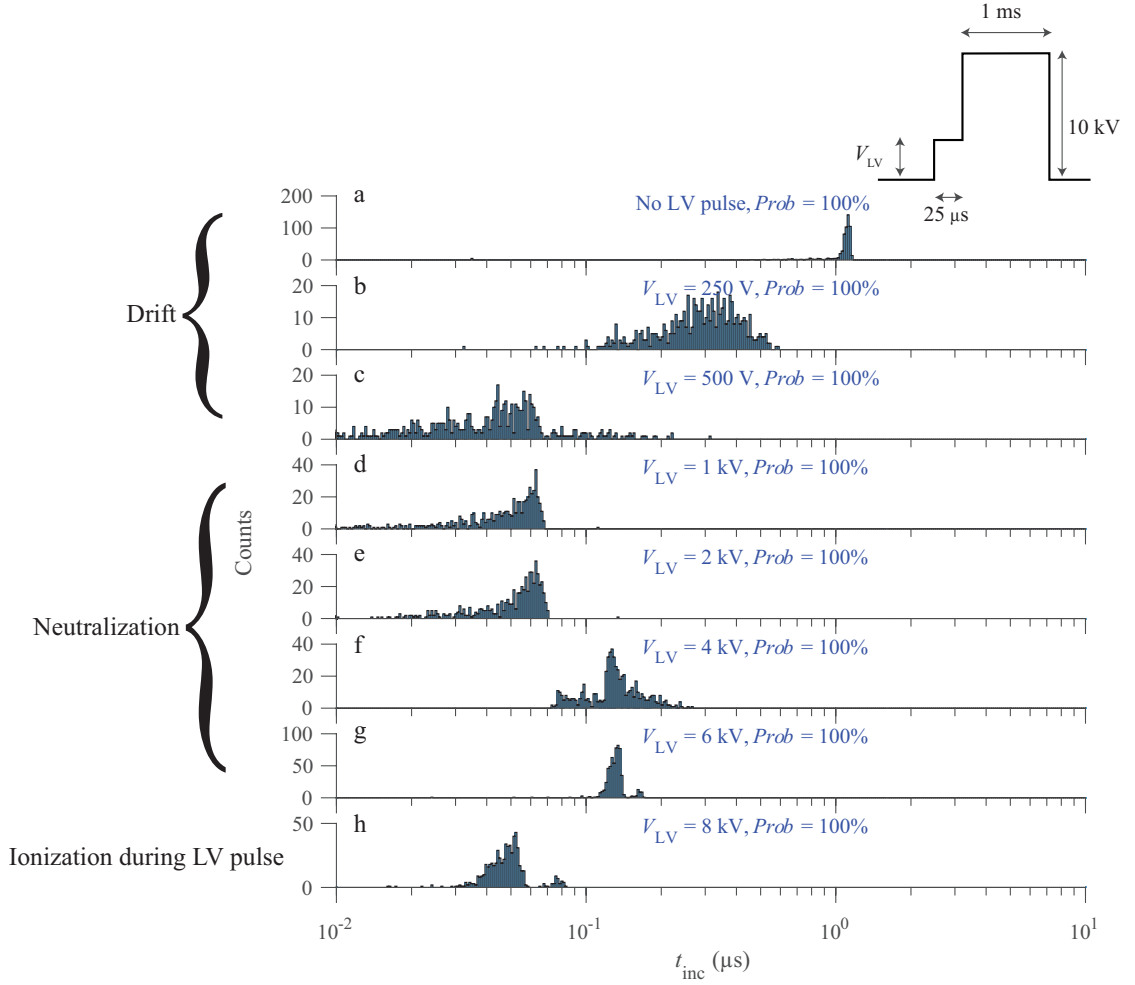


Figure 3.3: Histograms of discharge inception time t_{inc} for 600 discharges produced a) for no LV pulse and b-h) by applying a 25 μs duration LV pulse with the indicated voltage before a 10 kV HV pulse of 1 ms with a repetition frequency of 10 Hz. Inception probabilities are 100% for each case, as indicated.

We would expect to have the same drift magnitude in opposite direction for a negative LV pulse. Interestingly however, a negative LV pulse with a 10 μs pulse width leads to a negligible shift in \tilde{t}_{inc} . As can be seen in Figure 3.4, to have a 90 ns shift in \tilde{t}_{inc} we need to apply a 10 ms, 100 V negative LV pulse instead of a 10 μs , 100 V pulse. Note that \tilde{t}_{inc} is not fully linear with V_{LV} so the mentioned numbers are averages.

To investigate the effect of the duration of the LV pulse, we fixed V_{LV} to 1 kV and -1 kV and varied t_{LV} . Figure 3.5 shows the \tilde{t}_{inc} shift when applying positive and negative LV pre-pulses. For negative LV pre-pulses, a 1 ms increase in t_{LV} leads to a 86 ns decrease in \tilde{t}_{inc} . Similar to what we observed in the previous experiment \tilde{t}_{inc} the reverse effect for positive pre-pulses is also present but again roughly a thousand times stronger; to have a 92 ns shift in \tilde{t}_{inc} we need to apply a 1 kV positive pre-pulse

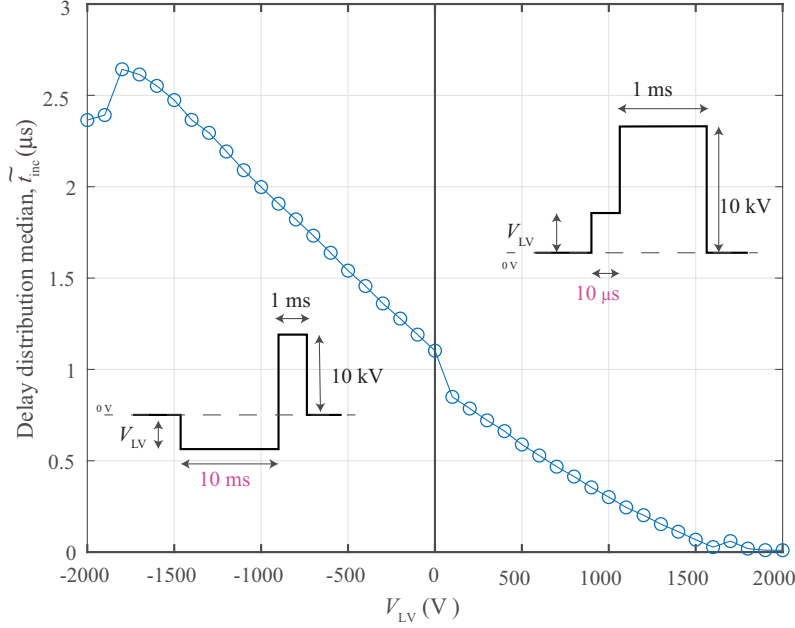


Figure 3.4: Median of the delay histograms, \tilde{t}_{inc} , produced by applying left) negative and right) positive LV pulses with different V_{LV} . For the negative and positive LV pulse, t_{LV} is fixed and set to be 10 ms and 10 μ s, respectively.

with $t_{LV} = 1 \mu$ s instead of 1 ms. Note that in our previous experiments in air [95] the effects of positive and negative pre-pulses were nearly equal, but of course opposite in direction. Below, we give a hypothesis to explain this large asymmetry of three orders of magnitude between the effects of positive and negative pre-pulses in CO_2 .

Hypothesis

In order to explain the surprising asymmetry between the effects of positive and negative pre-pulses in CO_2 (and not in air), we hypothesize that this is caused by the detachment process in CO_2 .

During an HV pulse, energetic electrons near the tip cause CO_2 dissociation by direct electron impact. The dissociative attachment reaction rate increases in higher electric fields and causes the production of CO and O^- near the electrode [100]. Thus, in this specific region, both these species are available and recombination of O^- and CO can liberate an electron through associative detachment at any time during and between voltage pulses. During an HV pulse, such an electron can enter the ionization region and initiate a discharge. If there is a "charged species patch": a volume containing positive ions, negative ions and free electrons, located some distance from the tip, like we also concluded in [95], then the electrons from this region can again explain the peaked distribution of the baseline experiment. Note that from our results we cannot determine the shape of the charged species patch.

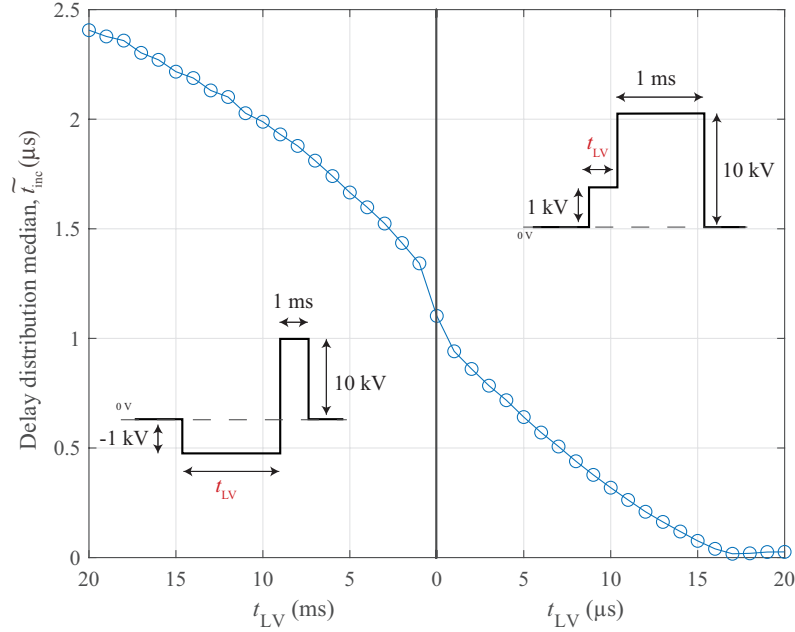


Figure 3.5: Median of the delay histograms, \tilde{t}_{inc} , produced by applying left) negative and right) positive LV pulses with different t_{LV} . For the negative and positive LV pulse, V_{LV} is fixed and set to be -1 kV and 1 kV, respectively. Note the difference in time units between left-hand and right-hand side on the horizontal axis.

It could be a thin layer, a localized patch, or a large region extending away from the electrode tip. We only know that it has a quite sharp boundary towards the electrode.

When applying a positive LV pulse, all negative species in the charged species patch will drift toward the tip. Since ions are much heavier than electrons, electron drift is more prominent and therefore the electron mobility will determine the effect of the LV pulse on inception behaviour. A negative LV pulse with the same S value will also push away the electrons from their initial position for roughly the same distance as the positive LV pulse. However, the much less mobile ions can still produce electrons by associative detachment and remain much closer to the tip than the drifted electrons due to their lower mobility. During the main HV pulse inception times are determined by the closest electrons and not the far-away ones. Therefore, for positive LV pulses, electron drift dominates the effect, while for negative LV pulses, negative ion drift does so.

To elaborate on this hypothesis, we have calculated the drift time of electrons and O⁻ ions in CO₂ from a distance z to the pointed electrode (at $z=0$) on the axis of symmetry. The drift time was calculated by

$$t_{\text{drift}}(z) = \int_z^0 \frac{1}{\mu(E(z'))E(z')} dz', \quad (3.1)$$

where μ , the mobility of the respective species, is derived from [101] for electrons and [102] for ions, and $E(z)$, the electric field on the axis (see figure 3.6), is calculated by a COMSOL Multiphysics simulation [80]. The corresponding drift times for electrons and ions are shown in figure 3.7. It should be noted that since mobility data for electrons and ions in CO_2 is not available for low electric fields, the given estimations are based on constant mobility in these fields (dashed lines in figure 3.7).

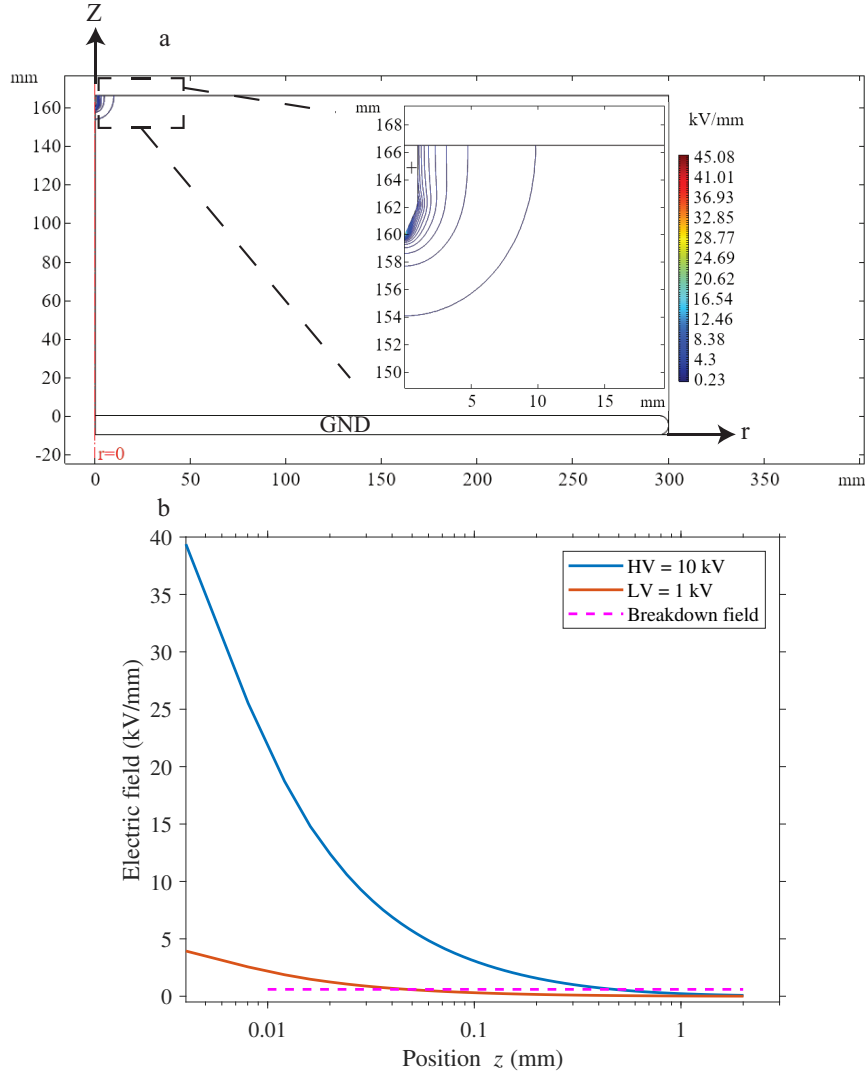


Figure 3.6: a) The computational domain for the electric field computation with COMSOL (included are electric field contour lines). The grounded electrode is placed at $x = 0$ and the electrode tip at $x = 160$ mm. b) The electric field on the symmetry axis as a function of distance for the first 20 mm from the tip for $V_{\text{HV}} = 10$ kV and $V_{\text{LV}} = 1$ kV. The breakdown electric field (dashed line) is 0.66 kV/mm at 300 mbar and is taken from Bagheri *et al.* [97].

Let us now assume that we indeed have a localized charged species patch containing, amongst other species, negative ions and free electrons. Figure 3.7

enables us to investigate the initial and post-drift positions of the ion and electron distributions, \tilde{t}_{inc} in the baseline experiment ($V_{\text{LV}} = 0$) is $1.2 \mu\text{s}$. Figure 3.7 shows that at $V_{\text{HV}} = 10 \text{ kV}$, electrons should be generated at 25 mm from the tip to have enough time to drift and reach the tip. Hence, we can estimate the initial position of the boundary of the charged species patch to be about 25 mm away from the tip. Note that a possible detachment time is not included in this calculation. Moreover, it is assumed that an electron should reach the tip of the electrode to initiate a discharge.

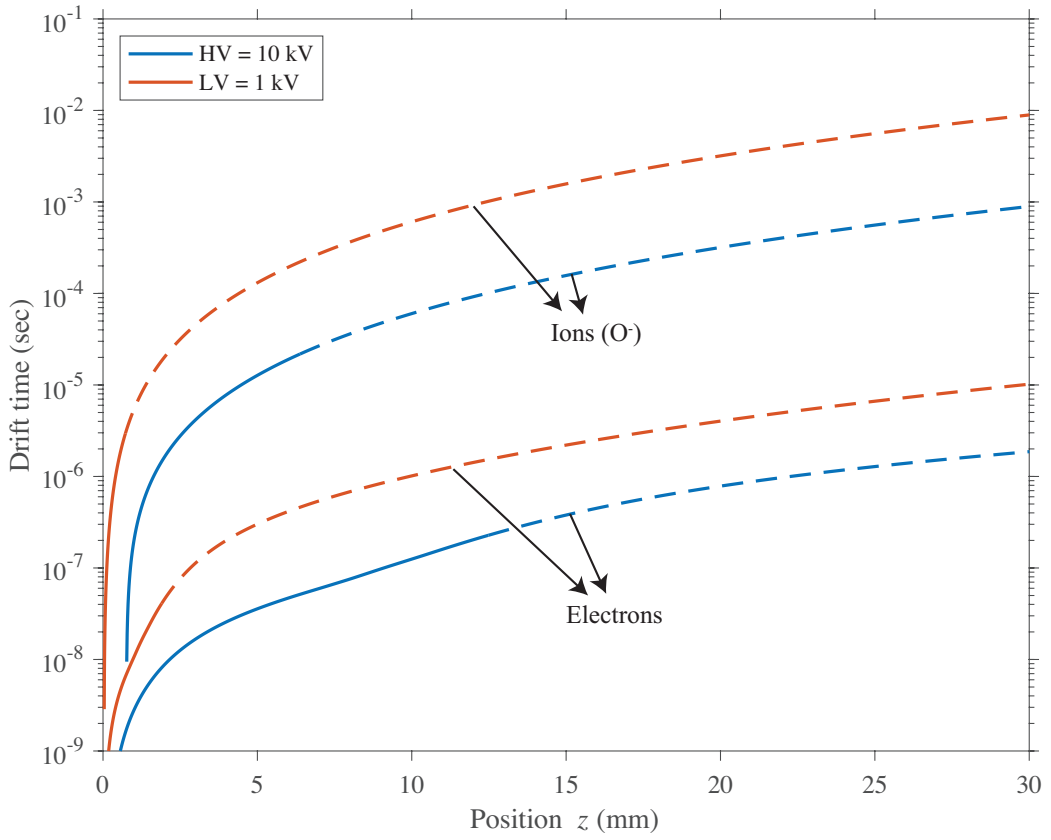


Figure 3.7: Drift time calculated using equation (3.1) on the axis of symmetry of electrons and O^- ions from a distance x to the electrode at $x = 0$ when a voltage of $V_{\text{LV}} = 10 \text{ kV}$ or $V_{\text{LV}} = 1 \text{ kV}$ is applied across the gap. The mobilities in the unavailable electric field ranges are assumed constant, and the calculated drift times in those ranges are plotted as dashed lines.

Under a positive LV pulse (figure 3.8.a) with $S = 1 \text{ mVs}$, the corresponding electron drift distance is around 2 mm toward the electrode tip. During the main HV pulse, electrons with this new position require $1.01 \mu\text{s}$ to reach the ionization zone. Therefore, we expect to observe around 182 ns shift in the \tilde{t}_{inc} peak. This is relatively close to our observation from the right-hand side of figure 3.5, where the

drift for every $S = 1$ mVs positive LV pulse was 92 ns. According to equation 3.1, the ion drift during application of 1 kV and 1 μ s is less than 1 μ m.

Under a negative LV pulse with $S=1$ mVs (figure 3.8.b), electrons drift outwards roughly the same distance as they drift inwards when a positive LV is applied. Ions which are nearly immobile during $S=1$ mVs, are still re-generating new electrons in the absence of the drifted electrons. This procedure also continues after the LV pulse is applied and at the beginning of the main HV pulse. The newly generated electrons are closer to the tip than their drifted cousins. Therefore, they have more chance to initiate a discharge. This supports our observation that no shift was measured in \tilde{t}_{inc} after an LV pulse was applied with $S = 1$ mVs. O^- ions only start to drift noticeably under a stronger electric field. Ions under a negative LV pulse of $S=1$ Vs drift out about 1 mm from their initial position (figure 3.8.c). At the beginning of the main HV pulse, the electrons newly generated from the ions that are located in a new position start to drift toward the tip and imitate the discharge. According to equation 3.1, the time that electrons need to drift back 1 mm is 115 ns. This is very close to our observation in figure 3.5 where the \tilde{t}_{inc} shift under an LV pulse with a $S=-1$ Vs is 92 ns.

In our previous study [95], we showed that O_2^- in synthetic air was responsible for one of the peaks of the t_{inc} histogram. This peak showed a symmetric shift for positive and negative LV pulses. A possible explanation for this difference between air and CO_2 can be the different electron detachment mechanisms. The detachment rate of O_2^- in air depends strongly on the electric field (see figure 3.9). Therefore O_2^- must be in a high field region to detach an electron [61]. However, for CO_2 the detachment rate decreases with electric field [103] (see figure 3.9). The reason is that associative detachment in CO_2 proceeds through autodetachment of the CO_2^- complex in a short period. In higher fields and energy, formation of this complex is less probable because of the shorter collision time. Thus, the associative-detachment reaction in CO_2 is more likely to release electrons in the low fields regions far away from the electrode tip. Therefore, during a low S value LV pulse, detached electrons can move and show up their drift in \tilde{t}_{inc} histogram.

One question that can be raised in this section concerns the attachment of electrons during the drift. According to our hypothesis, electrons should drift about 25 mm to reach the ionization zone. To calculate the attachment time, we exert a simple analysis using the BOLSIG+ solver [82], [83] with the reactions shown in table 3.1 as input. Results show that at the electric field around 1 Td at 2.5 mm, where the initial electrons release from the charged species patch, the attachment time is 1.5 μ s

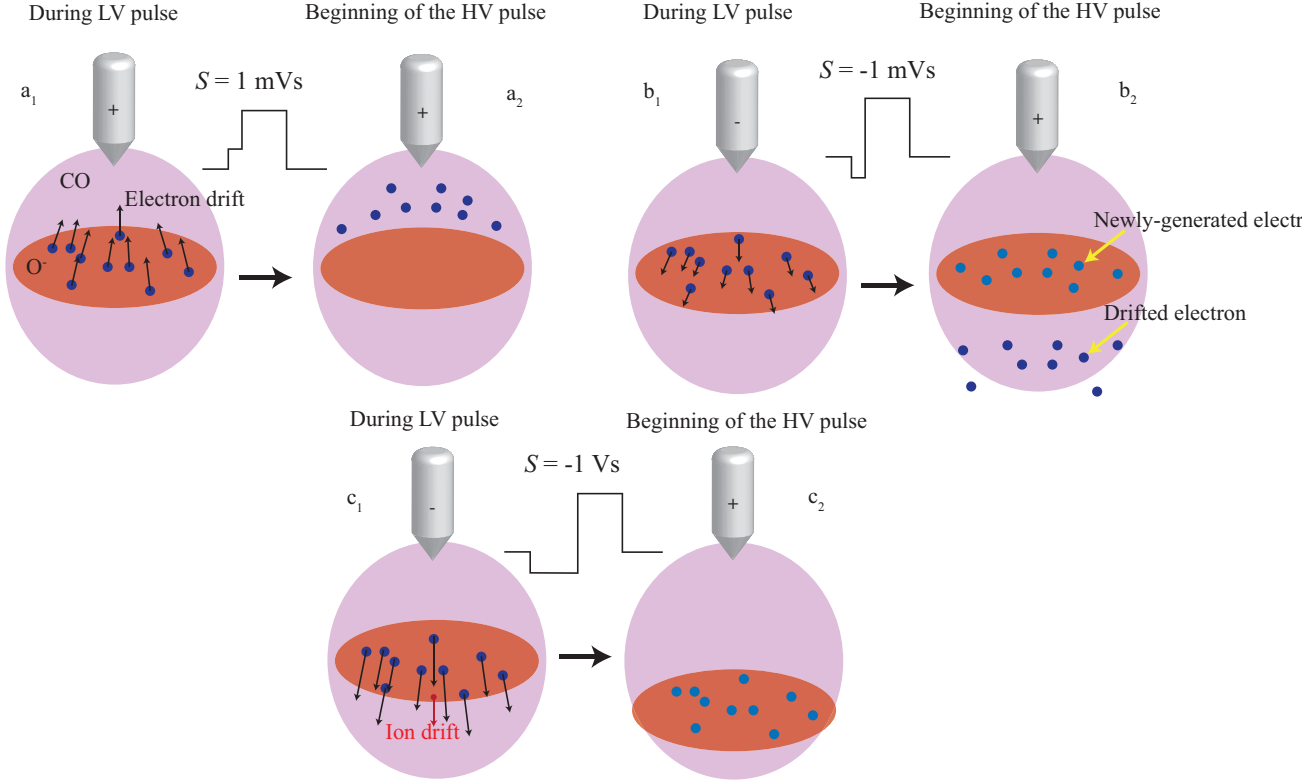


Figure 3.8: Visual explanation of electrons and ions drift under positive and negative LV pulses with $S =$ a) 1 mVs, b) -1 mVs, and c) -1 Vs. In each figure, 1 shows the drift during an LV pulse and 2 shows the new position of electrons and ions at the beginning of the HV pulse.

which is slightly higher than the inception time. Therefore, this gives enough time for most of the electrons to approach the ionization zone without being attached.

From the width of the inception time distribution in the baseline experiments and equation (3.1) we can estimate that the thickness of the charged species patch is about 0.2 cm. When we consider the charged species patch as disk of this thickness and with a diameter of 2.5 cm, its volume is approximately 1 cm^3 . With the following equation

$$k_{detachment} \cdot [CO] \cdot [O^-] = 1/(N \cdot t), \quad (3.2)$$

where $k_{detachment} = 5.5 \times 10^{-10}$ [99], we can estimate that in $t = 1.5 \mu\text{s}$ attachment time, in order to have 1 electron available in this volume of ($N = 1/\text{cm}^3$), the required concentration product of $[CO] \cdot [O^-]$ should be of the order of magnitude 10^{15} cm^{-6} . When we assume that the concentrations of $[CO]$ and $[O^-]$ are roughly equal, the density of each species should be $10^7 - 10^8 \text{ cm}^{-3}$ in order to supply the required electrons for inception. This is a feasible number for these densities in the charged species patch.

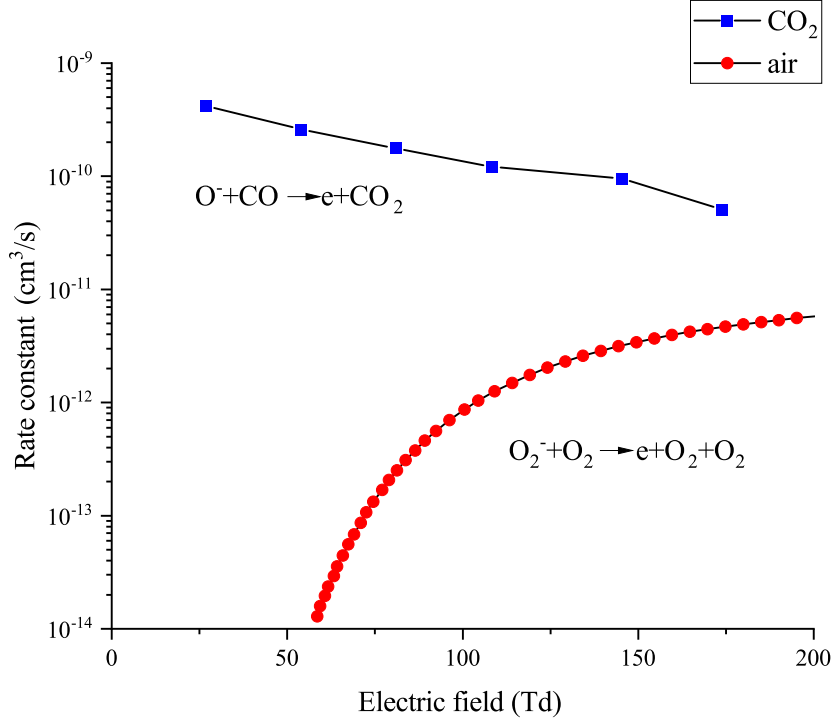


Figure 3.9: Rate constant of the dominant detachment processes in air and CO₂. For air data was taken from [61] and for CO₂ from [103].

Table 3.1: List of plasma-chemical reactions used for calculation the ionization and attachment coefficients. Cross-sections are taken from Itikawa database [72].

Elastic collision	$e^- + \text{CO}_2 \rightarrow e^- + \text{CO}_2$
Ionization	$e^- + \text{CO}_2 \rightarrow 2e^- + \text{CO}_2^+$
	$e^- + \text{CO} \rightarrow 2e^- + \text{CO}^+$
Attachment	$e^- + \text{CO}_2 \rightarrow \text{CO} + \text{O}^-$

3.3.3 Neutralization and ionization during longer LV pulse durations

In this section we investigate higher values of S .

Positive LV pulse

Above a certain value of S , t_{inc} reaches its minimum value and it is not possible to have faster inception because electrons and negative ions will have drifted all the way to the the electrode. Figure 3.10 shows that applying a 250 V and 50 ms LV pulse was enough to initiate a discharge during the rise-time of the HV pulse. Increasing V_{LV} to 1.5 kV was enough to drift all negative ions close to the tip. This can be verified by the mobility data in figure 3.7. Above this V_{LV} , ions

reside around the electrode for a long time, where they will be slowly neutralized. Moreover, the inception probability, $Prob$, decreases with increasing V_{LV} which shows the lack of initial electrons available to initiate a streamer. We also observed this effect in our previous experiments in synthetic air [95] where applying an LV pulse for a long time increased t_{inc} .

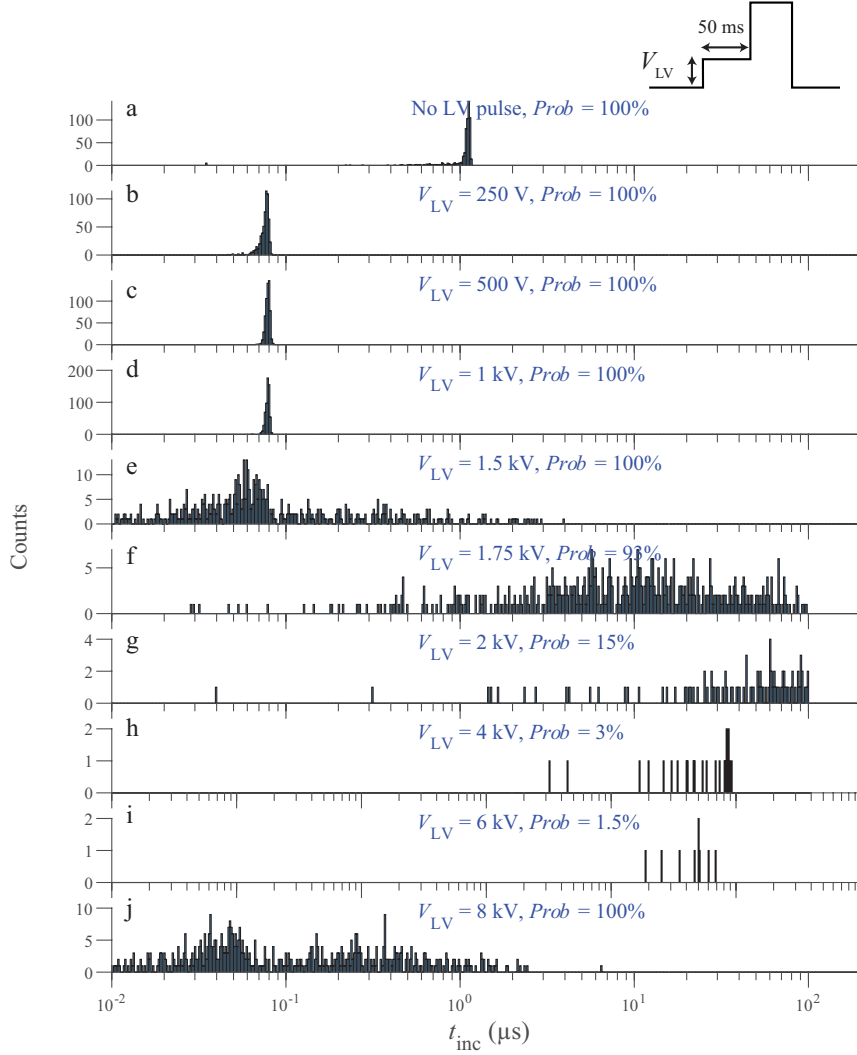


Figure 3.10: Histograms of discharge inception time t_{inc} for 600 discharges produced a) for no LV pulse and by applying a 50 ms LV pulse for $V_{LV} =$ b) 0.25, c) 0.5, d) 1, e) 1.5, f) 1.75, g) 2, h) 4, i) 6, j) 8 kV before a 10 kV pulse of 1 ms with a repetition frequency of 10 Hz. $Prob$ shows the probability of inception in each configuration.

For even higher V_{LV} values, starting at 8 kV, we observe fast inception again with a probability of 100%. However, at this voltage level, the inception peak already occurs during the LV pulse, because V_{LV} itself is already high enough to lead to inception. We observed the same effect for other values of t_{LV} . For V_{LV}

below 8 kV, the key parameter is S such that for a shorter LV pulse duration, a higher LV amplitude is required to achieve the same effect.

Negative LV pulse

Similar to a long positive LV pulse, we applied a negative LV pulse with a varying V_{LV} and a fixed t_{LV} of 10 ms (figure 3.11). As we already discussed (left-hand side of figure 3.4), for a lower V_{LV} we observe outward drift in which for $S = 1$ Vs, a 90 ns shift in \tilde{t}_{inc} was observed (figure 3.11.a₁-a₅). This continues until $V_{LV} = -2$ kV where a further increase of V_{LV} leads to a peak at low t_{inc} and thereby the disappearance of the original peak in the histogram. This transition from slow t_{inc} to fast t_{inc} occurs in a small range of V_{LV} , such that at $V_{LV} = -3.75$ kV \tilde{t}_{inc} is 30 ns (figure 3.11.b₁-b₆). Further increasing V_{LV} causes a negative t_{inc} (figure 3.11.b₇-b₉). Such a negative t_{inc} indicates that the discharge initiates during the rise time of the LV pulse immediately before the main HV pulse no discharge was observed during the on-time of the LV pulse.

3.4 Summary and conclusion

We measured inception delays t_{inc} of streamers in CO₂ gas to study the inception process in repetitive discharges in this gas. We applied 10 kV high voltage pulses with a fixed pulse duration of 1 ms and repetition frequency of 10 Hz. This can produce some residual charges that influence t_{inc} of the next pulse. To manipulate the residual charges we applied an LV pulse with different duration t_{LV} and amplitude V_{LV} before the main HV pulses. Application of the LV pulse leads to a shift in the t_{inc} histogram peak. Three main phenomena were observed, based on the different applied S ($V_{LV} \cdot t_{LV}$) values: drift, neutralization, and ionization during the LV pulse.

At low S values, discharges incept faster or slower for positive and negative LV pulses respectively. However, we observed an asymmetric shift differing three order of magnitude between positive and negative LV pulses. For a positive LV pulse with $S = 1$ mVs, we observed a 92 ns shift in \tilde{t}_{inc} , the median value of t_{inc} . To have a similar magnitude \tilde{t}_{inc} shift with a negative LV pulse, we must apply a pulse with $S = 1$ Vs. This is not consistent with our earlier observations in synthetic air. We hypothesize that this is caused by the fundamental differences between the detachment mechanism in CO₂ and air. O₂⁻ ions need to drift to a high electric field region to detach an electron. However, in the case of CO₂ due to the high yield of associative-detachment in low electric fields, O⁻ ions can release electrons through reaction with CO. In this case, an LV pulse with a low

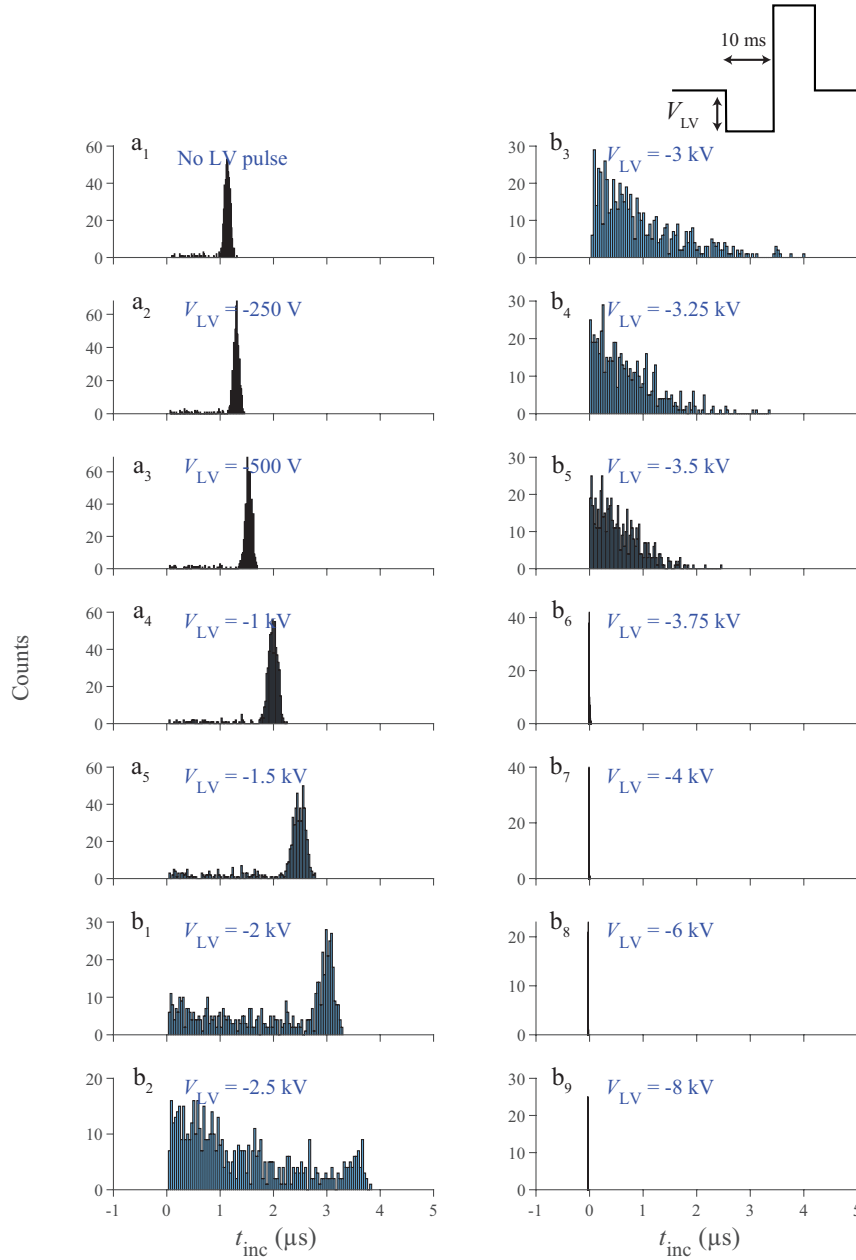


Figure 3.11: Histograms of discharge inception time t_{inc} for 600 discharges produced a₁) for no LV pulse and by applying a negative 10 ms pulse for $V_{LV} =$ a₂) -0.25, a₃) -0.5, a₄) -1, a₅) -2, (drift) b₁) -2, b₂) -2.5, b₃) -3, b₄) -3.25, b₅) -3.5, b₆) -3.75, b₇) -4, b₈) -6, b₉) -8 kV (neutralization and ionization in LV pulse) before a 10 kV pulse of 1 ms with a repetition frequency of 10 Hz.

S value drifts electrons significantly and ions hardly while an LV pulse high S value can also drift ions on top of the electrons.

We observed that the corresponding shift in \tilde{t}_{inc} due to application of LV pulse follows the mobility data and scales consistently with S value. This indicates that we can neglect the effect of space charge and its effect on electric fields for low S

values. However we observed different phenomena for higher values of S .

Applying a positive LV pulse for a longer time increases t_{inc} but decreases the probability of inception. This is likely due to neutralization of electrons and ions at the electrode. At $V_{\text{LV}} = 8 \text{ kV}$, the LV pulse is high enough to ionize the gas and we observed streamers already during the LV pulse. This is different for a negative LV pulse where ions drift away from their initial position. For a negative LV pulse with $V_{\text{LV}} \geq 2 \text{ kV}$, we observe formation of a fast peak ($\tilde{t}_{\text{inc}} = 120 \text{ ns}$) in the t_{inc} histogram replacing the original ion-associated peak. Increasing the voltage above 6 kV caused discharge inception during the LV pulse rising flank.

In our calculations, electrons should drift about 25 mm to reach the ionization zone. This seems to be a long distance since electrons can attach through several pathways such as dissociative attachment to CO_2 and O_2 , and three body attachment to O_2 producing O^- and O_2^- [104]. Our simple analysis on four reactions showed that attachment time is slightly longer than inception times.

4

Lightning inception by hydrometeors: a numerical approach

Abstract

Lightning is observed to incept in thundercloud electric fields below the threshold value E_k for discharge initiation. To explain this, the local enhancement of the electric field by hydrometeors is considered. The conditions for the onset of positive corona discharges are studied in air for ellipsoidal geometries. A hydrometeor is simulated as an individual charged conductor in zero ambient field; there is only a field generated by the charge on the hydrometeor surface. By doing so, the feasibility of corona inception from ellipsoidal hydrometeors can be formulated based on the self-sustaining condition of electron avalanches. For representative hydrometeor volumes and typical thundercloud pressure, values between $1.2 E_k$ and $37 E_k$ were found for the onset electric field at the tip of the ellipsoid. From simulations the required ambient electric field for corona onset from an uncharged hydrometeor can then be derived. This results in values between $0.07 E_k$ and $0.8 E_k$ for semi-axes aspect ratios between 0.01 and 1. The charge required on the hydrometeor surface for corona onset is minimum for semi-axes aspect ratios between 0.04 and 0.07 depending on the considered hydrometeor volume. For the simulated hydrometeors, the values of this onset charge for typical pressures are between 1500 pC and 3200 pC. Including a size-correction for comparison to in situ measurement shows agreement with measured precipitation charges. From the results it is concluded that corona onset from ellipsoidal hydrometeors of a realistic volume can be achieved in thundercloud conditions for certain aspect ratios.

This chapter is based on [S. Peeters, S. Mirpour, C. Kohn, and S. Nijdam. "A Model for Positive Corona Inception from Charged Ellipsoidal Thundercloud Hydrometeors." submitted to Journal of Geophysical Research: Atmospheres]

4.1 Introduction

One of the greatest unanswered questions in lightning physics is how lightning is initiated in a thunderstorm [3], [28], [105]. From in situ measurements it is found that lightning initiates in thundercloud electric fields which are considerably lower than the breakdown electric field required for the inception of electric discharges [106], [107]. One of the most popular and widely corroborated theories explaining how this is possible is the hydrometeor theory [28], [105]. This theory states that hydrometeors - ice and water particles in thunderclouds - locally enhance the electric field, such that the breakdown field is exceeded, and lightning inception is enabled. In recent observations of narrow bipolar events in thunderstorms, which generally coincide with lightning initiation, clear evidence supporting the involvement of hydrometeors was obtained [37]. The role of hydrometeors in lightning inception has been investigated in laboratory experiments [40], [108], [109] with a main focus on corona onset, which is the initial stage of the formation of a lightning leader.

A corona discharge is the result of electrical breakdown, which occurs at the voltage where the insulating gas surrounding the electrode becomes electrically conductive. An electrical discharge is thus only possible when a critical voltage, the onset voltage V_0 , on the electrode is reached. Equivalently, the electric field E in the discharge region should exceed the breakdown threshold field E_k and thus the field on the surface of the electrode should exceed the onset field E_0 . The breakdown field scales linearly with pressure, and at a typical thundercloud altitude pressure of 0.4 atm this field has a value of about 10 kV/cm [110]. The main mechanism of electrical breakdown is the electron avalanche. For electric fields above E_k , electrons can multiply by means of impact ionization of air molecules, thereby forming avalanches. In order to have a self-sustaining discharge, a constant source of seed electrons is required, which can be supplied by photo-ionization [110]. The first group of electrons that collides with the gas molecules and leads to photoionization is known as the primary electron avalanche, and the subsequently formed second group of electrons that can give further photoionization is known as the secondary electron avalanche (see Figure 4.1). In air, the gas molecules that are dominant in emitting photons after collisions with free electrons are nitrogen molecules, and the gas molecules that are predominantly photoionized by these photons are oxygen molecules. It should be noted that avalanche formation is a stochastic process, such that electron multiplication can also take place in fields (slightly) below the breakdown field. These contributions are briefly investigated but otherwise neglected in this work.

The onset of a corona discharge is typically defined by the discharge becoming self-sustaining. The self-sustaining criterion that is often applied is the amount of photons produced by the secondary avalanche being at least equal to those produced by the primary avalanche [111], [112]. This condition is also adapted by the current work, which closely follows the structure of the work by Liu, Dwyer, and Rassoul [111].

Depending on electrode polarity, corona discharges can be positive or negative. A popular hypothesis for lightning initiation is that the development of a positive streamer system, developed from a seed positive streamer from the corona on a hydrometeor, precedes and leads to negative breakdown [4], [28], [32], [113], [114]. Therefore, positive corona discharges are of great interest when investigating the initial stage of lightning initiation.

Laboratory experiments have revealed that the onset of a corona discharge strongly depends on the size and shape of the hydrometeor. In their study on corona initiation from small ice crystals, Petersen, Bailey, Hallett, et al. [40] reported that the onset field E_0 decreases with hydrometeor length and that ice crystals with sharper tips promote glow coronae while inhibiting positive streamer formation. Moreover, they noted that the onset field increases linearly with the relative gas density $\delta = N/N_0$ (where N and N_0 are the actual and standard gas densities), meaning $E_0 \sim p/T$, with p the pressure and T the temperature. The decrease of the onset field with size is also found in many point-to-plane and rod-to-plane experiments using metal electrodes [115]–[119], which are observed to give corona onset voltages very similar to ice electrodes [120].

In simulations, similar conclusions were reached. Dubinova, Rutjes, Ebert, et al. [59] investigated discharge inception conditions for dielectric ellipsoidal hydrometeors and concluded that an increase in hydrometeor length yields stronger field enhancement, as does a decrease in hydrometeor tip radius. Hence, a longer, sharper hydrometeor generally requires a lower background electric field for the initiation of a discharge. Likewise, in simulations of streamer initiation from charged water drops Babich, Bochkov, Kutsyk, et al. [4] found a lower threshold ambient field for larger drop sizes. Dubinova, Rutjes, Ebert, et al. [59] also observed an optimal semi-axes aspect ratio for inception; though longer hydrometeors produce a higher electric field, the probability of discharge initiation decreases when they become too sharp, because the field enhancement becomes too localized at the tip. As this ratio fixes the ellipsoidal hydrometeor's shape, an optimal shape can be determined. Simulations [121] also show the experimentally observed linear pressure dependence of discharge initiation. This is expected, as it follows from the pressure dependence of the

breakdown field.

In addition to size, shape and air density, the onset of a corona discharge has been found to depend on the orientation, surface features and initial charge of the hydrometeor. Griffiths and Latham [109] concluded from experimental studies on ice particles that onset fields in thundercloud regions are probably in the range of 400-500 kV/cm, which was later corrected by Griffiths [122] to 350-450 kV/cm when taking into account the effect of charge on ice particles. Furthermore, Griffiths and Latham [109] suggested that continuous corona discharges could be generated from thundercloud ice crystals at temperatures above -18°C only. Of course, the gas density increases with decreasing temperature, explaining the subsequent increase of the onset field. Moreover, the surface conductivity decreases with decreasing temperature such that corona onset becomes less likely [36], [109], and generally smaller ice crystals are formed at lower temperatures [36]. In 2006, Petersen, Bailey, Hallett, et al. [36] demonstrated that corona discharges can initiate in temperatures down to -38°C , showing that corona and streamer discharges can initiate from hydrometeors at thundercloud altitudes relevant for lightning initiation. Moreover, from numerical simulations Babich, Bochkov, and Neubert [123] observed that the required charge on hydrometeors at these representative temperatures and altitudes agrees with measured thundercloud precipitation charges, which are generally between 10 and 200 pC and for a small fraction of hydrometeors between 200 and 400 pC [124].

To conclude, these studies reveal that the onset of a corona discharge from a hydrometeor depends on its size, shape and surface charge, and on environmental conditions such as pressure, temperature and the ambient electric field. Experimental results and in situ measurements indicate the essential role of hydrometeors in lightning initiation. These findings are supported by simulations of lightning inception from ice and water particles.

The comparison of experimental work on corona onset from ice point electrodes to measurements on metal point electrodes has shown the corona onset voltage to be very comparable [120]. To simulate the onset of a positive corona discharge from a metal electrode in air, Naidis [112] introduced a model giving a corona inception criterion taking into account the ambient pressure and the size and shape of the electrode. This model was applied to spherical and cylindrical electrodes, and later revisited by Liu, Dwyer, and Rassoul [111] for the spherical case.

The main goal of this chapter is to extend this model to include another representative shape, the prolate spheroid, as ice and water particles in a thundercloud can have a wide variety of shapes depending on thundercloud conditions. Their sizes

range from a few micrometers to several centimeters [125]. The size distribution of hydrometeors is little investigated within thunderclouds due to difficulties of in situ measurements [105], but it is expected that the extreme cases of several centimeters are rare, and that a millimeter range is more representative [126], [127]. When these hydrometeors fall downwards due to gravity, they are extended along the vertical direction. The shape of the hydrometeor in the direction perpendicular to the thundercloud electric field has a negligible contribution to the field enhancement. More precisely, the enhancement at the tips is mainly determined by the length of the hydrometeor and the radius of curvature of the tip of the hydrometeor [59], [128]. Taking this into account, it can prove fruitful to investigate ellipsoidal hydrometeors. More specifically, assuming cylindrically symmetric thundercloud conditions, a prolate ellipsoid of revolution, or prolate spheroid, is considered.

Thus, the purpose of this study is to simulate positive corona discharges originating from a positively charged spheroidal hydrometeor tip. In doing so, the feasibility of lightning initiation from a spheroidal hydrometeor is studied. The simulation of this configuration is done using the model for the onset of positive corona discharges introduced by Naidis [112] and further elaborated by Liu, Dwyer, and Rassoul [111]. The investigated hydrometeor is isolated and without ambient electric field. Thus, there is only an electric field generated by the charge on the hydrometeor, which differs from realistic lightning occurrences, where there is also an external field present due to the large-scale charge distribution. However, the effects of the field induced by a charged particle can already reveal a lot about the role of particle shape and size in discharge inception. Hence, for the charged hydrometeor the dependence of corona onset on its semi-axes aspect ratio and volume is reported for various ambient pressures by varying its major and minor axes.

4.2 Model Description

As elaborated, a corona discharge is the result of electrical breakdown via direct impact ionization within avalanches. The resulting avalanches are seeded by electrons supplied through photoionization. Taking loss by attachment processes into account, $\alpha = \eta$ defines electrical breakdown, where α is the number of ionizing collisions per unit length and η the number of electron attachments per unit length. Formulating the net ionization coefficient $\alpha_{eff} = \alpha - \eta$, breakdown is defined by $\alpha_{eff} = 0$. Of course these coefficients depend on the electric field E , meaning $\alpha_{eff} = 0$ determines the breakdown field E_k .

The number of photons produced by a primary avalanche is denoted by N_1 , and those

produced by a secondary avalanche by N_2 . N_2 depends on N_1 through $N_2 = \gamma N_1$, where γ is the mean number of photons from the secondary avalanche produced by one of the photons from the primary avalanche (see Figure 4.1). In short, γ is the multiplication factor. Naidis [112] formulates the criterion for corona inception as the secondary avalanche producing at least as many photons as the primary avalanche, so $N_2 = N_1$, or equivalently $\gamma = 1$. Then, the discharge is self-sustaining; it can proceed without external ionization sources. This criterion does not take into account the stochastic nature of discharge inception. The region around the hydrometeor where the breakdown field is exceeded is sufficiently small such that individual electron avalanches, which have an intrinsically random nature, should be considered. Here, the randomness, and therefore contributions from outside this region, is neglected, as only the total amount of electrons in the avalanche is investigated. The inclusion of stochastic effects would soften the criterion, as then electrons can 'tunnel' to higher energies [44].

For point and wire electrodes, most of the electrons and photons are produced near the surface of the electrodes. It is therefore a reasonable assumption that all photons that lead to photoionization are produced at the electrode surface. This assumption overestimates the effect of photoionization, as the effect of photons on electron production is now maximized. As will be further substantiated, this chapter studies the minimum conditions for the onset of a corona discharge, such that this assumption is acceptable. Besides inducing photoionization and thereby triggering secondary electron avalanches, a photon can also fall back to the electrode surface or leave the ionization region and consequently not contribute to the secondary avalanche. Different factors, such as the photon absorption probability, affect this balance and thus play a role in satisfying the $\gamma = 1$ criterion for positive corona onset.

To formulate the $\gamma = 1$ criterion, a spherical coordinate system (r, θ, ϕ) is introduced with its origin at the surface of the electrode. This is illustrated in Figure 4.2 for the ellipsoidal electrode, with major axis a and minor axis b , considered in this paper. In the region near the electrode tip the electric field E reaches its maximum. Consequently, the number of electrons in the primary avalanche and the probability of photon emission are also maximum near the tip. For simplicity, it is assumed that the primary photon is emitted at the origin of the spherical coordinate system. Taking into account all possible directions in which this photon can move, the photon absorption region can be defined as the part of the ionization region ($E \geq E_k$) where $\theta \leq \pi/2$. In other words, the photon absorption region is the region that can be reached by the photon and where the field is sufficiently

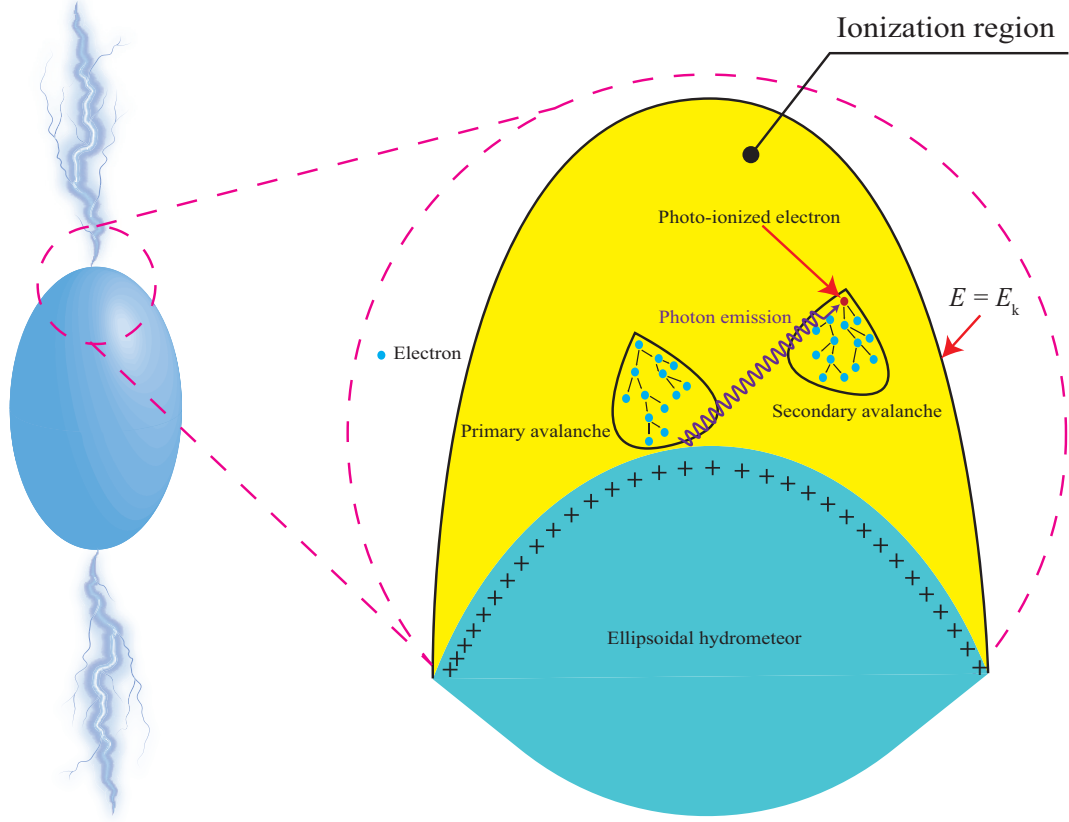


Figure 4.1: An illustrative image (not to scale) of the inception process in which the primary avalanche releases energetic photons, leading to the production of a photo-ionized electron. The secondary avalanche is formed by the multiplication of the photo-ionized electron via direct impact ionization. Inception occurs when the number of electrons in the secondary avalanche and the primary avalanche are equal. All processes occur in the photon absorption area, where the electric field is higher than the breakdown field (E_k).

high such that an electron avalanche can be created. This region, highlighted in deep yellow in Figure 4.2, is thus the region of interest for the initiation of a corona discharge.

The corona inception criterion $\gamma = 1$, derived by Naidis [112] using the above self-sustaining criterion, is then formulated as

$$\gamma \approx \xi \beta(\rho_0) \int_0^{2\pi} d\phi \int_0^{\pi/2} \sin \theta d\theta \int_0^{r_{max}(E)} r^2 P(r) \cdot \left[\exp \left(\int_{\rho_0(\theta, \phi)}^{\rho_{ab}(r, \theta, \phi)} \alpha_{eff}(\rho, E) d\rho \right) - 1 \right] dr = 1. \quad (4.1)$$

The coordinates ρ, r and θ are defined in Figure 4.2. Because of the cylindrical

symmetry of the prolate spheroid, there is no ϕ -dependence. Besides the spherical coordinate system (r, θ, ϕ) with the origin at the tip of the ellipsoid, the coordinate ρ , which is given by the direction of the electric field and starts from the z -axis, is introduced as well, as is the radial coordinate ρ' from the center of the ellipsoid. The term ξ is the ionization probability of an oxygen molecule at photon absorption. The distance $\rho_{ab}(r, \theta, \phi)$ is the distance between the point of photoionization (equivalent to the position of photon absorption) and the symmetry axis of the ellipsoid along the direction of the electric field in the point of photoionization. It is thus the length of the line along the ρ coordinate that ends at the point of photon absorption (see Figure 4.2). Similarly, the distance from the symmetry axis of the ellipsoid to its surface along the surface electric field direction is given by ρ_0 (for a sphere this would be its radius). The position where the electric field has decreased to the breakdown field E_k is given by r_{max} in the spherical coordinate system (r, θ, ϕ) . Naidis [112] uses the expression for the photon absorption probability $P(r)$ in air where photoionization of oxygen molecules takes place at absorption of radiation of wavelengths 98 - 102.5 nm, emitted by nitrogen molecules [129]

$$P(r) = \frac{\exp(-\kappa_1 r \delta) - \exp(-\kappa_2 r \delta)}{4\pi r^3 \log(\kappa_2/\kappa_1)}, \quad (4.2)$$

where $\kappa_1 = 5.6 \text{ cm}^{-1}$ and $\kappa_2 = 320 \text{ cm}^{-1}$. The term $\xi\beta(\rho_0)$ can be found from

$$\xi\beta = \left(0.03 + \frac{3.78}{E}\right) \frac{\delta_q}{\delta + \delta_q}, \quad (4.3)$$

where $\delta_q = 0.04$ and E is the electric field [129]. Here β is the coefficient of production of ionizing photons scaled to the net ionization coefficient α_{eff} . Because of its weak dependence on the electric field and the high fields at the electrode surface, β is approximated by its value $\beta(\rho_0)$ at the surface. To apply the corona inception criterion $\gamma = 1$ to a prolate spheroid, analytical expressions should be derived for the distances r_{max} , ρ_0 and ρ_{ab} , and the electric field E , on which the ionization probability and the net ionization coefficient depend.

To determine ρ_{ab} , the direction of the electric field is needed. This direction is given by the bisector of the two straight lines from the focal points of the prolate spheroid to the observation point [130]. Using various trigonometric relations, which are given in the Appendices B, it can be derived that

$$\rho_{ab} = \frac{\sqrt{2}\rho_1^2 \sqrt{\frac{(4\sqrt{a^2-b^2}(a+r\cos(\theta))+\rho_1^2)(2ar\cos(\theta)+b^2+\rho_1\rho_2+r^2)}{\rho_1\rho_2}}}{\rho_1^2 + \rho_1\rho_2}, \quad (4.4)$$

$$E(x, y, z) = \frac{Q}{4\pi\epsilon_0} \left(\prod_{k=1}^3 \frac{1}{\sqrt{a_k^2 + \Theta(\vec{r})}} \right) / \sqrt{\left(\sum_{m=1}^3 \frac{x_m^2}{(a_m^2 + \Theta(\vec{r}))^2} \right)}, \quad (4.6)$$

where Q is the total charge on the ellipsoid surface, ϵ_0 is the vacuum permittivity, $\Theta(\vec{r})$ the equipotential surfaces and $a_1 = a_x = b$, $a_2 = a_y = b$ and $a_3 = a_z = a$ are the semi-axes of the considered spheroid of Figure 4.2. Moreover, the Θ -equipotentials follow from

$$\sum_{k=1}^3 \frac{x_k^2}{a_k^2 + \Theta(\vec{r})} = 1, \text{ for } \Theta(\vec{r}) > 0. \quad (4.7)$$

The above electric field expression can be rewritten in the considered coordinates (ρ', r, θ, ϕ) as defined in Figure 4.2. Here r can be converted to ρ' using the trigonometric relation $\rho' = \sqrt{a^2 + r^2 + 2ar \cos(\theta)}$. The field is also reformulated to contain the electric field at the ellipsoid tip ($z = a$ in equation (4.6)) $E_0 = \frac{Q}{4\pi b^2 \epsilon_0}$. To obtain the final expression for the electric field, the ρ' coordinate is converted to the ρ coordinate along the electric field direction as required for the $\gamma = 1$ criterion. This is done using the derived ρ_{ab} expression. In order to have analytically solvable equations in this derivation, r is not converted to ρ' in the conversion from ρ' to ρ . This means some ambiguity remains in the expression of the electric field $E = E(\rho, r, \theta)$. As eventually the equation $\gamma = 1$ is solved numerically, this ambiguity is not a problem as long as the resulting α_{eff} (which is calculated using the electric field) behaves correctly. The used formulation is

$$E(\rho, r, \theta) = \frac{2b^2 E_0 \rho'}{\sqrt{a^2 - b^2 + q + \rho'^2} \left(-a^2 + b^2 + q + \rho'^2 \right) \sqrt{\frac{q}{(b^2 - a^2)(a^2 + 2ar \cos(\theta) + r^2 \cos(2\theta)) + q + \rho'^2}}}, \quad (4.8)$$

with the shorthand $q = \sqrt{\frac{2\rho'^2(b^2 - a^2)(a^2 + 2ar \cos(\theta) + r^2 \cos(2\theta))}{a^2 + 2ar \cos(\theta) + r^2}} + (a^2 - b^2)^2 + \rho'^4$ and with

$$\rho' = \sqrt{\frac{2ar \cos(\theta) (3a^2 - 3b^2 + \rho^2) + 2a^2 \rho^2 + a^2 \rho_1 \rho_2 - b^2 \rho^2 - b^2 \rho_1 \rho_2 + \rho^2 r^2 + \rho^2 \rho_1 \rho_2 + p}{2a^2 + 2ar \cos(\theta) - b^2 + r^2 + \rho_1 \rho_2}}, \quad (4.9)$$

with $p = 2a^4 - a^2 b^2 + 2a^2 r^2 \cos(2\theta) + a^2 r^2 - b^4 - 2b^2 r^2 \cos(2\theta) - b^2 r^2$. The derivations of these expressions are presented in Appendix B.3.

Finally, the distance r_{max} from the tip of the prolate spheroid to the position where $E = E_k$ can be determined. Because there is no explicit solution for r_{max}

in the considered geometry, this is done by approximating the surface $E = E_k$ as forming an ellipsoid surface near the tip, as is validated in simulations in Appendix B.4. Then, finding r_{max} specifically for $\theta = 0$ and $\theta = \pi/2$ is sufficient to obtain r_{max} for arbitrary θ . These expressions are found by reformulating the electric field in terms of r and θ only and solving $E(r, \theta = 0) = E_k$ and $E(r, \theta = \pi/2) = E_k$. This yields an analytical expression for r_{max} which can be validated using the aforementioned simulations:

$$r_{max}(\theta) = \frac{r_{max}(\theta=\pi/2) \left(\sqrt{r_{max}(\theta=0)^2 (2a+r_{max}(\theta=0))^2 \sin^2(\theta) + r_{max}(\theta=\pi/2)^2 (a+r_{max}(\theta=0))^2 \cos^2(\theta)} - a r_{max}(\theta=\pi/2) \cos(\theta) \right)}{r_{max}(\theta=0) (2a+r_{max}(\theta=0)) \sin^2(\theta) + r_{max}(\theta=\pi/2)^2 \cos^2(\theta)}, \quad (4.10)$$

with the expressions for $r_{max}(\theta = 0)$ and $r_{max}(\theta = \pi/2)$ derived and given in Appendix B.4.

Using the now known required expressions, the surface electric field E_0 at the tip of the ellipsoidal hydrometeor required for the onset of a positive corona discharge can be calculated from equation (4.1) at the known electric field distribution $E(\rho, r, \theta)$ for different values of the relative gas density δ and major and minor axes a and b . As noted by Liu, Dwyer, and Rassoul [111], it is more convenient to, instead of using $\gamma = 1$, define a new quantity:

$$Y \equiv \gamma - 1 = 0. \quad (4.11)$$

The onset surface electric field E_0 at the tip can now be computed by finding the zero of Y . This cannot be done analytically due to the complexity of the integrals. Moreover, since the integration limits in equation (4.1) also depend on the unknown E_0 and the integration variables, numerical integration by itself is also not sufficient. However, this numerical integration can be combined with a numerical function that finds the root of an expression, such as the MATLAB function 'fzero', as used by Liu, Dwyer, and Rassoul [111] and this work, or the Mathematica function 'FindRoot'. Substituting the numerical integration of equation (4.11) into the find root function means the numerical integration can be solved even though the integration limits are not numbers. Thus, in combination with this method the model determines the corona onset field E_0 at the hydrometeor tip through equation (4.11), equivalent to equation (4.1).

After applying the find root function, the found onset field E_0 can be used to evaluate the ionization integral K , given by

$$K = \int_{\rho_0}^{\rho_c} \alpha_{eff}(\rho, E) d\rho, \quad (4.12)$$

where $\rho_c = \rho_{ab}(r_{max}, \theta, \phi)$ gives the position of the breakdown field E_k . Exponentiation of K yields the number of electrons produced by an avalanche from the edge of the ionization region to the surface of the hydrometeor. Equation (4.12) is thus a criterion for the onset of a positive corona discharge with K a threshold value that needs to be reached to enable initiation. It is important to note that the above integration is taken along the field line from the surface of the electrode to the edge of the ionization region, because the avalanche follows the direction of the electric field.

Per the convention used by Naidis [112], the model is set up to output the onset field E_0 , from which the onset voltage V_0 , onset charge Q , and ionization integral K can be derived. This order is thus kept in the following results section.

As stated, the used model gives the minimum condition for the onset of a corona discharge. Besides assuming all photons are emitted at the surface, it neglects the presence of space charge created in the discharge. Furthermore, the onset criterion is only imposed on the secondary avalanche; further avalanches are assumed to take place when this criterion is satisfied. While these factors generally increase the threshold for corona inception, including its stochastic nature would lower this threshold. The validity of the model depends on the relevant dimensions. For the model to be reliable, the largest photon absorption length (r_{max}) should be smaller than the length of the ellipsoid. Otherwise, the equilibrium between the ionization coefficients with the local electric field cannot be guaranteed.

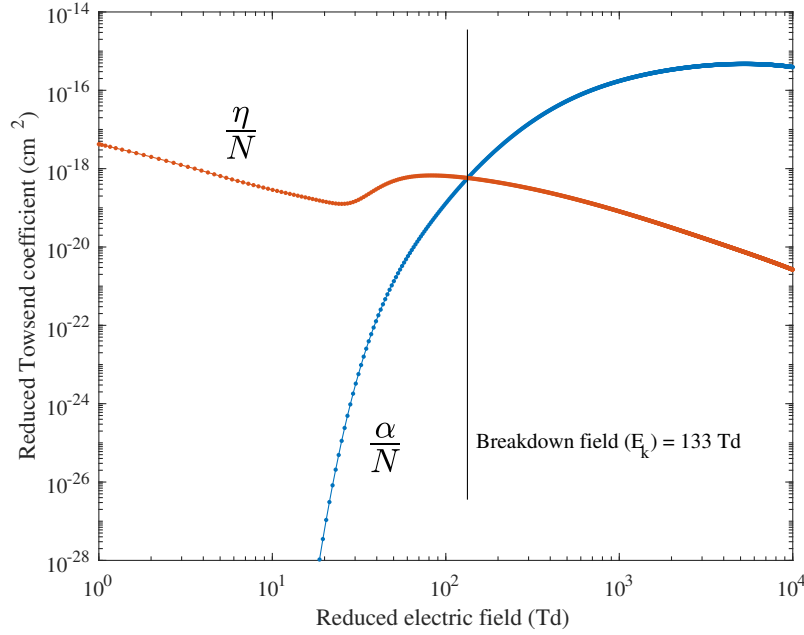
4.3 Results and discussions

4.3.1 The effects of varying aspect ratio and volume of spheroidal hydrometeors on the corona inception criterion

To calculate the required effective ionization coefficient α_{eff} in equation (4.1), we need to use the air plasma-chemical reactions which are listed in Table 4.1. All electron impact ionization, excitation, elastic and attachment reactions (except three-body attachment) that are included in the list were taken from Itikawa database [72]–[74]. The three-body attachment with O_2 as the third body was taken from Phelps database [75] and scaled to the different δ . Next, the reactions were used as input for BOLSIG+ [82], [83] to calculate the ionization and attachment coefficients. The results are depicted in Figure 4.3 and the effective ionization coefficient is defined as the subtraction of the attachment coefficient from the ionization coefficient.

Table 4.1: List of plasma-chemical reactions used for calculation the ionization and attachment coefficients.

Elastic	$e^- + N_2 \rightarrow e^- + N_2$ $e^- + O_2 \rightarrow e^- + O_2$
Ionization	$e^- + N_2 \rightarrow 2e^- + N_2^+$ $e^- + N_2 \rightarrow 2e^- + N^+ + N$ $e^- + N_2 \rightarrow 3e^- + N^{2+} + N$ $e^- + O_2 \rightarrow 2e^- + O_2^+$ $e^- + O_2 \rightarrow 2e^- + O^+ + O$ $e^- + O_2 \rightarrow 3e^- + O^{2+} + O$
Attachment	$e^- + O_2 + O_2 \rightarrow O_2^- + O_2$ $e^- + O_2 \rightarrow O^- + O$
Excitation	$e^- + O_2 \rightarrow e^- + O_2^*$ $e^- + N_2 \rightarrow e^- + N_2^*$

**Figure 4.3:** Reduced attachment (η/N) and ionization (α/N) coefficients as a function of reduced electric field in an $N_2 : O_2 = 80:20$ mixture at $\delta=1$. The breakdown field is determined where $\alpha - \eta=0$.

Using the corona inception criterion of equation (4.1), equation (4.11) is solved numerically in MATLAB for varying hydrometeor volume $\frac{4}{3}\pi C$, with $C = ab^2$ the volume parameter, and varying aspect ratios b/a . The aspect ratio b/a is considered instead of, for example, the major axis a , such that the effects of varying volume and shape can be investigated separately.

The studied hydrometeor geometries have volume parameters of $C = 0.01, 0.05,$ and 0.1 cm^3 and aspect ratios from $b/a = 0.01$ to 1, where $b/a = 1$ represents

a sphere ($a = b$). First, positive corona inception is investigated at atmospheric pressure ($\delta = 1$). The onset field E_0 at the tip of the ellipsoid, found directly from solving equation (4.11), is presented in Figure 4.4a. It can be seen that E_0 decreases with volume for a fixed aspect ratio. For the smallest hydrometeor, $C = 0.01 \text{ cm}^3$, the onset field at $b/a = 0.045$ is 366 kV/cm, while for the largest hydrometeor, $C = 0.1 \text{ cm}^3$, this is 248 kV/cm. The decrease of the onset field with increasing volume is expected as a larger hydrometeor, simulated as an electrode, provides more surface for photon emission to the photon absorption region. Here, it should be noted that in the model it was assumed that all photons that lead to photoionization are emitted at the surface. Thus, for a smaller hydrometeor less photons are emitted and therefore less electrons are produced by photoionization, such that to satisfy the corona onset criterion a larger onset field E_0 is required.

From Figure 4.4a it can also be concluded that for a fixed volume, a sharper ellipsoid has a larger onset field E_0 at its tip. Because a sharper ellipsoid has less surface near the photon absorption region, a larger E_0 is needed to meet the inception criterion. In the spherical limit, $b/a = 1$, the onset field for $C = 0.01 \text{ cm}^3$ is about 17% larger than that for $C = 0.1 \text{ cm}^3$, and for the much sharper tip at $b/a \approx 0.015$ this difference has increased to about 70%. The onset field thus increases much stronger with sharpness for a smaller hydrometeor, which is expected as a smaller object has more surface area compared to its volume. It should be noted, however, that Figure 4.4a does not give the whole story. This onset field is only at the tip of the ellipsoid. Moreover, as charges on a conductor tend to move away from each other as much as possible on its surface, the electric field is enhanced more strongly near a sharper tip. Hence, even though a sharper ellipsoid has a larger E_0 , this does not necessarily mean corona inception from sharper hydrometeors in thunderstorms is less likely. On the contrary, Petersen, Bailey, Hallett, et al. [40] observed sharper hydrometeors promote glow coronae. Griffiths and Latham [109] suggested in their paper on coronae from ice hydrometeors that the onset ambient field decreases with increasing combined length of the liquid filament, which was confirmed by Crabb and Latham [33], who also found that the elongated filament resulting from raindrop collision promotes corona onset. This seems to contradict the decrease of E_0 with elongation in Figure 4.4a, but taking into account the mentioned effect of only considering the tip this discrepancy is explained. To draw clearer conclusions, other quantities such as potential, surface charge and the ionization integral should be considered as well when studying corona inception from an ellipsoid.

From the onset field E_0 the onset voltage, or inception voltage, along the major axis (from the tip to infinity) can be calculated by the integration of the electric

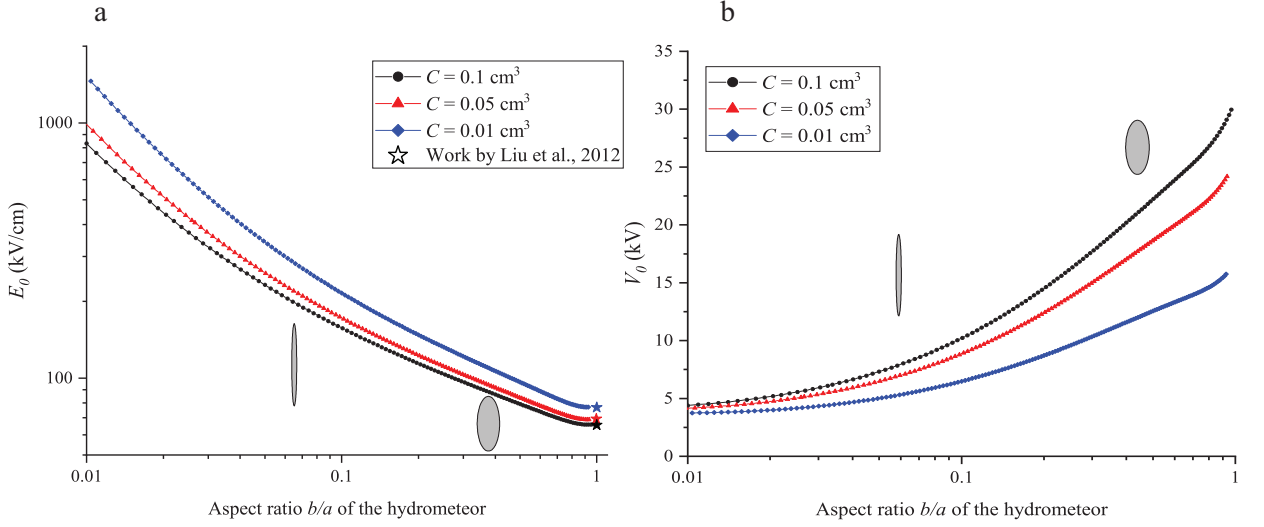


Figure 4.4: The a) onset field, and b) onset voltage for positive coronae at the tip of the ellipsoidal hydrometeor for $C = 0.01, 0.05,$ and 0.1 cm^3 for varying aspect ratio b/a at atmospheric pressure. For clarity, two ellipsoid shapes are given at different b/a . Results are compared in the spherical limit ($b = a$) with Liu, Dwyer, and Rassoul [111].

field. This onset voltage V_0 is shown in Figure 4.4b. The inception voltage increases with hydrometeor volume. This is also found by Liu, Dwyer, and Rassoul [111] for a spherical electrode. Note that the onset field decreases with volume while the onset voltage increases, which can be quickly understood by looking at the simpler configuration of a sphere, where $V_0 = E_0 \rho_0$, with ρ_0 its radius. Figure 4.4b also shows that the onset voltage is lower for a sharper ellipsoid. For a very sharp tip this difference is less noticeable, and the onset voltage is about 4 kV for the three hydrometeors. In the spherical limit, the largest hydrometeor ($C = 0.1 \text{ cm}^3$) requires 30 kV for corona onset, while the smallest hydrometeor ($C = 0.01 \text{ cm}^3$) requires 16 kV.

Besides the onset voltage V_0 , the onset charge Q can also be derived from the onset field E_0 through $E_0 = \frac{Q}{4\pi b^2 \epsilon_0}$. Of course, the onset field is a result of the onset charge, making this the more fundamental parameter. The onset charge, which is the total charge on the electrode surface, is depicted in Figure 4.5. A size-dependent optimum aspect ratio b/a is observed at which the onset charge is lowest. While a sharper ellipsoid has a higher onset field and thus requires more charge at the tip to reach this E_0 , a larger fraction of the total charge is collected at its tip because of the optimization of charge separation. In simulations of corona inception from hydrometeors modelled as dielectrics in an external electric field, Dubinova, Rutjes, Ebert, et al. [59] also found a size-dependent aspect ratio for which the onset background field is minimum. From Figure 4.5 the range of onset

charge for hydrometeors with volumes between 0.042 cm^3 and 0.42 cm^3 is found to be 2367 pC to 15,467 pC at atmospheric pressure.

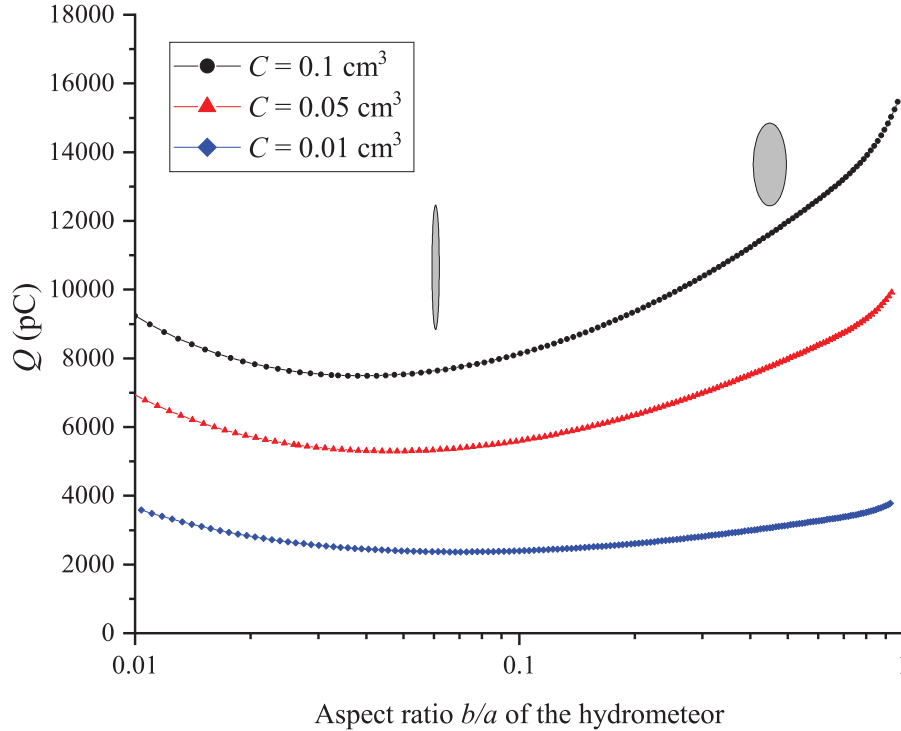


Figure 4.5: The onset charge for positive coroneae at the tip of the ellipsoidal hydrometeor for $C = 0.01, 0.05,$ and 0.1 cm^3 for varying aspect ratio b/a at atmospheric pressure.

Finally, the ionization integral K along the major axis can be calculated from the onset field as well, through equation (4.12). The result is presented in Figure 4.6. At a fixed volume, the ionization integral decreases with b/a , meaning that less electrons are required in an avalanche from the edge of the photon absorption region to the electrode surface. To interpret these results the dependence of the photon absorption area and length on the electrode dimensions are studied in COMSOL for some data points, of which the results are given in Table 4.2. From this data it can be concluded that for a fixed aspect ratio, a smaller electrode has a smaller photon absorption area and length, as does a sharper electrode for a fixed volume. However, for a very sharp electrode the photon absorption area and length are approximately equal, as can be seen for $b/a = 0.014$ in Table 4.2.

As an ellipsoid with smaller b/a has a smaller photon absorption region, photons are absorbed closer to the electrode compared to its size, such that stronger avalanches are required to satisfy the inception criterion. A similar argument was made by Naidis [112] to explain the ionization integral dependence on radius for a spherical and cylindrical electrode. Comparing the data points for different

Table 4.2: Photon absorption area and length for various ellipsoidal electrode aspect ratios and volumes.

Volume parameter C (cm ³)	Aspect ratio b/a	Semi axis a (cm)	Semi axis b (cm)	Area (mm ²)	Length r_{max} (mm)
0.1	0.014	7.93	0.11	0.21	0.12
0.1	0.045	3.68	0.16	0.33	0.22
0.1	0.141	1.70	0.24	1.02	0.47
0.1	0.447	0.79	0.35	6.20	1.02
0.05	0.014	6.29	0.08	0.25	0.11
0.05	0.045	2.92	0.13	0.28	0.20
0.05	0.141	1.35	0.19	0.84	0.41
0.05	0.447	0.62	0.28	4.91	0.88
0.01	0.014	3.68	0.05	0.25	0.09
0.01	0.045	1.70	0.07	0.28	0.16
0.01	0.141	0.79	0.11	0.58	0.31
0.01	0.447	0.36	0.16	2.71	0.61

volumes, two regions can be discerned in Figure 4.6, separated by a cross-over point around $b/a = 0.55$. At large b/a , where K drops below 14, the largest ellipsoid has the largest value for the ionization integral, again because photons are absorbed closer to the electrode with respect to its size. When K increases above 14 for decreasing b/a it is observed that the smallest ellipsoid has the largest K value. An explanation for this could be that when b/a becomes small enough, the photon absorption region becomes so small that its absolute size instead of its relative size determines the value of the ionization integral. Stronger avalanches are then required for a smaller electrode. For very small b/a the data points for different volumes appear to converge again. A likely explanation is that when the ellipsoid becomes very sharp, a photon is absorbed so close to the tip such that the total volume of the electrode has no effect; only the sharpness of the tip determines the value of the ionization integral. This is supported by the photon absorption area being approximately equal for the different volumes at $b/a = 0.014$ in Table 4.2.

4.3.2 Variation of the corona inception criterion with pressure

Next, the dependence of corona onset from an ellipsoidal hydrometeor on the ambient pressure is investigated by varying the relative gas density δ . More specifically, the values $\delta = 10$, 1, and 0.1, analogous to the works by Naidis [112] and Liu, Dwyer, and Rassoul [111], and $\delta = 0.5$, representative for thundercloud altitudes, are considered. The volume parameter is fixed at $C = 0.01$ cm³ and the aspect

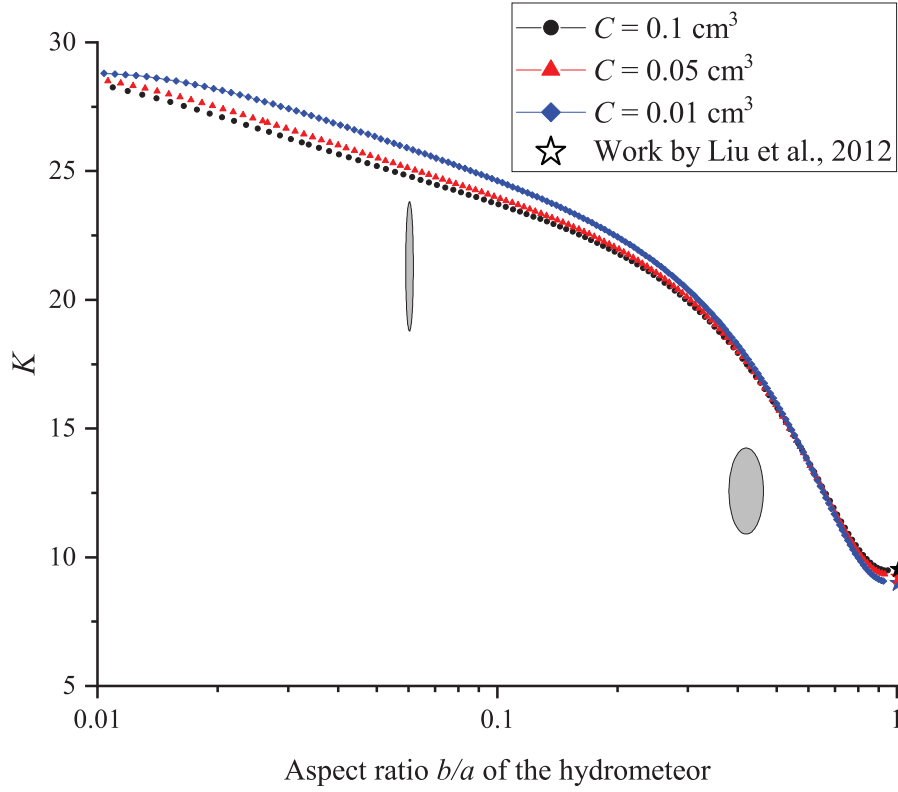


Figure 4.6: The ionization integral along the major axis for positive corona onset at the tip of the ellipsoidal hydrometeor for $C = 0.01, 0.05,$ and 0.1 cm^3 for varying aspect ratio b/a at atmospheric pressure.

ratio b/a varies again from $b/a = 0.01$ to 1. The results for the onset field at the hydrometeor tip are shown in Figure 4.7a. As expected, a higher pressure leads to a higher onset field E_0 . As explained by Liu, Dwyer, and Rassoul [111], at a higher pressure more of the excited nitrogen molecules responsible for emitting the ionizing photons are quenched, leading to a lower photon production such that a higher field is required. To briefly examine how the results are affected by the aforementioned photoionization outside of the ionization region, the computations are redone with an integration upper limit of $10r_{max}$ instead of r_{max} . It follows that the difference in outcome is generally well below 1%, only rising above 5% for $\delta = 0.5$ for the smallest volume parameter $C = 0.01 \text{ cm}^3$, and only for very blunt tips, nearing $b/a \approx 1$. Neglecting this stochastic effect thus seems justified.

Similarly, the onset charge increases with pressure, as depicted in Figure 4.7b. For $C = 0.01 \text{ cm}^3$ the onset charge is between 547 pC and 2400 pC for $\delta = 0.1$ and between 1500 pC and 3100 pC for $\delta = 0.5$. For $\delta = 0.5$ the onset charge is minimum at an aspect ratio of approximately 0.1. A pressure above atmospheric pressure, at $\delta = 10$, is not representative for thunderstorms, but is included for completeness. Again, the ionization integral K can be calculated from the onset

field and is plotted in Figure 4.7c. The pressure dependence can be explained as before; due to increased quenching of excited nitrogen molecules at higher pressures the photon production is lowered. Therefore, stronger avalanches are required to satisfy the inception criterion.

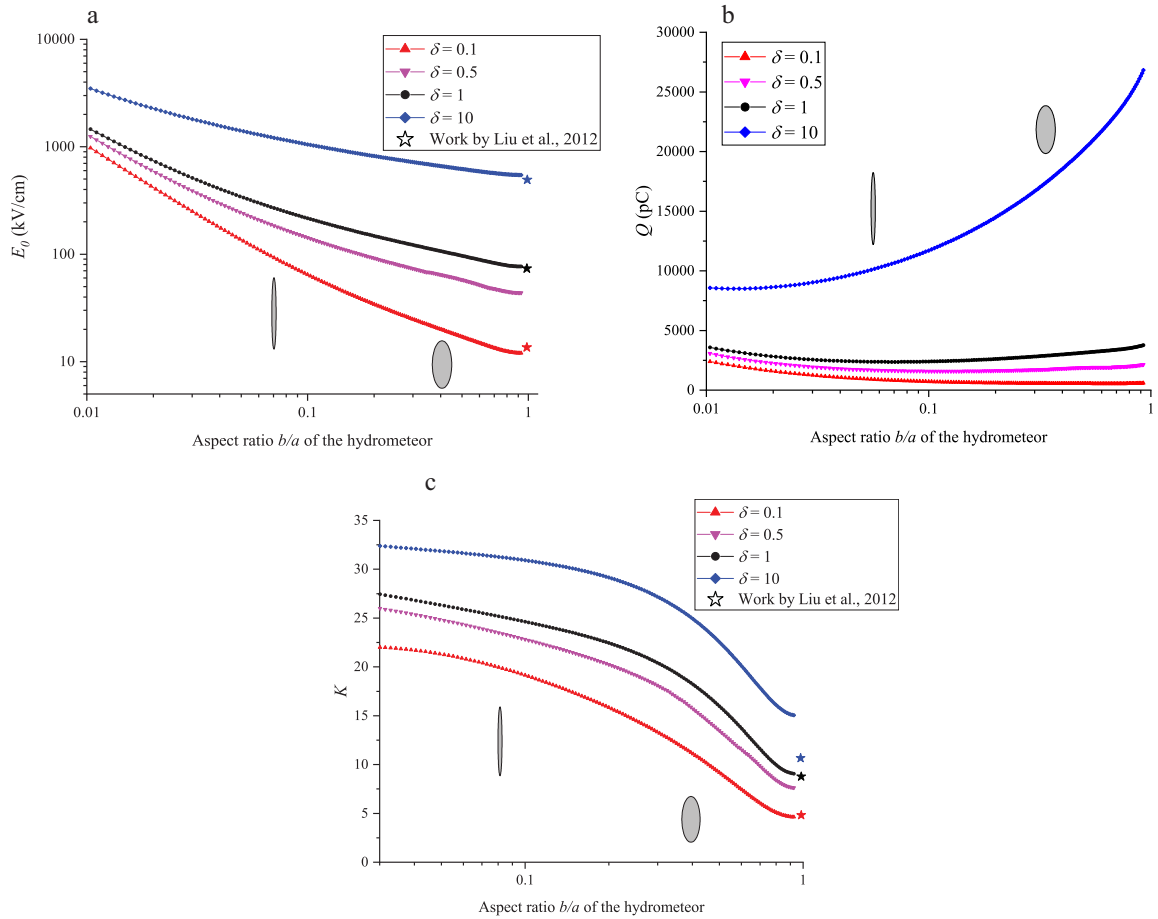


Figure 4.7: The a) onset field, b) onset charge, c) ionization integral for positive coronae at the tip of the ellipsoidal hydrometeor for $\delta = 10, 1, 0.5,$ and 0.1 for varying aspect ratio b/a at a fixed volume parameter $C = 0.01 \text{ cm}^3$. Results are compared in the spherical limit ($b = a$) with Liu, Dwyer, and Rassoul [111].

4.3.3 Dependence of the derived ambient electric field on the aspect ratio for thundercloud pressure

The ambient field E_{bg} required for corona onset can be derived from the onset field E_0 at the hydrometeor tip. This is done by simulating the hydrometeor as a conductor without surface charge in an ambient electric field in COMSOL, and increasing this field until the determined E_0 is obtained at the tip. The relative gas density of $\delta = 0.5$ and the most representative size of $C = 0.01 \text{ cm}^3$ (as

hydrometeors are generally found in the millimeter range [126], [127]) are chosen. The results are presented in Figure 4.8. It is seen that the required background field E_{bg} is below the breakdown field E_k , between $0.07 E_k$ and $0.8 E_k$, and is lowest for the sharpest hydrometeor tips.

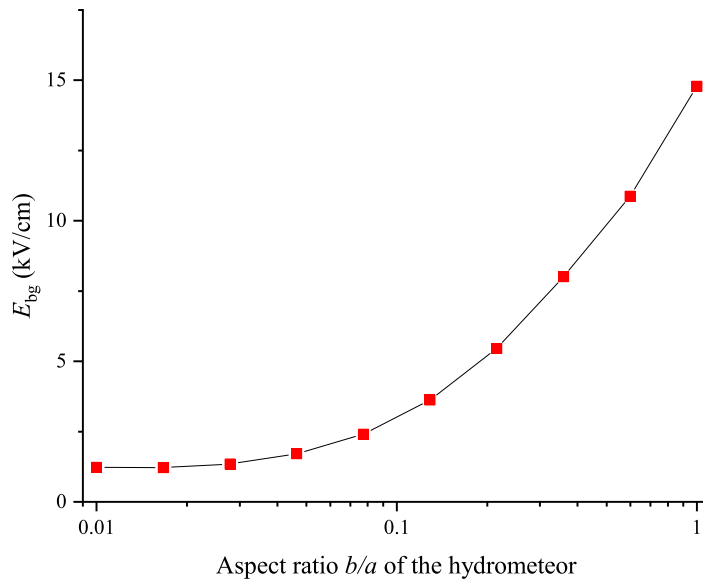


Figure 4.8: The required background electric field, E_{bg} , to have an enhanced electric field of E_0 at the tip of the hydrometeor ($C = 0.01 \text{ cm}^3$). The values are calculated at $\delta = 0.5$, where $E_k = 17.9 \text{ kV/cm}$.

4.4 Summary, Conclusions and Outlook

The corona inception criterion set up by Naidis [112] is applied through numerical simulations to spheroidal electrodes of various dimensions at different pressures. By doing so, the theoretical onset of a positive corona from an ellipsoidal hydrometeor is studied. It is found that the onset electric field at the hydrometeor tip decreases with hydrometeor volume and tip bluntness, as the hydrometeor surface near the photon absorption region increases with these factors. Moreover, the onset field increases with pressure due to the quenching of excited nitrogen molecules. For a hydrometeor of 0.042 cm^3 volume ($C = ab^2 = 0.01 \text{ cm}^3$) and thundercloud pressure ($\delta = 0.5$), the onset field at the tip varies approximately from $2.4E_k$ (limiting case sphere) to $70E_k$ (sharpest case considered), where E_k is the breakdown field. However, the onset field at the tip is not deemed representative for the likeliness of

corona onset as it does not provide information on the entire surface. These values were also obtained without the inclusion of an ambient electric field. Instead, the onset potential difference, V_0 , can provide a more realistic picture for corona onset, since it can be compared with experimental results. As we can observe, sharper hydrometeors need a lower voltage to initiate a discharge.

Another way to better predict the feasibility of corona onset in thundercloud electric fields is by the derivation of the required ambient electric field E_{bg} from the computed onset field E_0 . This yields values between $0.07 E_k$ and $0.8 E_k$ for semi-axes aspect ratios between 0.01 and 1. Hence, the found ambient electric field is well below the breakdown field. It should be noted that this derived ambient field is neither an upper limit nor lower limit on the field required for onset. While the model gives a minimum condition for corona onset, the found E_0 would be lower if an ambient electric field was included in the model in the first place. Thus, the used assumptions and simplifications should be kept in mind when interpreting these results. However, the ambient field being significantly lower than the breakdown field for representative shapes is very promising.

Whereas the onset field only provides information on the hydrometeor tip and the onset voltage only on the major axis, the onset charge is the total charge on the hydrometeor surface. This onset charge reveals, depending on hydrometeor volume, an optimal semi-axes aspect ratio of the ellipsoidal hydrometeor for which the least amount of charge is required for positive corona onset. The minimum in the onset charge curve is caused by the interplay between required onset field and geometry; a sharper hydrometeor has a larger onset field at the tip and thus requires more charge at the tip, but a larger part of its total charge is located at the tip. As this optimum was not found for the onset field or onset voltage, this suggests that considering only the major axis, which is often done in models for simplification, may not be sufficient when investigating corona onset conditions. Interestingly, in their study on lightning inception from hydrometeors, simulated as dielectrics in an ambient electric field, Dubinova, Rutjes, Ebert, et al. [59] obtain a length-dependent optimum aspect ratio of the hydrometeor that requires the lowest ambient field for discharge inception. In addition, the obtained results can be compared to measured precipitation charges. Generally the hydrometeor charge is measured below 400 pC [124]. For the volume closest to the measured precipitation, $C = 0.01 \text{ cm}^3$, and a relative gas density of $\delta = 0.5$ the onset charge is found to be between and 1500 pC and 3100 pC. However, these charges were measured for estimated hydrometeor diameters between 1 and 3 mm, whereas in the spherical limit the simulated hydrometeors have diameters between 4 mm and 9 mm. In their simulations on spherical hydrometeors using

the same corona inception criterion as this study, Liu et al. have shown that the onset charge varies over several orders of magnitude in the estimated size range of hydrometers. For spherical hydrometeors of 9 mm diameter, the simulated onset charge was near ten times larger than for a 3 mm diameter. With this size correction (roughly a factor 10) onset charge values are close to the hydrometeors charges obtained from in situ measurements. Moreover, the considered configuration is an isolated hydrometeor with zero ambient field. Interaction between hydrometeors (see for example [131]) and a non-zero ambient field would lower the amount of charge required for corona inception, which explains why the found onset charge is higher than expected from in-situ measurements.

Besides the onset charge, the ionization integral K also displays different behaviour in different b/a regions. For hydrometeors with very blunt tips, close to a spherical shape, a larger hydrometeor has a larger K value for onset, as photons are absorbed closer to the hydrometeor with respect to its size. However, for hydrometeors with sufficiently sharp tips, the absolute size of the photon absorption region seems to be more important than its relative size, such that a smaller hydrometeor has a larger value of the ionization integral. For any ellipsoidal shape, the value of the ionization integral is larger at higher pressures, because of the quenching of excited nitrogen molecules, which leads to lessened photon emission and therefore a need for stronger avalanches for corona onset.

To investigate the validity of the results, the approximations and assumptions of the model should be evaluated. Firstly, the distance r_{max} from the tip to the edge of the photon absorption region should be smaller than the hydrometeor length. Using the expression derived in the Appendices B, it is found that for all data points the maximum ratio of this distance to length is $r_{max}/L = 0.2$, meaning this condition for the model to hold is satisfied. Furthermore, the presence of space charges is ignored in the model, leading to an overestimation of the electric field magnitude. When the ionization integral K , or equivalently number of electrons in the avalanche, is large enough, the perturbation of the electric field by the space charge becomes comparable to the magnitude of the electric field itself, such that space charge cannot be neglected. This is accompanied by the transformation of the avalanche into a streamer. In literature, it is often taken that K should be below 14-22 [110], [112] for the perturbation of the electric field by space charge to be neglected. In the results, the value of K is below this threshold for sufficiently blunt hydrometeors. Near $b/a = 0.555$ in Figure 4.6, which is also the cross-over point of the three curves, this value rises above 14. Hence, for sharper ellipsoids possibly more physics should be added to the model to obtain more accurate results.

In the model of the current work, it is assumed that there are sufficient free electrons present for the primary electron avalanche. To be able to draw conclusions on whether corona onset is possible in thunderclouds, it should be considered how these free electrons are supplied, and if this supply is large enough. The source of free electrons for lightning initiation is a widely researched subject, see for example [131], [132]. At least one primary electron is required for discharge initiation, but more electrons lower the inception threshold. When more electrons are available, the requirements on the other factors, such as the aspect ratio and volume of the hydrometeor or amplitude of the ambient field, will be softened.

From the above considerations, it can be concluded that lightning initiation from a spheroidal hydrometeor is feasible. While the onset field at the tip of the charged hydrometeor without ambient field was not found to be below the breakdown field in the considered configuration, the derived onset ambient electric field for the uncharged hydrometeor is lower than this threshold. Further enhancement could be provided by the interaction between hydrometeors. For representative dimensions and pressures, the amount of charge required for corona onset provided by the model is comparable to measured hydrometeor charges. Whether sharper hydrometeors promote lightning onset is a delicate discussion, which depends on which parameters are considered. From our results, it appears that only considering the major axis is not sufficient to reach conclusions on this matter. To further investigate the corona onset from hydrometeors using this model, more physics could be included. Most importantly, the thundercloud ambient electric field could be added to the model. Furthermore, the method can be applied to a hydrometeor cluster. The role of humidity, which was studied by Liu, Dwyer, and Rassoul [111] for spherical hydrometeors, and the low-temperature environment can also be investigated. Finally, the model could be adjusted to account for space charge effects.

5

Lightning inception by hydrometeors: an experimental approach

Abstract

In this study we use an experimental investigation to shed light on the lightning inception problem. From atmospheric observations, it is known that the electric fields in thunderclouds are significantly lower than required for electric breakdown in air. One theory to explain lightning inception is that hydrometeors, i.e. any liquid or solid water particles formed in the atmosphere, greatly enhance the local electric field and can thereby initiate an electron avalanche leading to a streamer discharge. In this study, we investigate streamer initiation in the presence of artificial particles with different shapes. A metal or dielectric (TiO_2) particle is suspended between a high-voltage and a grounded planar electrode which are separated by 16 cm in 50 mbar air. The particles are shaped as ellipsoids with a length of 8, 4, 2, and 1 cm and with different aspect ratios. A negative high voltage pulse is applied with a rise time of 30 ns, a pulse width of 1-10 μs , a repetition rate of 1 Hz, and a maximum voltage between 1 and 50 kV.

Results show that the required background electric field for breakdown in the presence of a dielectric particle is decreased to 0.4 times the air breakdown field. Moreover, we observed bipolar streamer development from the particles where negative streamers are thicker and slightly slower than positive streamers. Finally, we found that streamers from longer particles are thicker and faster.

This chapter is based on [S. Mirpour and S. Nijdam. "Experimental investigation on streamer inception from artificial hydrometeors." to be submitted to Journal of Geophysical Research Letters]

5.1 Introduction

One of the unanswered fundamental questions in atmospheric electricity physics is the lightning inception issue [2], [3], [28], [133]. Observations have shown that the electric field of a thundercloud is much lower (approximately 1/10) than the critical electric field, E_k , required for discharge initiation [107]. One of the main theories to explain this is a streamer-based mechanism for lightning initiation [22]. In this model, a system consisting of a few successful positive streamers can lead to a significant electric-field enhancement at their origin. However, in this model, a main question that remains unanswered is how the very first streamer is initiated under a sub-breakdown field. One main hypothesis that has been developed and discussed is lightning inception by hydrometeors, in which electric fields can be significantly enhanced near the extremities.

A streamer is initiated when an electron is available in a relatively high electric field near the hydrometeor tip where the ionization coefficient is approximately higher than the attachment coefficient. Under such conditions, the number of electrons can start to increase exponentially and eventually result in an electron avalanche. The number of produced electrons should be higher than the so-called Meek criteria [58], which has recently been revisited by Montijn *et al.* [20]. As soon as the number of electrons meets the Meek criterion, the space charge is sufficient to initiate a streamer.

Streamer inception from hydrometeors has been the focus of quite a few theoretical and experimental studies. In most of these, the hydrometeor or ice crystal is considered as a suspended electrode in the gap and is not connected to an external circuit. Petersen *et al.* [40] experimentally investigated streamer inception from ice crystals. They were able to produce ice crystals and place them between two electrodes at low temperatures. They established an empirical formula between the positive corona inception and the temperature and length of the ice particles. They found that positive streamers can be initiated in a lower electric field at temperatures well below -18°C by longer ice crystals. Furthermore, they showed that in addition to ice crystal length, tip sharpness can play an important role. Although ice crystals with sharper tips can increase the field enhancement, an ice crystal with a very sharp tip ($<100\ \mu\text{m}$) can also inhibit positive streamers. In another experiment, Mazur *et al.* [41] used an array of conducting spherical particles in a large-gap, high-voltage setup. They observed bidirectional and bipolar leader development from the particles. They showed that the size of the particle can influence the duration of the discharge. Some questions were not answered in

their study, such as the streamer inception point and propagation velocity, since their observations were limited by leader development and no investigation was conducted regarding primary streamers development.

On the theoretical and numerical side, there have been more complicated and advanced studies on this topic. Sadighi *et al.* [134] modelled a column-shaped ionized patch under sub-breakdown conditions. They found that at an altitude of 7 km, streamers can be initiated from the hydrometeor at $0.3E_k$. This can be achieved for hydrometeors with a length between 5 and 8 mm and an ambient background density on the order of 10^{15}m^{-3} . Because of the importance of the hydrometeor geometry, Dubinova *et al.* [59] investigated the requirements for a large ellipsoid hydrometeor as a function of the background field. They found that streamers can be initiated at lower electric fields from longer and sharper particles. More specifically, at an ambient background density of 100 free electrons per cm^3 , streamer inception is observable from a hydrometeor with a length of 6 cm and a tip radius-to-length ratio of 0.005 at approximately $0.15E_k$. In addition to the shape and size, a unique feature of ice is its dielectric function, which yields a high dielectric constant (approximately 93) at low frequencies and a low dielectric constant of 3 at high frequencies. This can manifest itself in streamer inception where the very first electrons experience almost a DC field, while streamer propagation occurs on the order of a few ns (MHz to GHz). Dubinova *et al.* [21] demonstrated the influence of dielectric properties on streamer propagation and showed that streamers from particles with a dielectric function of ice are lower than those of particles with a constant dielectric permittivity of 93. Notably, when discussing dielectric particles, it is important to consider surface charge accumulation (initial net charge), which was not considered in Dubinova's work. It has been shown that negative charges are accumulated on particles and increase during streamer propagation [135], [136]. This can generally influence the near-tip electric field enhancement, streamer propagation, and inception, especially if we work under repetitive discharges. One important missing piece in theoretical studies is a comparison with experimental data, which can likely show the mentioned effects in a real-life experiment. In chapter 4, we present a theoretical model which investigates the discharge inception criterion near ellipsoidal hydrometeors. We showed that longer and sharper hydrometeors can enhance the electric field near the hydrometeor tip up to $37 E_k$. Furthermore, in line with Dubinova [21] we found an optimal ellipsoidal aspect ratio of 0.1 for corona inception for representative conditions.

In this study, we implemented an experimental approach to understand the discharge behavior near ice-like dielectric particles and compared that with metal particles.

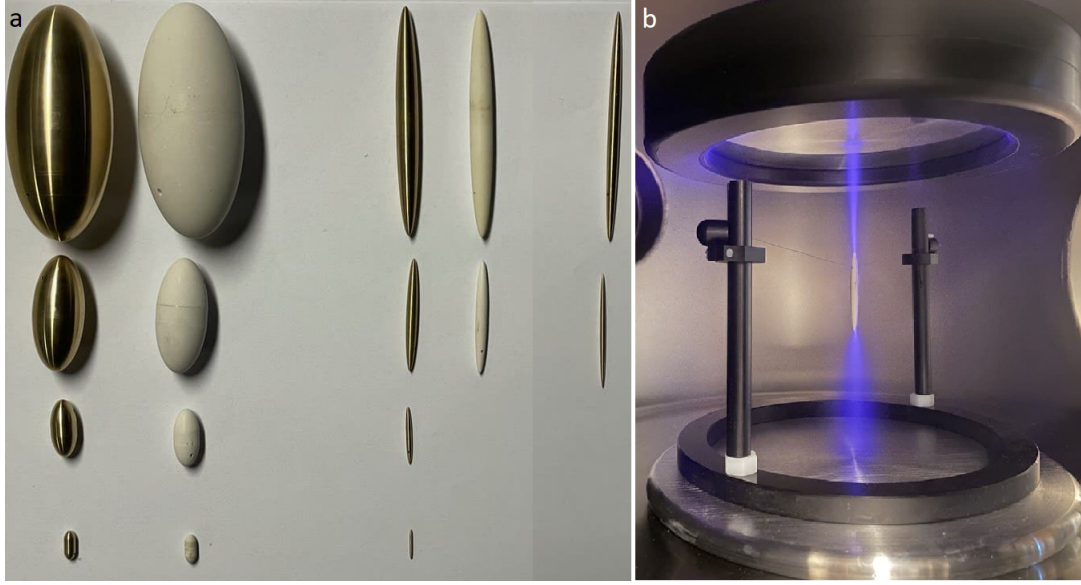


Figure 5.1: a) Metal (Brass) and dielectric (TiO_2) particles used for this experiment, b) long exposure camera image of discharges with a dielectric particle ($L = 4$ cm and $AR = 0.1$) placed between a negative high-voltage electrode ($V_{\text{HV}} = 15$ kV) and a grounded electrode.

Of primary interest in this work are the effects of particle size and shape on streamer inception near particles. Of secondary importance are streamer propagation properties (velocity and thickness) from different particles to understand the role of particle size and shape and its dielectric profile.

5.2 Materials and Methods

5.2.1 Experimental conditions

All experiments in this study were performed in a plane-to-plane geometry in which an ellipsoid dielectric or metal particle ($a =$ semi-major and $b =$ semi-minor axis) was suspended by a thin fishing line (diameter of 0.3 mm) between high-voltage and grounded electrodes (see figures 5.1 and 5.2). Note that no corona formation was detected from the fishing line. The dielectric and metal ellipsoid particles are composed of titanium dioxide (TiO_2) and brass respectively and have varying different tip radii ($R = b^2/a$) and lengths ($L = 2 \times a$). The dielectric particles were formed by annealing and pressing followed by polishing. Table 5.1 shows the metal and dielectric particles used for the experiments based on their shape (R/L) and aspect ratio ($AR = b/a$).

In each experiment, a particle was suspended between negative high-voltage and grounded plane electrodes of 20 cm diameter separated by a fixed 15 cm gap

Table 5.1: List of metal and dielectric particles with different shapes and AR

Length (cm)	Shape R/L	AR b/a	Material
8	0.1	0.44	TiO ₂ and brass
	0.05	0.1	TiO ₂ and brass
	0.01	0.044	brass
4	0.1	0.44	TiO ₂ and brass
	0.05	0.1	TiO ₂ and brass
	0.01	0.044	brass
2	0.1	0.44	TiO ₂ and brass
	0.05	0.1	brass
	0.01	0.044	NA
1	0.1	0.44	TiO ₂ and brass
	0.05	0.1	brass
	0.01	0.044	NA

distance. A high-voltage pulse was applied by a circuit consisting of a high-voltage semiconductor switch (HTS 401-10-GSM, Behlke) and a 1 nF high voltage capacitor. This produced a negative high-voltage pulse with a rise time of 40 ns, a repetition rate of 1 Hz, a pulse width of 1-10 ms and a maximum voltage of 60 kV. The experiments were conducted in synthetic air with a composition of 80% N₂ and 20% O₂ at pressure 50 mbar. To prevent discharges between the high-voltage electrode and the vessel body, we used a PVC rounded insulator around the electrode.

5.2.2 Dielectric properties of TiO₂

To measure the dielectric profile of the dielectric particles, a cylindrical disk from TiO₂ material with a diameter of 3 cm and height of 1 cm was prepared. We measured the permittivity of this material using dielectric material measurement fixtures (1 kHz - 5 MHz: Agilent 16451B and 5 MHz - 10 GHz: Agilent 16453A) and a network analyzer (E5071C Agilent). Figure 5.3 shows the measured relative permittivity of TiO₂ and ice (taken from Mavrovic *et al.* [137]) as a function of frequency. Below 10⁴ Hz, the relative permittivity of ice is approximately 90. In this range, the TiO₂ dielectric constant was measured to be 140±30. The relative permittivity of ice decreases from 90 to 3 at approximately 10 kHz. For TiO₂, the dielectric constant continuously decreases to less than 10. Note that the step in the dielectric constant profile of TiO₂ at 5×10⁶ Hz is due to a switch in measurement device at this frequency and has no physical meaning.

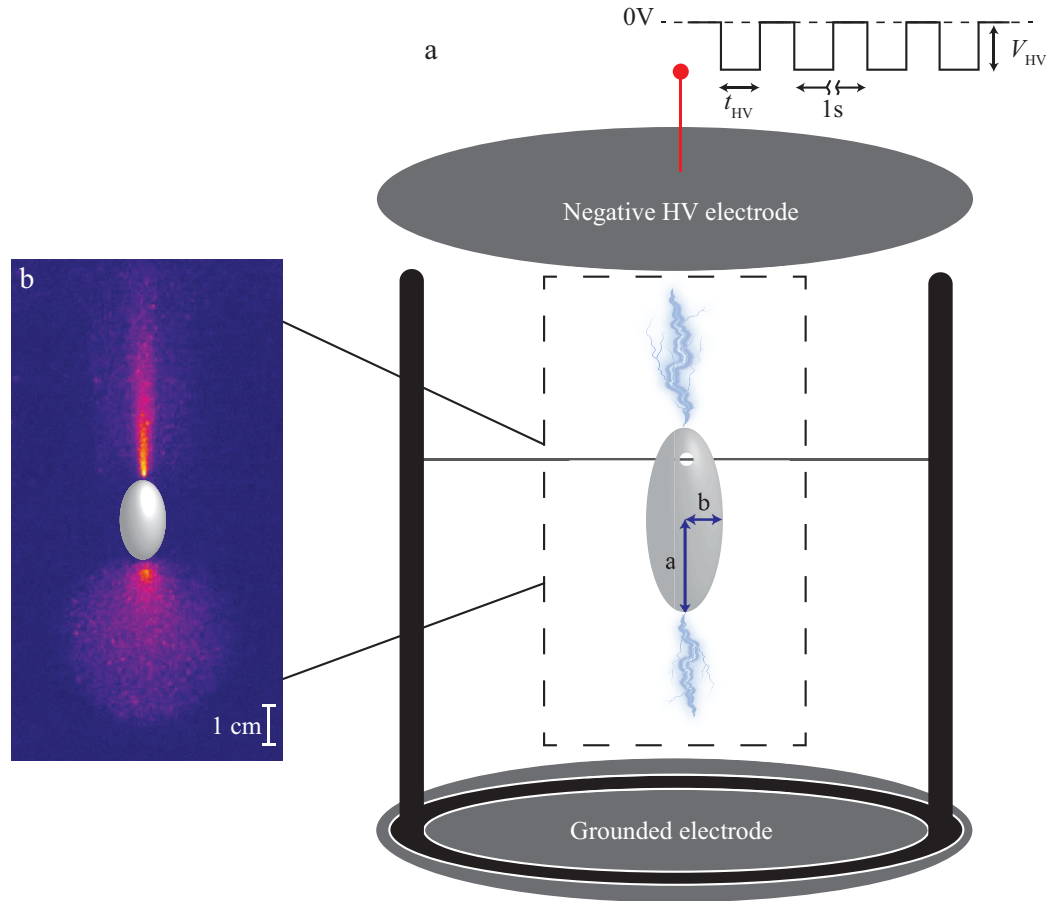


Figure 5.2: a) schematic of the setup where an ellipsoid particle with semi-major axis a and semi-minor axis b is suspended by a thin fishing line between a negative high-voltage and grounded electrode. b) ICCD image of streamer development from a dielectric particle ($a=1$ cm and $b/a=0.44$).

5.2.3 Inception voltage measurements

To collect the photons from the inception phase, a photo-multiplier tube (PMT, Hamamatsu H10720-1 10) with 15 cm lens were placed in front of the vessel to capture photons produced by the corona around the particle tips. The PMT output signal showed a peak for each streamer discharge event. When the peak was 3 times higher than the background level, it was recorded as a streamer initiation. The inception voltage is the voltage at which the discharge initiated. The HV pulse width for these measurements was set to $t_{HV} = 10 \mu\text{s}$ to give enough time to initiate the discharge.

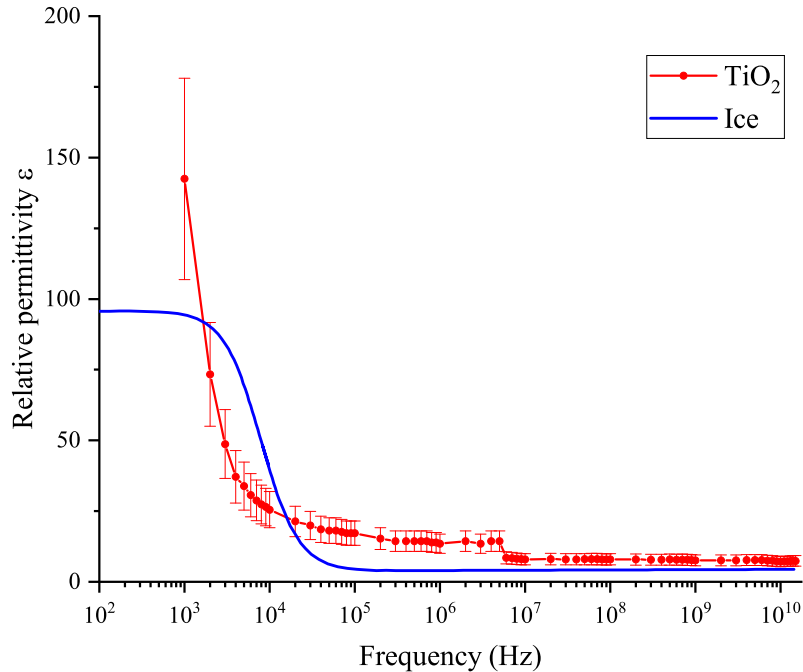


Figure 5.3: Measured relative permittivity of TiO₂ and ice. The data for ice was taken from [137]

5.2.4 Streamers thickness and velocity measurement

To measure the streamer thickness, we used an intensified CCD camera (ICCD, Stanford Computer Optics 4QuickE) with a Nikkor UV 105 mm $f/4.5$ camera lens mounted directly on the camera. The intensifier enabled us to take streamer images with a nanosecond exposure time. The camera was placed in front of the vessel. For better clarity, the output images are rendered in false color. To measure the streamer thickness, the camera gate was open for 300 ns from the beginning of the HV pulse. V_{HV} and t_{HV} of the HV pulse were fixed to 15 kV and 1 μs at 50 mbar, respectively. This is sufficient time for streamers to fully develop and cross the gap. We scaled the applied voltage for different pressures by keeping V/p constant. From the measured images, several cross sections at 0 (tip), 20 %, 40 %, 60 %, 80 % and 100 % (electrodes) of the gap for upward and downward streamers were obtained. The streamer thickness was measured as the full width at half maximum (FWHM) in that cross section as we did that in the previous studies [50].

To measure the streamer propagation velocity, we obtained two images with a very short camera exposure time (5 ns) when streamers crossed half of the gap. The two images were taken with a difference in exposure delay of 10 ns. The velocity was

determined by dividing the distance between streamer head positions in the two images by this delay time. Note that at the applied voltages, we observed low jitter (< 5 ns) during streamer inception, which makes them reproducible.

Finally, The error bars show standard deviation of three independent experiments

5.3 Results and discussion

5.3.1 Streamer inception from particles

We measured the streamer inception voltage from different metal and dielectric particles under a negative HV pulse with a pulse width of $10\ \mu\text{s}$. The inception voltage was the minimum voltage for which we observed a peak in the PMT signal. To support our observation, we made an ICCD-image with a camera gate of $10\ \mu\text{s}$ to observe streamers at the inception voltage.

Figure 5.4 shows the streamer inception voltage from the metal and dielectric particles with different aspect ratios. The measured breakdown voltage for the empty gap is shown as a dashed line. It can be seen that the longer particles with the same aspect ratio had a lower inception voltage. The inception voltage for 8 cm dielectric particles decreased to less than half of the breakdown voltage. At the same length, the sharper particles generally had a lower inception voltage. For 4 cm metal particles, the inception voltage for particles with an aspect ratio of 0.044 was approximately half the inception voltage of the particles with an aspect ratio of 0.44. This was also observed for dielectric particles but less pronounced than for metal particles (the inception voltages of the dielectric particles with aspect ratios of 0.44 and 0.1 were 11.8 and 10.9 kV). Considering the particle materials, the difference between the inception voltages of metal and dielectric particles was not significant. For the 8 cm particles we observed that the inception voltage for metal particles is significantly lower than that of dielectric particles (6 ± 2 kV compared to 9 ± 1 kV). One possible reason for this difference may be the polarization effect of the dielectric. A possible reason may be surface charge density. A large dielectric particle with a larger surface area can carry more charge to influence the streamer initiation. We also observed a similar trend for 25 and 100 mbar pressures (data not shown).

Electric field calculation

Using the Electrostatic module in COSMOL Multiphysics [80], we were able to calculate the electric field in the presence of dielectric and metal particles. For this purpose, a particle ($L = 4$ cm and $AR = 0.044$) was virtually suspended between

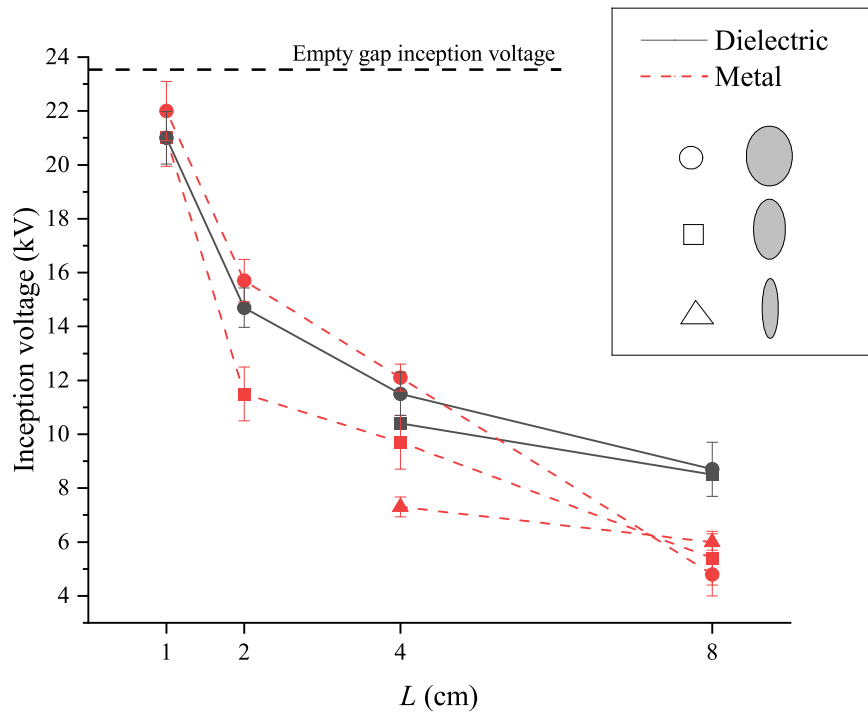


Figure 5.4: Inception voltage with the metal (red) and dielectric (black) particles for different L and AR at 50 mbar in air. \circ , \square and \triangle represent data for the particles with $AR = 0.44$, 0.1 and 0.044 , respectively. The dashed line shows the breakdown voltage without a particle in the gap. The error bars show standard deviation of three independent experiments

two electrodes as described in section 5.2.1. For the dielectric particles, we used isotropic relative permittivity values of 90 and 2. For metal particles, we used a floating potential with no charge on it. In both cases, the top electrode was connected to 12.5 kV (the inception voltage according to figure 5.4). The surface charge accumulation was neglected in this calculation. Additionally, to measure the empty gap inception voltage (at 50 mbar) between two electrodes, the particle was removed, and the top electrode voltage was set to 23.5 kV, as shown in figure 5.4. The results are shown in figure 5.5. The electric field increased near the particle tips to approximately 5 times the empty gap inception voltage. It is important to note that while the field enhancement is greater than the breakdown electric field, electrons need enough space to initiate an avalanche. Hence, streamers need to be initiated at an electric field higher than the breakdown field. Figure 5.5 shows the similarity between the electric field profile of the TiO_2 and metal particles. Obviously, a particle with a lower permittivity (e.g., $\epsilon = 2$) results in less field enhancement, and we expect to require a higher applied electric field to initiate a

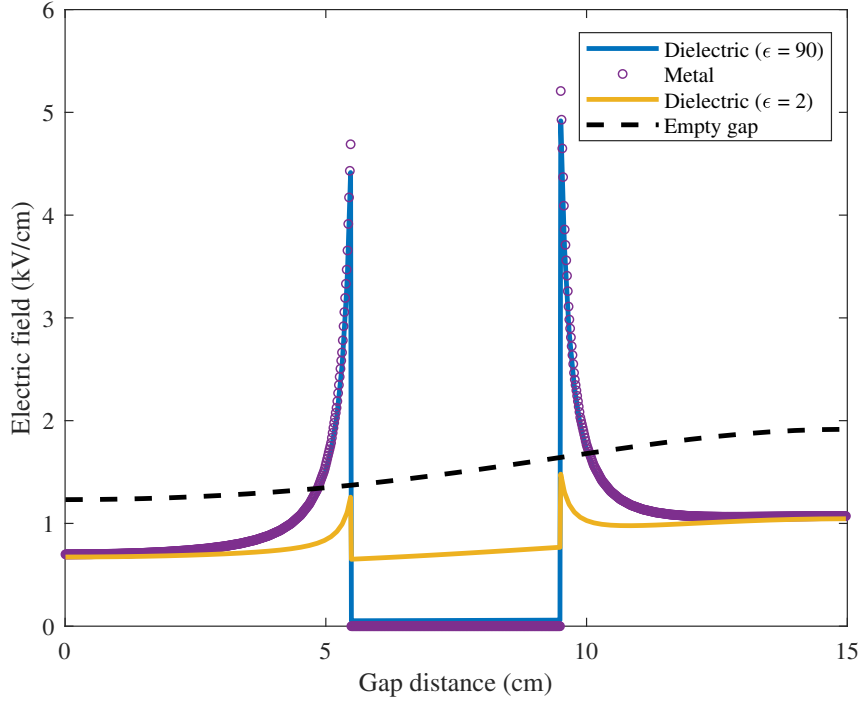


Figure 5.5: Electric field on the center axis of the gap as a function of gap distance to the grounded electrode for dielectric particles with a permittivity of 90 (blue), 2 (yellow) and metal particles (circle) ($L = 4$ cm, $AR = 0.044$) and the gap without particles (dashed black). The high-voltage electrode (breakdown voltage of empty gap = 23 kV (dashed line) and others 12.5 kV) was placed at 15 cm, the grounded electrode was placed at 0 cm, and the particle was placed in the middle of the gap.

discharge. From the electric field profile, we can conclude that because of the similar electric field strength between TiO_2 and metal particles, their inception voltages should be close to each other. This is in line with our measurement in figure 5.4. Note that the asymmetry of the electric field between the top and bottom of the particle is due to the different sizes of the high-voltage and grounded electrodes. We tried to compensate this effect by moving the particle closer to the top or bottom electrodes. However, it was not enough to have an equal electric field on the top and bottom of the particle. Furthermore, we did not include surface charge accumulation of the dielectric particles in our calculations. This might have some effects on the inception voltage. We observed roughly similar profiles for particles with a length of 8 cm (data not shown). The results are in line with the previous modeling work of Dubinova *et al.* [59] in which, at the same $AR = 0.01$, if the length of the hydrometeor increased by a factor of four, the inception voltage was halved (Note that we performed the experiments in a finite gap).

5.3.2 Streamer development from particles

In this section, we study streamer development from the metal and dielectric particles. Figure 5.6 shows the streamer propagation from a dielectric particle with $L = 4$ cm and $AR = 0.44$ under a -15 kV, $1\mu\text{s}$ HV pulse at 50 mbar. Since the top electrode was connected to a negative power supply, a positive streamer initiated from the top of the particle and propagated to the cathode. A positive streamer initiates first due to the lower initiation voltage of positive streamers [1], [138], [139]. After a propagation time of the positive streamers of approximately 75 ns, a discharge initiates on the bottom of the particle. Since negative charges accumulate on the bottom of the particle, a negative discharge begins to propagate towards the grounded electrode. Negative streamers need higher inception fields than positive streamers. Therefore, the positive streamer must propagate some distance to increase the field at the bottom. A similar bipolar discharge from spherical hydrometers was investigated by [135], who showed that positive streamers precede negative streamers due to their lower inception fields. Furthermore, Luque *et al.* [138] showed that for a double-headed streamer discharge, the negative discharge is wider than the positive discharge since negative streamers propagate in the direction of the electron drift. Moreover, they observed that positive streamers are faster than negative due to the higher field enhancement in the narrower positive streamers. In the next sections, we investigate the streamer thickness and velocity under different conditions. Similar results were obtained by Sun, Teunissen, and Ebert [140].

Streamer thickness

Figure 5.7.a shows the thickness of the positive and negative streamers as a function of distance percentage for dielectric particles with $AR = 0.44$. Here, it shows that positive and negative streamers become thicker during propagation. For $L = 4$ cm, the thickness increased to 0.5 cm at 80% of the gap. As the streamers approach the electrodes, we observe that the streamers became thinner. A possible reason for this is the higher electric field when streamers approach the electrodes. In this situation, the proximity effect occurs in which a counter-streamer can be initiated from the electrode that can totally change the streamer behaviour. When comparing particles with different lengths, we observe that streamers from longer particles are thicker. Positive streamers from the particle with a length of 8 cm are 1.8 times thicker than those from the 1 cm long particle at 40% of the gap. This ratio is the same for negative streamers although negative streamers are wider than positive streamers, as discussed above.

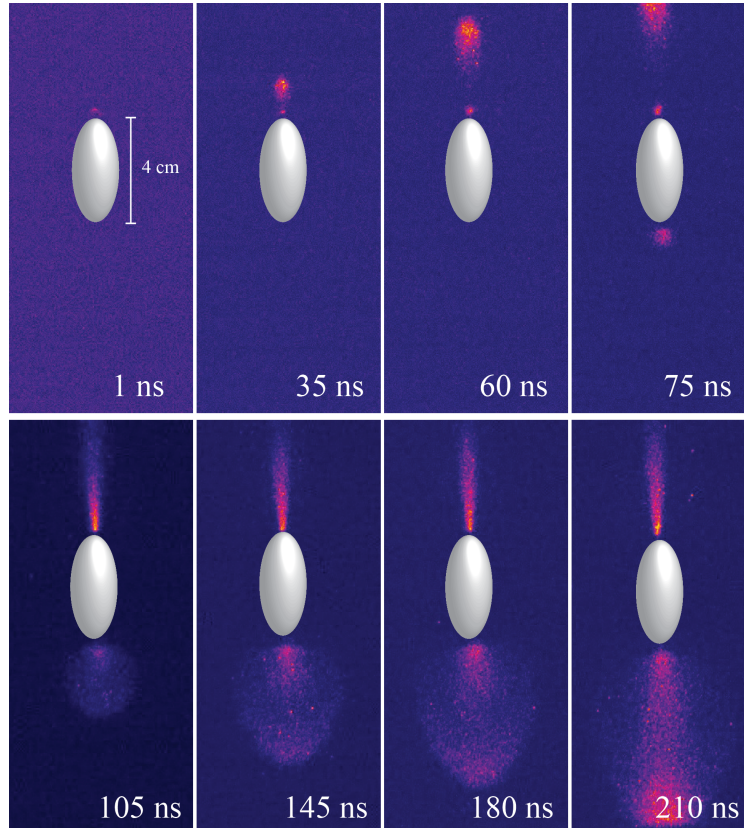


Figure 5.6: Phase resolved images of bipolar discharge development from a dielectric particle with $L = 4$ cm and $AR = 0.44$ in 50 mbar air with $V_{HV} = 15$ kV and $t_{HV} = 1$ μ s in a gap of 15 cm. The camera gate time is 5 ns and the exposure start time with respect to the high voltage pulse is indicated in each image. Each image was taken from a different discharge event under the same conditions.

For a fixed L and varying AR for dielectric particles, figure 5.7.b shows thicker positive streamers from thicker particles. For particles with $AR = 0.44$, the streamer thickness is 0.5 cm at 40% of the gap compared 3.7 mm for the particles with $AR = 0.1$. For negative streamers, the thicknesses are much closer, within the error margins.

Streamer velocity

We have plotted the measured the streamer propagation velocity in figure 5.8. We observe that longer metal and dielectric particles have higher propagation velocities. The streamer velocity for 8 cm long particles was almost twice that of particles with a length of 1 cm. In figure 5.7, we see that longer particles with the same shape had thicker and faster streamers. Moreover, streamer propagation from dielectric particles was faster than that from metal particles. For the 4 cm long particles, the velocity of streamers initiated by the dielectric particles was, on average, 1.2

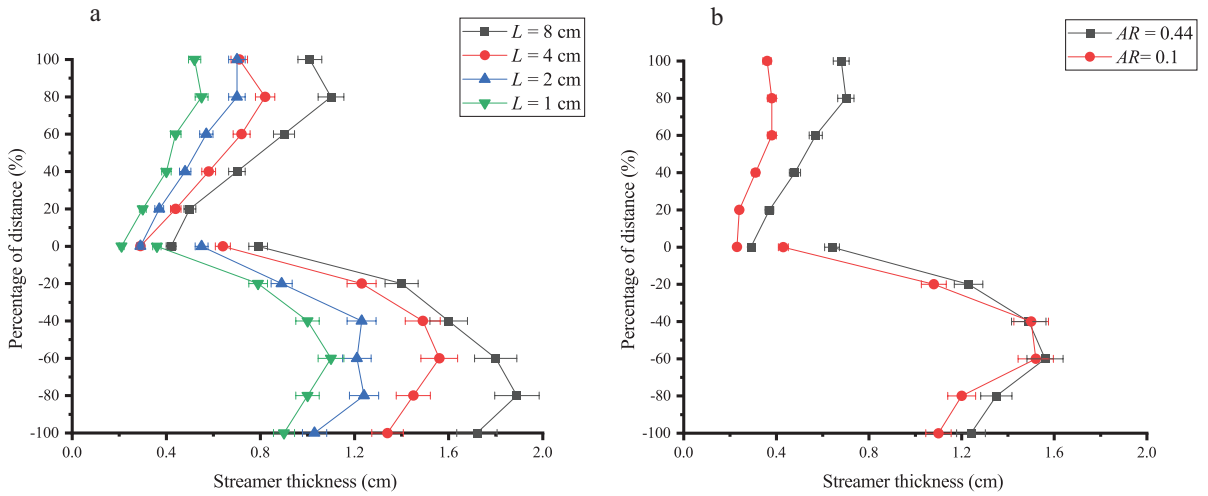


Figure 5.7: Streamer thickness measured from ICCD images from different stages of the streamer development from dielectric particles at 50 mbar in air when 15 kV is applied to the electrode a) at a fixed $AR = 0.44$ and various values of L and b) at a fixed $L = 4$ cm and different values of AR . The top electrode is placed at 100 % and the bottom electrode at -100 % while the top and bottom of the particle are located at 0 %. The error bars show standard deviation of three independent experiments

times higher than that of streamers initiated from the metal particles. Figure 5.5 shows that the electric field enhancement near a TiO_2 particle was slightly less than near a metal particle. However, the average velocity of positive streamers from dielectric particles was higher than streamers that are initiated from metal particles. A possible explanation is that we did not take the surface charge on the dielectric particles into account which might change the electric field distribution near the dielectric particle.

When comparing propagation velocities for different aspect ratios while keeping $L = 4$ cm fixed in figure 5.8b, we see that positive streamers initiated by particles with a blunt tip are faster. The mean positive streamer velocity for a dielectric particle with $AR = 0.44$ was 7.5×10^5 m/s, while for a dielectric particle with $AR = 0.044$, this value was observed to be 5.1×10^5 m/s. Similar to our previous explanation, we observed that the streamer velocity from dielectric particles was higher than from metal particles.

Finally, we compare positive and negative streamers, and observe that positive streamers are slightly faster than negative streamers for the same conditions. This seems to be surprising at the first glance because for negative streamers the space-charge front propagates with the electron drift. However, as Luque *et al.* [138] suggested and we observe in figure 5.7, a thinner positive streamers head leads to more field enhancement and consequently faster propagation while outward drift

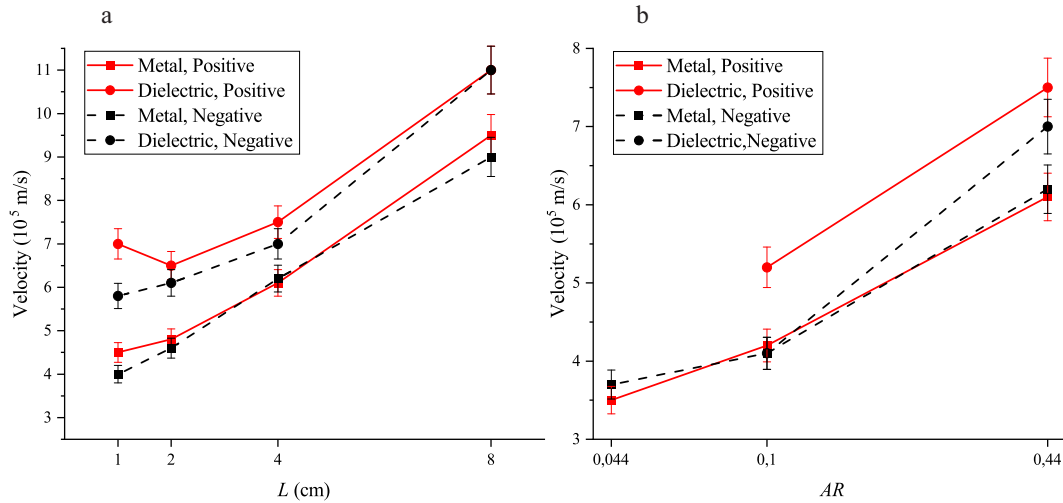


Figure 5.8: Velocity of streamers initiated by particles under a voltage of 15 kV at 50 mbar in air a) at a fixed $AR = 0.44$ and various L , b) at a fixed $L = 4$ cm and different AR . The error bars show standard deviation of three independent experiments

motion of electrons in negative streamers leads to a loss of focus of streamer head and subsequently decrease in field enhancement.

5.4 Summary and conclusions

In this work, we showed that streamers can be initiated from centimeter-size ellipsoidal particles at background fields significantly lower than the classical breakdown fields. In our experiments, we used dielectric particles with a similar profile to ice and compared them with metal particles. We observed that longer and sharper particles resulted in streamer inception as low as $0.4E_k$ (from an 8 cm, $AR = 0.44$ dielectric particle). This is in line with previous experimental results with ice crystals at low temperatures [40]. This shows that to initiate a discharge with field enhancement near a sharp tip, the minimum ionization area close to the tip must provide enough space for the electron avalanche process. This was also predicted by [59], who observed an optimal AR for inception, while a longer and sharper hydrometeor resulted in greater field enhancement near the tip but too little space to start an avalanche. Regarding the real observation of hydrometeor sizes in thunderclouds, the length and shape of particles used in this study must be on the extreme side in a thundercloud, as observations showed that we could have such hydrometeors with a density of 0.1 m^{-3} [141]. Note that in thunderclouds, we might have a system of multiple hydrometeors that can act as a large hydrometeor via inter-discharge connection between particles. From the

dielectric profile measurements and the results obtained during inception, we can conclude that metal particles are very similar to TiO_2 dielectric particles and ice. This shows that in future studies, metal particle models can be used to predict the streamer inception behavior.

A bipolar duo of a positive and a negative streamer initiates from both dielectric and metal particles. First, the positive streamer starts from the positive tip of the particle since positive streamers require a lower electric field to be initiated than negative streamers. After ≈ 75 ns, when the negative charge accumulation on the particle is sufficient, a negative streamer starts to propagate from the other tip of the particle.

Negative streamers are thicker than positive streamers, due to outward drift of the electrons, the streamer head becomes wider which results in less field enhancement. This likely explains our observation that negative streamers are slower than positive streamers. Streamers initiated from longer and thicker particles are faster and thicker. Moreover, streamers from dielectric particles are slightly faster than those from metal particles.

We performed our experiments at room temperature; however, it should be noted that in a thundercloud environment, most lightning may be initiated at altitudes of 4-9 km, where the temperature can be below freezing to -30°C [35]. While [142] reported a significant decrease in the corona current below -18°C , Petersen *et al.* [36] showed that positive streamers can initiate from ice crystals at temperatures as low as -38°C . Moreover, Petersen *et al.* [40] showed that at for constant pressure and ice crystal length, lower temperatures will lead to increased onset fields.

The next parameter to be considered is the source of the very first electron. In thunderclouds, cosmic rays can produce the free electrons that are required for the inception, and Dubinova *et al.* [59] predicted that to initiate a discharge, 100 free electrons/ cm^{-3} are required. Another possible free electron source is electron detachment from metastable oxygen and nitrogen, as suggested by Lowke [45]. In our experiment, we exert the experiments under repetitive pulsed conditions. Previously, we have shown that in repetitive discharges, due to a memory effect, an inhomogeneous distribution of negative ions can be formed and remain for a long time in the gap, which can influence the discharge inception in the preceding pulses [95]. This can induce different effects on the inception voltage and differentiates it from the real situation in thunderclouds.

In summary, we showed that streamers can be initiated from dielectric and metal particles at background electric fields far below the classical breakdown electric field. A bidirectional positive and negative streamer was observed initiating from the tips of the particles.

6

Discharge inception from a laser induced ionized patch

Abstract

This chapter explores a potential new method to initiate streamers. Currently streamers are mostly created in lab conditions using point-plane setups, where they are initiated with a sharp electrode. This is not a perfect representative of streamer inception in the atmosphere where no metal electrodes exist. This chapter aims to solve that by creating an 'ionized patch' by focusing a 532 nm, 6 ns pulsed laser with a maximum pulse energy of 160 mJ at a point between two flat electrodes. A uniform electric field was placed over this laser discharge, leading to the initiation of a wide and diffuse discharge above and below the laser focal point (channel discharge), but not the expected bipolar streamer discharge.

Two hypotheses are proposed to explain this. The sharp rise in electron density is suspected to lead to a local enhancement in the electric field analogous to a high voltage rise time which results in faster and wider streamers compared to point-plane discharges. The other explanation is that this phenomena is not a streamer but a discharge caused by the laser producing enough photons to photoionize the gas throughout the gap, followed by excitation by the resulting free electrons due to the external electric field. The laser discharge also causes a 'dark area' to appear, which is thought to be an area with very high conductivity. This prevents the electric field from penetrating, and exciting the species within, leaving the area dark.

We can conclude that in its current implementation, this new method is not suitable in replacing traditional point-plane setups as the streamers induced have very different properties. However it can still be used to induce diffuse streamers with high velocities at specific points in time and space and may be more successful in larger gaps.

6.1 Motivation

Streamers can be found in nature. Usually they can be observed tens of kilometers high up in the atmosphere. Many related atmospheric electricity phenomena such as sprites, elves, and blue jets have been observed. Red sprites are large-scale and luminous electric discharges that occur above thunderstorm clouds ($\approx 60\text{-}70\text{ km}$) and associated with positive CG (Cloud-Ground) lightning events [143], [144]. High-speed video observations of sprites, show that sprite streamers propagate primarily downward in some cases and both upward and downward with the upper region being more diffuse in other cases [145], [146]. Hence, sprites in some cases are double-headed bipolar discharges which initiate from competing electron in-homogeneities in the lower ionosphere under the lightning-induced electric field.

In streamer simulation studies, often, an in-homogeneous ionized patch is used to initiate a streamer. Qin *et al.* [147] studied single-headed and double-headed streamers to investigate the initiation and development mechanism of streamers inside the sprite halo region. To do this, they used an in-homogeneous electron density profile in their simulation and showed that double-headed streamers can be launched close to the region with $E \approx E_k$ (breakdown field). The upward (negative) streamer initiates from the downward (positive) streamer channel since electron density in these channels is much higher than that in preexisting in-homogeneities in the ambient ionosphere. In another study, Luque *et al.* [138] studied double-headed streamers initiated from an ionization seed in a homogeneous background field. They observed that positive streamers initiated before the negative streamers. Furthermore, they showed that for a spatially concentrated ionization seed consisting of $10^6 - 10^{10}$ electron-ion pairs, streamer velocity is only weakly dependent on the ionization seed.

However, in the laboratory, a sharp electrode is usually used to initiate a streamer (see [139], [148], [149]). Streamers are generated with high electric fields, which heavily depend on the curvature of the anode. Sharp edges make excess charge to bunch up at the tip, causing the electric field (field enhancement) to heavily increase and curve out from the needle point, potentially altering streamer velocity or its trajectory. Streamers generated high up in the air are not caused by any sharp edges so the electric field is expected to be much more uniform. To try and minimize this effect on the electric field, streamers could be initiated between two flat electrodes in order to create parallel field lines. The streamer would ideally originate from a point somewhere between these electrodes, as it does in modelling.

A potential method that can be used for this purpose is to use a high power laser focused at a specific point in between the electrodes. Optical breakdown of gas can be initiated in the focused laser beams for intensities of at least $10^{10} \text{ W} \cdot \text{cm}^{-2}$ [150]. A combination of two processes contributes to the optical breakdown: multiphoton ionization and cascade ionization i.e. Townsend discharge [151]. Multiphoton ionization is simply the process where a molecule is ionized due to absorbing multiple photons with a total absorbed photon energy higher than the ionization energy. It is only important at short wavelengths ($< 1000 \text{ nm}$) and at low pressures ($< 15 \text{ mbar}$), where collisional effects are negligible [152]. At higher pressures, the cascade ionization or Townsend discharge mechanism is dominant. In cascade ionization, free electrons gain energy by absorbing laser energy (inverse Bremsstrahlung) and undergoing elastic collisions with neutral atoms. As soon as the energy exceeds the ionization potential of the gas, molecules start to ionize. The liberated electron is available for the process to be repeated and ionize a large volume [153].

The ionized patch can be used as a seed that is placed between two electrodes. Hence, the aim of this work is to see if it is possible to better explore streamers by using an artificially initiated ionized patch produced by a high power laser induced discharge.

6.2 Setup and Methods

A powerful pulsed Nd:YAG laser (Q-smart 450) with a wavelength of 532 nm a pulse energy of $200\text{-}400 \text{ mJ}$, a pulse length of 6 ns , and repetition frequency of 10 Hz used for inducing the discharges (through multiphoton and/or cascade ionization process) required for the streamer initiation (figure 6.1). An Ophir PE50-DIF-C power meter was used to measure the laser pulse energy for each setting. About 10 cm from the laser, the beam is focused by means of a 20 cm focal length positive lens to a focal point in the middle of the vessel. To achieve lower beam waist sizes and thereby higher local intensities, we also used lenses with shorter focal lengths, 10 cm and 5 cm , of which the latter one had to be placed inside the vessel.

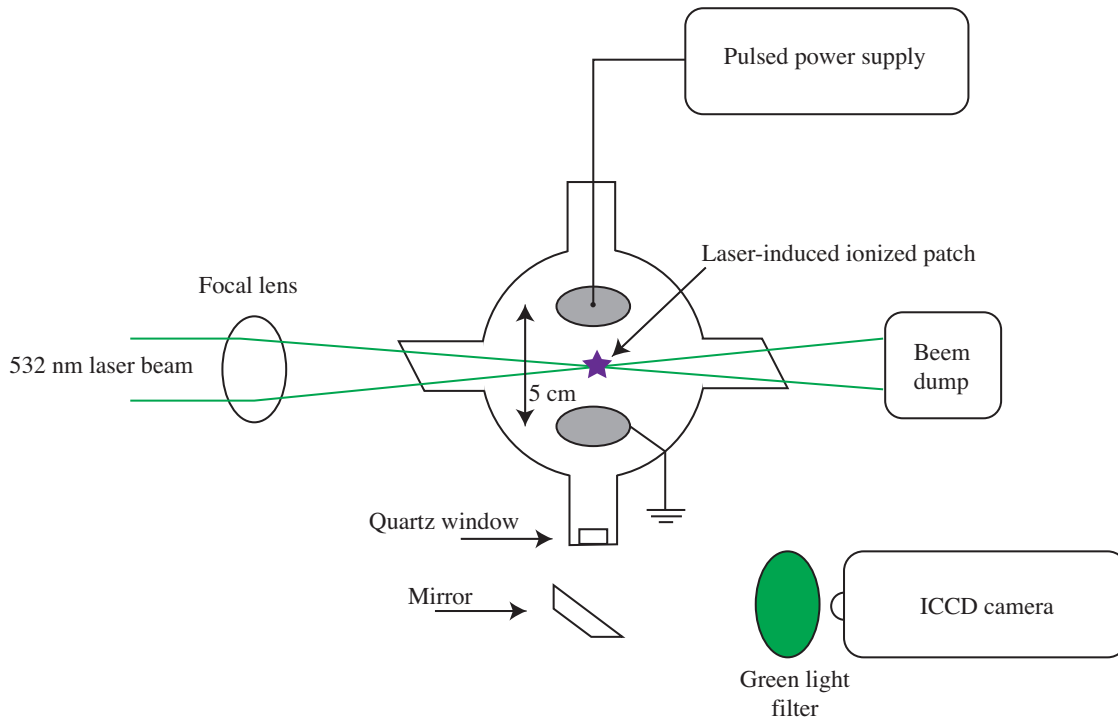


Figure 6.1: A schematic layout of the setup used. The electrodes are omitted from this figure.

The vessel is built around two parallel electrodes with diameters of 4.6 cm which are separated by 5 cm. The bottom electrode is connected to ground and the top electrode is connected to a high-voltage power supply. The power supply setup consists of a Behlke HV switch (HTS 181-01-HB-C) which is connected to a 4700 pF capacitor that is charged by a high voltage DC power supply. This setup can produce relatively short pulses with a pulse width of 200 ns, a rise-time of 20 ns, and an amplitude of 0 – 10 kV. Experiments were performed in 100-500 mbar synthetic air (80 % N₂ and 20 % O₂) and Argon (99.999 %). It should be noted that we applied short HV pulses to the electrode since using long pulses or DC voltage causes electrode-wall discharge. Moreover, in longer applied voltages the formed channel discharge between two electrodes transit into spark discharge and causes overcurrent.

To image the streamer development, we used an ICCD camera (Andor iStar) with a Nikkor UV 105 mm f/4.5 camera lens mounted on it. Due to a lack of space in the lab, the camera is placed sideways in relation to the large viewing window and a mirror is used to view the inside of the vessel. In front of the camera lens is a 532 nm blocking filter, to filter out the scattered green light on the camera. Figure 6.2 shows the timing scheme used for all the measurements. The 200 ns voltage pulse was started 150 ns before the laser discharge fired. The next 50 ns

are thus still under the influence of the voltage. This interval is viewed in its entirety by using a 50 ns camera gate.

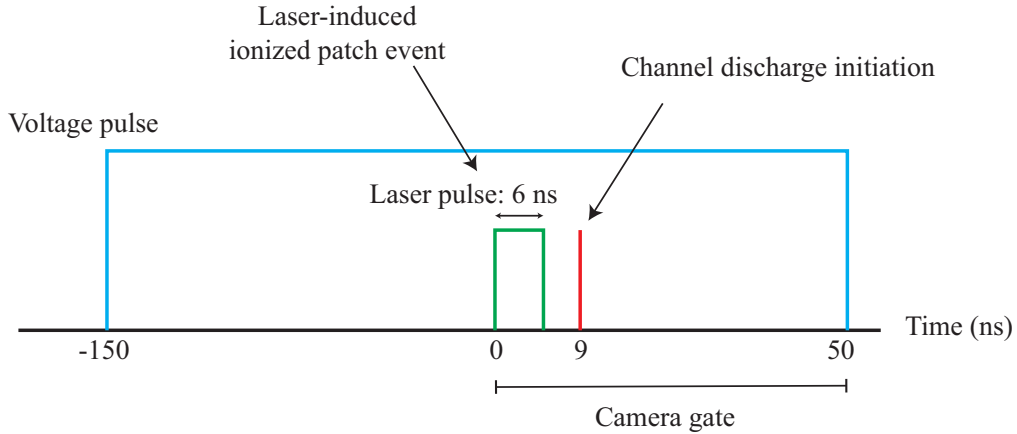


Figure 6.2: Schematic detailing the timings used in the following measurements.

6.3 Results and discussion

6.3.1 Laser-induced ionized patch evolution

Before we look at the effect of an electric field and possible streamer inception, we first investigate the development of the laser-induced discharge in the absence of an electric field. When the laser focal spot intensity increases above the optical breakdown threshold, $10^{10} \text{ W} \cdot \text{cm}^{-2}$ [150], [151] at atmospheric pressure, then the neutral gas starts to ionize at the laser spot and forms a laser-induced "ionized patch". The size of the ionized patch depends on the lens focal length and the pressure inside the vessel. As is shown in figure 6.3, for the 20 cm lens at 100 mbar, we observed a large bright ionized patch with a thin 'tail' in the direction of the laser. With the 10 cm lens (not shown) the end of the thin tail widens while still leaving a thin part in the middle. The 5 cm lens causes the ionized patch length to decrease even more to about 1.5 mm, while also making it more uniformly thick.

Harilal [154] also notes the ionized patch should be round for the first 10 ns, which is not exactly what we observe and show in figure 6.3.a. The shape of the ionized patch afterwards is teardrop shaped at first, with the tail end pointed away from the laser beam direction and the enlarged 'head' pointing towards the laser (figure 6.3.b). This shape is thought to be caused by inverse bremsstrahlung absorption, where dominance of this process would lead to an ionization front absorbing incoming photons, causing it to propagate towards the laser [152]. This effect is more pronounced for higher pressures in figure 6.3.d-f, where inverse bremsstrahlung

is more dominant, while the lack of a large absorption front indicates a larger reliance on the multi-photon ionization process.

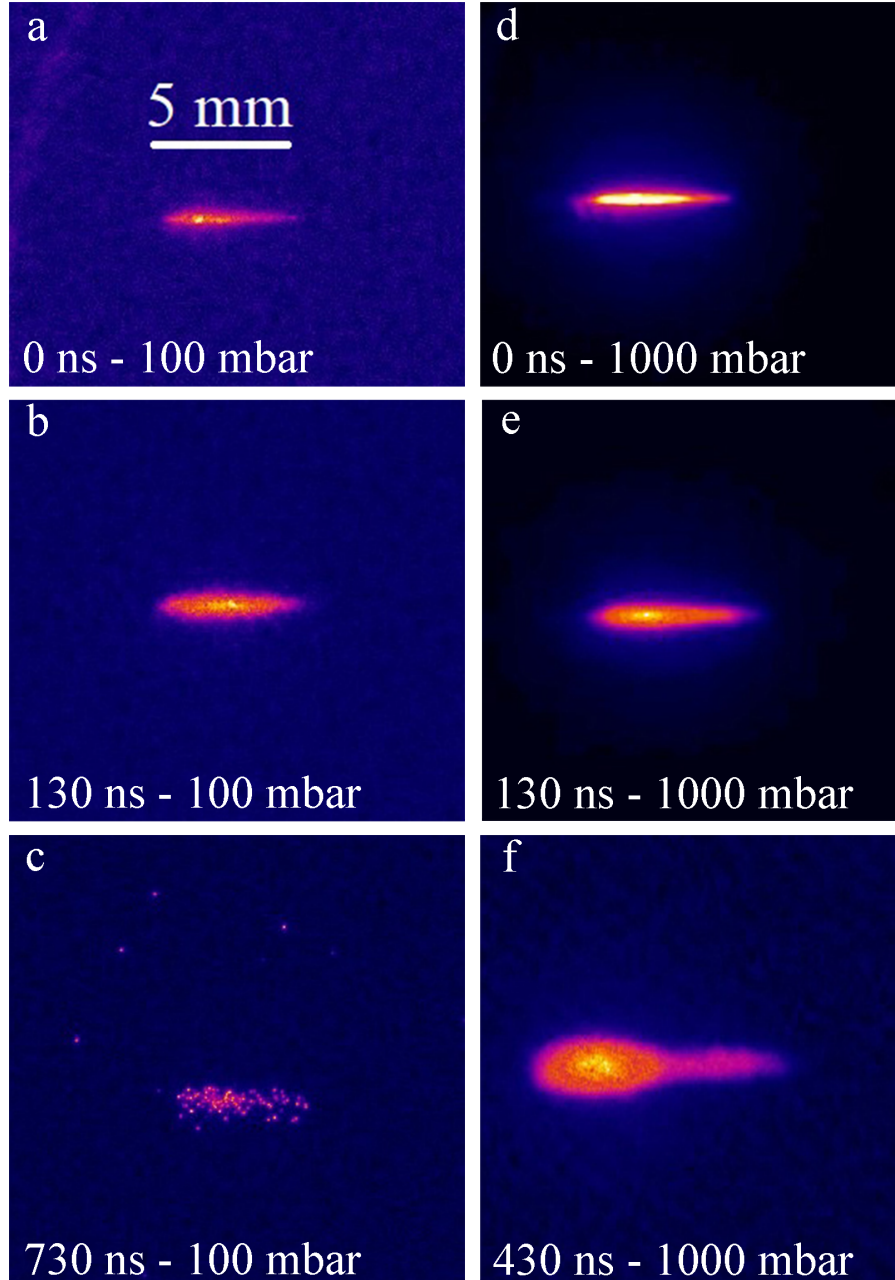


Figure 6.3: The evolution of the ionized patch during time for a-c) 100 and d-f) 1000 mbar in air. The laser pulse energy is set at 120 mJ. The ICCD camera shutter gate is 5 ns. Camera gate opening time with respect to the laser pulse (the laser beam enters from the left side) and pressure are indicated in the images.

A few hundred nanoseconds after the laser pulse (>430 ns), the entire discharge becomes somewhat thicker, followed by the tail becoming as large as the rest of the ionized patch, leaving a long oval shape behind. After a couple of microseconds, the

discharge starts to break up in individual light spots. Note that the light spots that are visible in figure 6.3.c are not camera noise and represent small laser-induced discharges in this case. These stages can be seen in figure 6.3 and coincide with the observations from Harilal and Harilal [154].

6.3.2 Channel discharge initiation from the ionized patch

Next, we apply a high voltage to the the top electrode which creates an electric field between the two planar electrodes around the laser-induced ionized patch. We increase the applied voltage until one or more discharge channels appear in the gap and since the formed discharges appear like as a vertically-developed channel, we call that a "Channel discharge".

Figure 6.4 shows the channel discharge developed from the ionized patch at various pressures, all for an applied voltage of 10 kV. These ICCD images show a very clear "dark area" surrounding the ionized patch. The channel discharge is initiated from the edge of this dark area. The typical height of the dark area is 1 mm on each side of the laser focus. The size of this area decreases with increasing time as no dark area is observable 250 ns after channel discharge development.

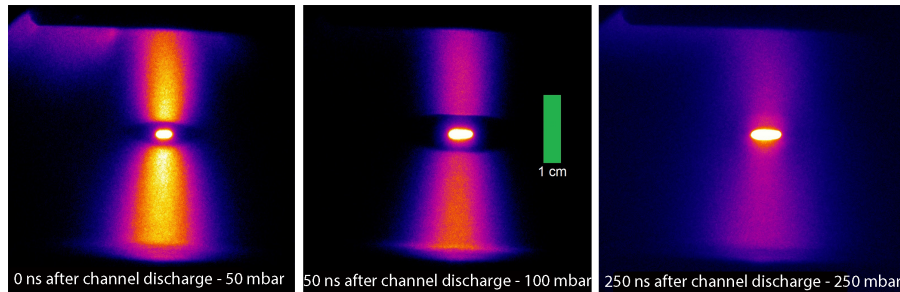


Figure 6.4: Pressure comparison for a channel discharge initiated by ionized patch in argon under a 10 kV pulse of 200 ns. The pressures at 50, 100 and 200 mbar were viewed at 0, 50 and 250 ns after the laser respectively. The focal length of the lens is 10 cm in all cases.

An explanation for the appearance is that the ionization rate near the ionized patch is so high that makes the surrounding area highly conductive. The electric field can not penetrate inside the conductive area, which causes electrons to not accelerate and ionize the gas in that region. The channel discharge does not seem to have the streamer propagation mechanism. By a simple calculation we can estimate that the channel discharge propagation velocity is in the order of 2×10^7 m/s which is much higher than a typical positive streamer [139]. A probable hypothesis is that the high energy photons emitted from the laser discharge photoionize a large

part of the surrounding molecules, creating free electrons. These free electrons would then be accelerated by the field, lighting them up due to excitation. In this case, probably, the discharge is not propagating with streamer mechanism anymore. Since the whole discharge crosses the gas in about 1 ns which is shorter than minimum camera intensifier gate time (2 ns), we were not able to image the discharge development stages.

Figure 6.5 shows that ionized patch becomes more intense with higher input laser power. Also no changes was observed in dark area size. Furthermore, figure 6.5 shows that a laser discharge with enough density is needed for channel discharge initiation in the rest of the gap. These discharges disappear for low laser pulse energies, leaving only a faint ionized patch. This indicates that a certain amount of the electron density is required, and that the laser discharge does not reach the required level at low pulse energies.

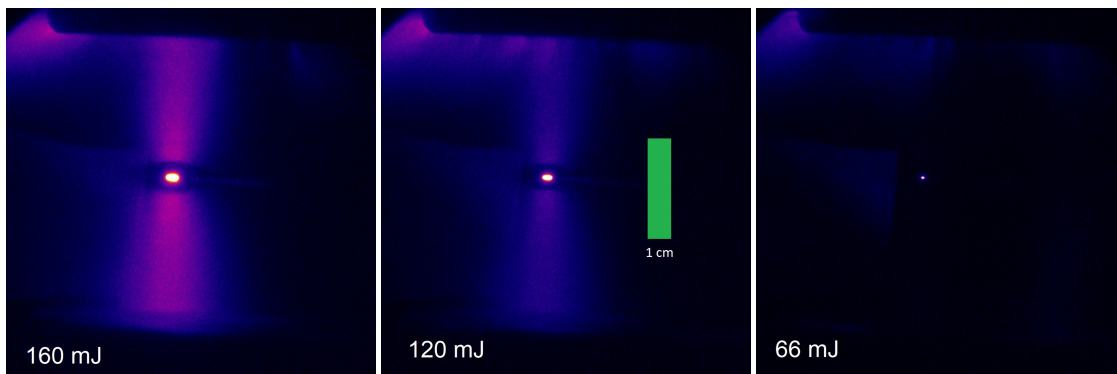


Figure 6.5: Channel discharge measurement with a 5 cm focal length lens at 50 mbar in argon. Each image has a different laser pulse energy.

Comparing the effects of different focal lengths in figure 6.6, and thus ionized patch sizes, shows that the dark area barely changes. Mostly likely this is simply within the margin of error for the ionized patch size, as looking at multiple images shows the dark area slightly moves around and is not completely constant. The variation in size between the different focal lengths is only a few millimeters at most. The discharge images imply that the choice of focal length has a small impact on the discharge for short voltage pulses. The shorter a focal length a lens has, the more intense the laser discharge becomes, which seem to manifest itself in a slightly brighter discharge.

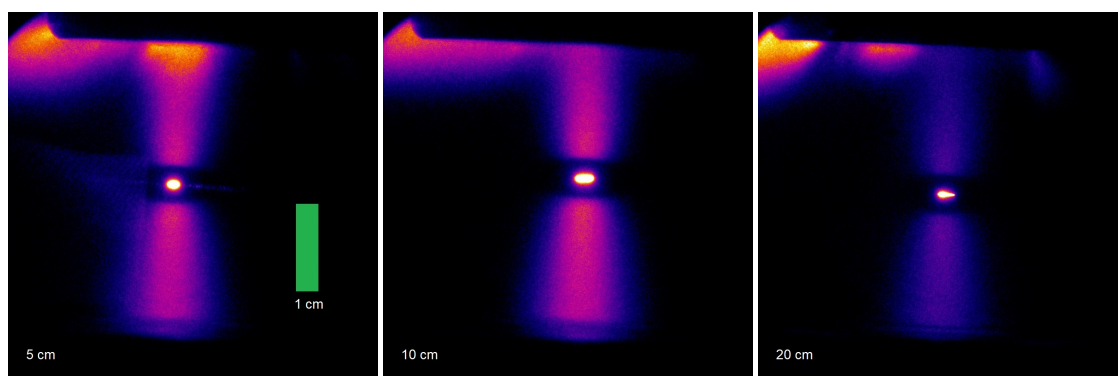


Figure 6.6: Comparison of the laser-induced discharges in air at 50 mbar using a 5, 10 and 20 cm focal length lens. Images were made with a 50 ns camera gate starting at time 0.

6.4 Summary and Conclusion

We used a powerful laser to induce an ionized patch between two parallel electrodes. A channel discharge appears 3 ns after the creation of the ionized patch. The channel discharge develops very fast (<3 ns) from the ionized patch. We observed a dark area around laser-induced ionized patch which can be caused by a conductive area around it due to the higher degree of ionisation that makes it easier for a discharge to be induced from the patch. Other research estimated the plasma temperature in the patch to be around 30000 K, with a rapidly rising electron density [155]. A stronger laser discharge results in a larger conductive area, as the increased power causes more ionisation and increases the conductivity, making it more difficult for an electric field to penetrate it. The electrons thus do not get accelerated enough and cannot excite the species within. A strong dependence on the electric field could also be seen. The propagation velocity of the channel discharges was measured to be much higher than what is expected for streamers, crossing a 1.5 cm gap in less than a nanosecond, reaching velocities around 10^7 m/s. The shape was also much more diffuse and less directed than expected for point-to-plane streamers. This discharge might therefore not be a streamer. To make it more clear a streamer is a nonlinear ionization wave transforms a non-ionized medium into a weakly ionized nonequilibrium plasma. Other research has found similar discharges, named streamers in their paper [156], by applying high voltage with very high rise times to a point-plane electrode setup. It is suspected that the laser induced discharge rapid rise in electron density is analogous to the high rise times, causing similar phenomena. The lack of field enhancement in the setup used might be compensated for by the high initial energy of the electrons coming from the ionized patch.

While the experiments did show that laser induced discharges are possible and useful, a lot can still be done to improve them. Most obvious are the improvements to the setup. A larger vessel would help prevent spark channels to be made with the wall, preventing overcurrents. This would make it possible to use DC sources at higher voltages. Also a larger vessel would help us to investigate the propagation velocity and determine the discharge type (streamers or not). The length of a pulse was shown to not matter much and DC sources can often put out much higher voltages, making higher pressures and gases possible.

7

Conclusion

7.1 Summary and conclusions

In this thesis, we have addressed the fundamental question: How is lightning initiated in thunderstorms? What makes this question such a difficult one to answer is that the measured ambient electric fields in thunderclouds is much below what is required for classical breakdown: E_k . We investigate the hypothesis that lightning inception is assisted by hydrometers, which might be a solution for this question. This approach has two main components: **the availability of free electrons** and **the field enhancement near hydrometers**. Here, We study these aspects both experimentally and numerically, with most emphasis on the experiments. Note that our experimental investigation of this theory has been performed under different conditions than in real thunderstorms. Our experimental conditions included a smaller discharge gap, repetitively pulsed discharges, dielectric particles instead of graupels, and different temperature and humidity conditions than in a thundercloud. In five chapters, we have probed these conditions to find a reasonable answer for the main question. Below, the main conclusions from each chapter are summarized.

Free electron sources in repetitive discharges

Chapter 2: We investigate the free electron sources in repetitive discharges in synthetic air at 500 mbar. We study that by applying 10 ms long 17 kV pulses with a repetition frequency of 2 Hz to a pin-to-plate electrode geometry with a gap length of 6 cm. The free electron sources manifest themselves as three distinguishable peaks at 1) 20 ns, 2) 25 μ s, and 3) 125 μ s in the inception time histogram. This tells us that there are three distinct free electrons sources that build up during repetitive pulsed discharges. Since electrons have charge, they can drift in an

applied field and move toward or away from the anode, at least for low plasma densities, where ambipolar effects do not play a role. To measure this, we have applied a low-voltage (LV) pulse between two main high-voltage (HV) pulses to manipulate the charge distribution positions. We observed that electrons start to move, and consequently inception times start to shift. Using this method, we have shown that the three free electron sources likely originate from: 1) free electrons or electron detachment from negative ions close to the electrode, 2) a process that liberates electrons from (quasi)-neutrals since it seems not to be influenced by the LV pulses, and 3) the drift of an elevated density of negative ions coming from some distance away of the electrode. To validate our theories, we present a theoretical analysis of the distribution of inception times. The results indicate that the third peak is likely caused by a large negative ion concentration consisting of O_2^- located at least 1.5 cm away from the tip. When a positive LV pulse is applied, these O_2^- ions drift to the tip and ionization zone, where they can liberate an electron via the detachment process. During an HV pulse, the detached electron, which is now closer to the tip, starts to drift toward the ionization zone and there can initiate a discharge leading to fast inception. Application of a negative LV pulse causes the O_2^- charged species layer to drift away from the tip and delays inception until, for LV pulses above 50 ms, the third peak is completely removed from the histogram. For the first peak, the effect is different, as the negative LV pulse is not removed when the negative LV pulse is applied. While our hypothesis may describe our experimental observations, at least for the third peak, a significant number of questions still remains, such as: What causes the second peak to form (which is of interest as it shows strange behavior)? What causes the charge layer to become spatially distinct? And, what is the role of plasma chemistry in the inception process? Are we able to observe the same effect for other gas compositions?

Chapter 3: Following the last question proposed in the first chapter, we decided to repeat the same procedure for discharges in CO_2 gas. In this regards we applied a main HV pulse with an amplitude of 10 kV, a pulse width of 1 ms and a repetition rate of 10 Hz. Attached to that we applied an LV pulse with an amplitude of 0-8 kV and pulse width of 0-100 ms. For repetitive HV pulses, and without any applied LV pulse, we observed one peak in the inception time histogram around 1.2 μ s, which indicates that, as in the previous chapter, a non-uniform negative charge distribution formed in front of the tip. We applied a positive or negative LV pulse attached to the main HV pulse. Again, the positive LV pulse causes the peak to shift to faster inception up to a minimum of 50 ns, while the negative LV pulse

delayed inception. However, the results were quite different than expected. We expected that applying a positive LV pulse would have the same but opposite effect as a negative LV pulse. Instead, we observed a factor of a thousand difference in the histogram peak shift between positive and negative LV pulses. This required a different hypothesis regarding the CO₂ inception process.

Electron detachment in CO₂ occurs via associative detachment between CO and O⁻. This reaction continuously liberates electrons, which can drift toward the ionization zone and initiate discharges during a main HV pulse. We have to note that always the closest free electrons to the tip are the ones that cause inception. When we apply a positive LV pulse, electrons drift toward the tip and find a position closer to the ionization zone, which leads to faster inception times. Applying a negative LV pulse, of course, repels the electrons from their initial positions, but O⁻ ions, due to their lower mobility, drift much less than electrons. Hence, the electrons that are produced by ions detachment are closer to the tip and cause inception. To move ions we had to apply a factor of a thousand longer or a higher amplitude LV pulse and this causes the asymmetry. In CO₂, O⁻ can continuously release electrons even in low fields due to high detachment rate which is different from air that is studied in chapter 2.

As an overall conclusion from chapters 2 and 3, the availability of free electrons in thunderclouds can be different from what is seen in laboratory conditions, where, usually, experiments are conducted using repetitive HV pulses. The main difference is in the leftover charges that remain in the gap and can liberate electrons in various reactions. However, with the biasing method that we introduce in those chapters, we are able to identify which sources are contributing to the discharge inception process.

Lightning inception by hydrometers

The next two chapters investigate the theory of lightning inception by hydrometers. Chapter 4: In this chapter, we theoretically investigate the streamer inception criterion near charged hydrometers. This criterion was introduced by Naidis [17] for spheroidal electrodes of various dimensions and pressures. Here, we extend this criterion to ellipsoidal hydrometers of various shapes and lengths. We found that the required onset field at the tip of a hydrometer (with a volume of 0.042 cm³) varies approximately from $1.2E_k$ (the limiting case sphere) to $37E_k$ (the sharpest hydrometer that we considered) at the thundercloud pressure which in this case is 500 mbar. An important note here is that besides the maximum field at the tip, enough space in the vicinity of the tip is also required for discharge inception. As a main conclusion, in general, longer and sharper hydrometers need a lower electric field to initiate a discharge. Moreover, the analysis of the required onset charge

showed an optimum point in its curve. The minimum point in the onset charge curve is caused by the interplay between the required onset field and geometry; a sharper hydrometer has a larger onset field at its tip and thus requires more charge there, but a larger part of its total charge is located at the tip and therefore the field is higher. We also calculated the required background electric field to initiate a discharge and showed that a hydrometer with a length of 40 mm and an aspect ratio (minor axis/major axis) of 0.03 can initiate a discharge at 10% of E_k .

Chapter 5: In this chapter we investigate the lightning inception by hydrometer theory experimentally. Since it is very impractical to use a real ice or graupel, we employed an ceramic particle with a dielectric profile similar to that of ice. We suspended this between two parallel electrodes and compared it with metal particles. We studied the inception voltage, streamer development, thickness, and propagation velocity. As we observed before, longer and sharper particles need lower background fields to initiate a discharge. To compare experimental results with the theoretical results presented in the previous chapter, in experiments, a dielectric particle of 40 mm length with an aspect ratio of 0.044 can initiate a discharge at $0.3E_k$. However, it should be noted that this comparison and extending that to thunderclouds conditions is not a fully valid premise. In the theoretical study we investigate the discharge inception criterion near "charged" hydrometeors while in thunderclouds hydrometeors are assumed to be in an external electric field which polarizes the hydrometeor and turn that to a dipole. In the experimental study, we used a "non-pre-charged" dielectric particle which is suspended between to finite electrodes. This might induce some effects such as uneven distribution of the electric field in the experimental setup because of using finite-length electrodes. We observed that bipolar streamers developed from the top and bottom of the hydrometer. The positive streamer starts earlier than the negative streamer, due to a lower breakdown threshold. Negative streamers are thicker, compared to positive streamers. Furthermore, we observed thicker and faster streamers from longer and thicker particles. Comparing metal and dielectric particles (TiO_2), the results showed a lot of similarities. The field enhancement near the tip in both particles has less than 10% difference. The inception voltage in the most of the cases, the inception voltage, streamer thickness, and velocity difference is not significant. So perhaps in future studies, we may be able to consider metal particles as a suitable candidate for lightning inception investigation.

Chapter 6: In the previous chapter, we learned how streamers were initiated

from dielectric and metal particles. In this chapter, we aim to understand how streamers initiated from an ionized patch. This will put us one step further to bridging the gap between simulation studies and experimental investigations in streamer inception studies. In simulations, usually an ionized patch (or a patch of electrons) with a sufficient density is used in an external electric field to initiate streamers (skipping the first avalanche). However, in experiments, usually a sharp electrode provides the local high electric field and streamers initiate from the tip of the electrode. In this chapter, we see that an ionized patch is produced by a powerful laser focused at a point between two parallel electrodes with a gap size of 30 mm. We observed a conductive dark area around the patch, which might be caused by the high ionization density of the patch. Glowing discharge channels form on the top and bottom of the patch. We did not observe any streamer-like development from the patch. Perhaps because of the high ionization rate and small discharge gap size we observed a glow discharge in the gap. We concluded that this setup is not suitable for studying streamer development. However, a more advanced experimental setup is required to draw more clear conclusions.

Now it is time to answer the main question that we asked in the introduction: *is the hydrometer theory a suitable candidate for solving the lightning inception problem?* Based on the theoretical and experimental evidence that we gathered in this thesis, it can be concluded that this theory is a possible solution for the lightning inception problem. However, the differences between experimental conditions and thunderclouds, such as differences in temperature, humidity level, turbulence, and the phase and size of the hydrometers should still be considered. We will address them again in the outlook section.

7.2 Outlook

Lightning inception problem

- In the experimental study on hydrometer inception, an important topic that we did not address in our investigations is the use of an array of hydrometers, or the equivalent, instead of focusing on a single particle. This could be very important for our understanding of the discharges between the particles and how such discharges can affect the discharge inception. Moreover, inside the vessel, we used a dielectric that has a dielectric profile close to ice. However, it is best to use ice crystals for the experiments. A possible way to do this is to cool down the vessel to a temperature close to that of the thundercloud's

ambient temperature (≈ -30 °C) and suspend an ice crystal between two parallel electrodes.

- In the theoretical exploration, we model the streamer inception near charged ellipsoidal conductors. However, in actual thunderclouds conditions, hydrometeors are assumed to be in an external electric field. The external field polarizes the hydrometeor so that it becomes a dipole. In the modeling presented in this thesis, there is only an electric field generated by the charge on the hydrometeor, which is different from real lightning. While the effects of the field induced by a charged particle can already tell us a lot of what particle shape and size can do for discharge inception, in future studies we have to implement external electric fields.
- To have a better understanding from streamer development, we have to set up a larger vessel with a greater gap distance. This will allow us to study two different topics in addition to streamer development: streamer-to-leader transition and x-ray radiation. We do not have a clear criterion for streamer-to-leader transition, but that can be resolved in this setup. Furthermore, the x-ray radiation from two colliding streamers initiated by hydrometers might be a very interesting topic. Doing this experiment in a large gap will give us the opportunity to have a more uniform electric field, due to the small ratio of the size of hydrometer to the electrode diameter.

Discharge inception in technology

- A more detailed examination of the formation of the localized ion distribution in repetitive pulsed discharges is required. In general, our knowledge on the background ionization density before streamer inception is not sufficient. One problem that is associated with this is the low density of background ions, which makes them difficult to diagnose with current diagnostic methods such as Laser-induced fluorescence and Raman spectroscopy. An idea that can be helpful for this challenge is to use a very sensitive pico (femto)-amp meter to measure the current caused by background charges flowing in the electric field between two parallel electrodes. From the modeling point of view, repetitive discharges are not yet well-implemented, due to the long time scale of such simulations. Developing a more sophisticated model will help us to better understand this topic.

- The role of humidity in discharge inception must be studied. Adding water droplets to the experimental vessel is very challenging, since in addition to problems such as condensation on the vessel body, the plasma chemistry would also be a lot more complicated.
- One idea that can improve our knowledge of streamer propagation initiated by hydrometeors/or electrodes is using time-resolved detectors. We used an ICCD camera for our studies which takes one single image at a time. Studying streamers near inception voltage can be associated with high jitter in the streamer initiation, making it difficult to study the streamer development. One idea which can be helpful is using a streak camera. A streak camera is a powerful tool for measuring ultra-fast light phenomena and delivering intensity vs. time vs. position information. Using a streak camera, we can have a complete picture of the streamer development during one high-voltage pulse. Above jitter problem, avalanche process in streamer inception is a low-light phenomenon. To detect avalanche events, we have to employ a single-photon detector. This can be done by single-photon avalanche diode (SPAD) detectors which are extremely efficient at detecting a single photon.
- Another very important topic is surface charge accumulation. As we have also observed in our experiments, surface charges can affect discharge inception as well as streamer propagation. A recent method, called "E-FISH" (electric field induced second-harmonic generation), can measure temporally and spatially resolved electric fields in a gas using laser beam interacts non-linearly with the ambient electric field in a medium. This method can be employed to measure the electric field near the hydrometer tip at different times after streamer development to determine the charge on the surface of the dielectric.

Appendices



Inception probability in air discharges

A.1 Analytic estimate for inception probability

In this appendix, we derive an analytic estimate for the probability of inception when only drift is taken into account; effects due to reactions, diffusion or space charge are neglected.

Suppose that a single O_2^- ion or electron is present in the discharge vessel, with a spatially homogeneous probability distribution. For simplicity, we assume that inception occurs when this particle reaches the HV electrode (for the O_2^- ion, an electron would be liberated through detachment in the high field around the electrode). The probability of inception is then equal to the probability that the particle has reached the HV electrode in a time t , which we denote by $F_1(t)$.

As discussed in section 2.5.2, we can assume the particle flux (or its probabilistic equivalent) to be constant in time until boundary effects due to the finite vessel size become relevant. The underlying assumptions are that the field is divergence-free, that the mobility is constant, and that the initial density is homogeneous. If the flux is constant, then we have $F_1(t) \propto t$. If we assume that any particle reaches the HV electrode within a time t_{\max} , then we can write

$$F_1(t) = t/t_{\max}, \quad (\text{A.1})$$

in other words, the inception probability linearly increases with time from zero to one. If there are N initial particles, the probability of inception $F(t)$ is one minus the probability that inception did *not* occur

$$F(t) = 1 - (1 - F_1(t))^N,$$

so that the probability density of inception $f(t)$ is

$$f(t) \equiv \partial_t F(t) = N(1 - F(t))^{N-1} \frac{dF(t)}{dt}. \quad (\text{A.2})$$

Plugging in equation (A.1), the result is

$$f(t) = N/t_{\max}(1 - t/t_{\max})^{N-1}. \quad (\text{A.3})$$

For large N and $t/t_{\max} \ll 1$, this can be approximated by $f(t) \approx k(1 - kt)$, where $k = N/t_{\max}$. To a good approximation, the dependence on k instead of N and t_{\max} individually also holds at later times. This means that the specific values used for N and t_{\max} are not important, only their ratio. One could for example consider a volume around the electrode containing $N \gg 1$ initial particles, and let t_{\max} denote the maximal drift times of these particles to the electrode.

B

Derivations related to the hydrometeors
model

B.1 Derivation of the distance ρ_0

To find the distance ρ_0 from the major axis to the surface of the ellipsoid along the surface electric field direction, the equation defining the ellipsoid (with the origin at the tip of the ellipsoid)

$$\frac{x^2}{b^2} + \frac{y^2}{b^2} + \frac{(z+a)^2}{a^2} = 1 \quad (\text{B.1})$$

is reformulated in spherical coordinates, which yields

$$\frac{r^2 \sin^2(\theta)}{b^2} + \frac{(a+r\cos(\theta))^2}{a^2} = 1. \quad (\text{B.2})$$

Solving equation (B.2) for r gives two solutions, valid separately for $\theta \leq \pi/2$ and $\theta > \pi/2$, namely

$$r = \begin{cases} 0 & \theta \leq \pi/2 \\ \frac{2ab^2 \cos(\theta)}{(a^2 - b^2) \cos^2(\theta) - a^2} & \theta > \pi/2, \end{cases} \quad (\text{B.3})$$

as the range $\theta \leq \pi/2$ is the ionization region, which only encompasses the tip, $r = 0$, of the ellipsoidal surface (see also Figure 4.2). Substituting these solutions into the expression for ρ_{ab} (equation (4.4) and Appendices), thus constraining ρ_{ab} to the surface of the ellipsoid, gives

$$\rho_0 = \begin{cases} \frac{(a - \sqrt{a^2 - b^2}) \sqrt{2a(\sqrt{a^2 - b^2} + a) - b^2}}{a} & \theta \leq \pi/2 \\ \frac{4(2a(\sqrt{a^2 - b^2} - a) + b^2 + p_2) \sqrt{\frac{4ab^2(2\sqrt{a^2 - b^2}) \cos^2(\theta)}{(a^2 - b^2) \cos^2(\theta) - a^2} + 2a(\sqrt{a^2 - b^2} + a) - b^2 - p_2}}{2a(\sqrt{a^2 - b^2} - a) + b^2 - \frac{p_1}{8} + p_2}}{\frac{4ab^2 \sqrt{a^2 - b^2} \cos^2(\theta)}{(a^2 - b^2) \cos^2(\theta) - a^2} + b^2 + \frac{p_1}{8} - p_2}} & \theta > \pi/2, \end{cases} \quad (\text{B.4})$$

with

$$p_1 = 8\rho_1\rho_2 \left(r = \frac{2ab^2 \cos(\theta)}{(a^2 - b^2) \cos^2(\theta) - a^2} \right)$$

and

$$p_2 = -\rho_1^2 \left(r = \frac{2ab^2 \cos(\theta)}{(a^2 - b^2) \cos^2(\theta) - a^2} \right) - 2a(\sqrt{a^2 - b^2} - a) - b^2$$

B.2 Derivation of the distance ρ_{ab}

The distance ρ_{ab} the point of photon absorption, which will now be referred to as the 'observation point', is in the direction of the electric field. This direction is given by the bisector of the two straight lines from the focal points of the spheroid to the observation point [130]. The bisector ρ_{ab} is depicted in Figure B.1.

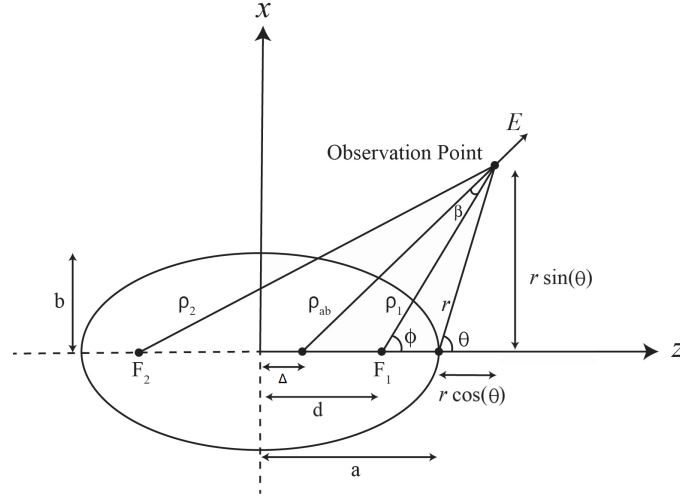


Figure B.1: Schematic of the bisector giving the electric field direction outside a conducting ellipsoid.

Since the origin of the spherical coordinate system in Figure B.1 is placed at the tip of the ellipsoid on the positive z -axis, the lines from the focal points to the observation point given by $\rho^2 = x^2 + y^2 + z^2$ become in spherical coordinates:

$$\begin{aligned}\rho_1^2 &= (r \sin \theta)^2 + (a - d + r \cos \theta)^2 = r^2 + (a - d)^2 + 2(a - d)r \cos \theta, \\ \rho_2^2 &= (r \sin \theta)^2 + (a + d + r \cos \theta)^2 = r^2 + (a + d)^2 + 2(a + d)r \cos \theta,\end{aligned}\quad (\text{B.5})$$

with coordinates as given in Figure B.1 and the linear eccentricity $d^2 = a^2 - b^2$. Using the law of cosines, the angle 2β between these two lines ρ_1 and ρ_2 is given by:

$$\cos(2\beta) = \frac{1}{2\rho_1\rho_2} (\rho_1^2 + \rho_2^2 - 4d^2). \quad (\text{B.6})$$

Using the trigonometric identity $\cos(2\beta) = 2\cos^2\beta - 1$ the cosine of the angle between ρ_{ab} and ρ_1 is found:

$$\cos(\beta) = \sqrt{\frac{1}{2} + \frac{1}{4\rho_1\rho_2} (\rho_1^2 + \rho_2^2 - 4d^2)}. \quad (\text{B.7})$$

The acute angle ϕ between ρ_1 and the z -axis follows from:

$$\sin \phi = \frac{r \sin \theta}{\rho_1}. \quad (\text{B.8})$$

Since the acute angle between ρ_{ab} and the z -axis is given by $\phi - \beta$, it can be concluded that

$$\rho_{ab} = \frac{r \sin \theta}{\sin(\phi - \beta)}, \quad (\text{B.9})$$

where β and ϕ are given by Equations B.7 and B.8, respectively. The final expression for ρ_{ab} can be formulated more compactly by applying the trigonometric identity $\sin(\phi - \beta) = \sin(\phi) \cos(\beta) - \cos(\phi) \sin(\beta)$. Figure B.1 shows that $\cos \phi = (r \cos(\theta) + a - d)/\rho_1$. Moreover, the law of sines applied to the triangle with the observation point and the two focal points as vertices in Figure B.1, in combination with the trigonometric identity $\sin(2\beta) = 2 \sin(\beta) \cos(\beta)$, gives $\sin(\beta) = \sin(\phi)d/\cos(\beta)\rho_2$. Finally, the following expression for ρ_{ab} is obtained:

$$\rho_{ab} = \frac{\sqrt{2}\rho_1^2 \sqrt{\frac{(4\sqrt{a^2-b^2}(a+r\cos(\theta))+\rho_1^2)(2ar\cos(\theta)+b^2+\rho_1\rho_2+r^2)}{\rho_1\rho_2}}}{\rho_1^2 + \rho_1\rho_2}, \quad (\text{B.10})$$

with ρ_1 and ρ_2 the straight lines from the two focal points of the ellipsoid to the observation point (see also Appendix B.2) given by

$$\rho_1 = \sqrt{r^2 + (a - \sqrt{a^2 - b^2})^2 + 2(a - \sqrt{a^2 - b^2})r \cos \theta}, \quad (\text{B.11})$$

$$\rho_2 = \sqrt{r^2 + (a + \sqrt{a^2 - b^2})^2 + 2(a + \sqrt{a^2 - b^2})r \cos \theta}, \quad (\text{B.12})$$

This expression reduces to $\rho_{ab} = \sqrt{(r \sin \theta)^2 + (\rho_0 + r \cos \theta)^2}$ for a sphere of radius $a = b = \rho_0$.

B.3 Derivation of the electric field $E(\rho, r, \theta)$

The electric field of a conducting ellipsoid has been derived analytically by Köhn and Ebert [128] for the prolate spheroid case and by Curtright, Cao, Huang, et al. [130] for arbitrary dimensions. The derivation of the electric field strength E yields

$$E(x, y, z) = \frac{Q}{4\pi\epsilon_0} \left(\prod_{k=1}^3 \frac{1}{\sqrt{a_k^2 + \Theta}} \right) / \sqrt{\left(\sum_{m=1}^3 \frac{x_m^2}{(a_m^2 + \Theta)^2} \right)}, \quad (\text{B.13})$$

where Q is the charge on the ellipsoid surface, ϵ_0 is the vacuum permittivity, and $a_1 = a_x = b$, $a_2 = a_y = b$ and $a_3 = a_z = a$ are the semi-axes of the ellipsoid. Moreover, the Θ -equipotentials follow from

$$\sum_{k=1}^3 \frac{x_k^2}{a_k^2 + \Theta} = 1, \text{ for } \Theta > 0. \quad (\text{B.14})$$

Solving equation (B.14) for Θ gives

$$\Theta = \frac{1}{2} \left(\sqrt{(-a^2 - b^2 + x^2 + y^2 + z^2)^2 + 4(-a^2b^2 + a^2x^2 + a^2y^2 + b^2z^2)} - a^2 - b^2 + x^2 + y^2 + z^2 \right). \quad (\text{B.15})$$

Substituting this in equation (B.13) and converting to spherical coordinates (ρ', θ', ϕ') with the origin at the center of the ellipsoid yields an expression for the electric field in terms of ρ' , the radial coordinate from the center of the ellipsoid, and θ' , the azimuthal angle for the origin at the center of the ellipsoid. Using the trigonometric relations

$$\theta' = \tan^{-1} \left(\frac{r \sin(\theta)}{a + r \cos(\theta)} \right) \quad (\text{B.16})$$

and

$$\cos(2 \tan^{-1} u) = (1 - u^2)/(1 + u^2), \quad (\text{B.17})$$

with $u = \frac{r \sin(\theta)}{a + r \cos(\theta)}$, the obtained electric field expression can be rewritten in the desired θ coordinate. Note that the conversion from θ' to θ can be done in multiple (equivalent) ways using the tangent, sine or cosine. Now, the radial coordinate ρ' needs to be converted to the ρ coordinate along the electric field direction. This is done using the expression for ρ_{ab} , which is the distance to point of photoionization along the ρ coordinate and is given by equation (B.10). By simple trigonometry the following relation can be derived

$$\rho' = \sqrt{2a\Delta - \Delta^2 + \rho^2 + 2\Delta r \cos(\theta)}, \quad (\text{B.18})$$

with $\Delta = \Delta(r, \theta) = a - \sqrt{\rho_{ab}^2 + \frac{1}{2}r^2 \cos(2\theta) - \frac{r^2}{2}} + r \cos(\theta)$ the distance between the center of the ellipsoid and the intercept of ρ_{ab} with the major axis and with ρ_{ab} given by equation (B.10). Writing out equation (B.18) gives

$$\rho' = \sqrt{\frac{2ar \cos(\theta)(3a^2 - 3b^2 + \rho^2) + 2a^2\rho^2 + a^2\rho_1\rho_2 - b^2\rho^2 - b^2\rho_1\rho_2 + \rho^2r^2 + \rho^2\rho_1\rho_2 + p}{2a^2 + 2ar \cos(\theta) - b^2 + r^2 + \rho_1\rho_2}}, \quad (\text{B.19})$$

with $p = 2a^4 - a^2b^2 + 2a^2r^2 \cos(2\theta) + a^2r^2 - b^4 - 2b^2r^2 \cos(2\theta) - b^2r^2$. Thus, equation (B.18) allows us to convert ρ' to ρ . However, as r is also a function of ρ' through $\rho' = \sqrt{a^2 + r^2 + 2ar \cos(\theta)}$ (or equivalently $r = \sqrt{\frac{1}{2}a^2 \cos(2\theta) - \frac{a^2}{2} + \rho'^2} - a \cos(\theta)$), this derivation is not complete. Substituting the expression for r in terms of ρ' in equation (B.18) gives an equation that is not analytically solvable. Ideally, an electric field would be obtained that is only a function of ρ and θ . As an analytical expression is required for the model, the expression for the electric field in terms of ρ , r and θ is now accepted, given by

$$E(\rho, r, \theta) = \frac{2b^2 E_0 \rho'}{\sqrt{a^2 - b^2 + q + \rho'^2} (-a^2 + b^2 + q + \rho'^2) \sqrt{\frac{q}{\frac{(b^2 - a^2)(a^2 + 2ar \cos(\theta) + r^2 \cos(2\theta))}{a^2 + 2ar \cos(\theta) + r^2} + q + \rho'^2}}}, \quad (\text{B.20})$$

with the shorthand $q = \sqrt{\frac{2\rho'^2(b^2 - a^2)(a^2 + 2ar \cos(\theta) + r^2 \cos(2\theta))}{a^2 + 2ar \cos(\theta) + r^2}} + (a^2 - b^2)^2 + \rho'^4$ and where ρ' is converted to ρ using equation (B.19). As eventually the $\gamma = 1$ equation is solved numerically, the dependence of r is not a problem as long as the resulting α_{eff} (which depends on the electric field) behaves correctly.

B.4 Derivation of the distance r_{max}

The distance r_{max} between the tip of the ellipsoid and the position of the breakdown field E_k can be found from the relation $\rho_{ab}(r_{max}, \theta, \phi) = \rho_c$. Here, ρ_{ab} is the bisector in the direction of the electric field, and ρ_c is the distance (in terms of the ρ coordinate) to the position of the breakdown field $E(\rho_c) = E_k$. Thus, to solve for r_{max} , ρ_c needs to be found first, where ρ_c is defined by the equation $E(\rho_c) = E_k$ (the electric field is derived in Appendix B.3). However, due to the complicated nature of the electric field of a conducting ellipsoid, this equation cannot be solved explicitly for ρ_c . Nevertheless, it turns out that there is a fairly good approximation for r_{max} .

The surface of a conducting ellipsoid is an equipotential. One can mistakenly think that the electric field is constant on the surface. From symmetry it then follows that the points where the electric field has a certain constant value, such as E_k , will lie on an ellipsoid. Though this is based on a false assumption, it might prove useful to approximate the surface $E = E_k$ as forming an ellipsoid. Simulating the electric field in COMSOL, specifically for the semi-axes $a = 5$ cm and $b = 2$ cm, the field at the tip $E_0 = 95.2$ kV/cm and the breakdown field $E_k = 32$ kV/cm, results in the plot of Figure B.2. This figure shows that near the tip of the ellipsoid in the (x, z) -plane, where x is the horizontal coordinate and z the vertical coordinate, the line of $E = E_k$ approximately follows the shape of an ellipse around the conducting ellipse. The validity of the approximation can be tested, by importing the data points where $E = E_k$ into MATLAB, and fitting these using the equation of an ellipse. This ellipse has unknown semi-axes a' and b' , which are the fitting parameters, and is centered at the center of the conducting ellipsoid (here at $(0, 0)$) because of symmetry. The fitting equation is thus $z = a' \sqrt{1 - (x/b')^2}$. The data points imported from COMSOL and the fit through these points is depicted in Figure B.3, where $(x, z) = (0, 5)$ is the position of the tip of the ellipsoid. It follows that the data points indeed approximately lie on an ellipse near the tip of the conducting ellipsoid, as the fit agrees very well with the data points.

It can thus be concluded that the surface where $E = E_k$ can be approximated as an ellipsoid. Because of symmetry, only an ellipse in the (x, z) -plane or (y, z) -plane needs to be considered. The next step is to find an analytical expression for r_{max} going from the origin at $r = 0$ at the tip of the conducting ellipsoid to the ellipse where $E = E_k$.

While r_{max} cannot be found from the electric field for arbitrary θ , it can be found for $\theta = 0$ and $\theta = \pi/2$. First, the electric field is reformulated in terms of only r and θ . Then, filling in $\theta = 0$ and solving $E(r, 0) = \frac{b^2 E_0}{2ar + b^2 + r^2} = E_k$ for r gives:

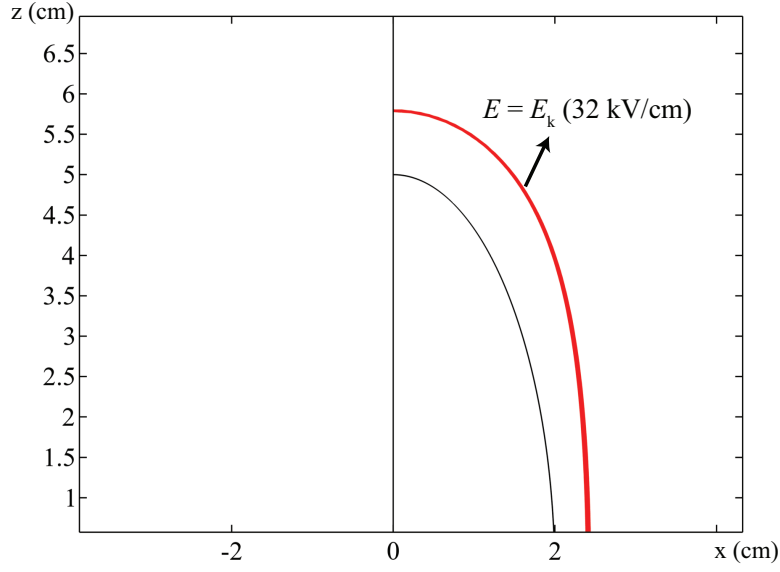


Figure B.2: The line of constant $E = E_k$ (red) for an ellipse with semi-axes $a = 5$ cm (vertical) and $b = 2$ cm (horizontal). Here only half of the width of the ellipse is shown and the axis of symmetry is drawn.

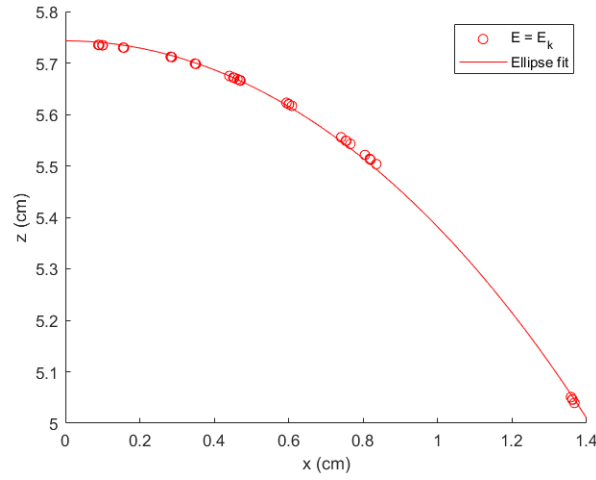


Figure B.3: Fit of $E = E_k$ data points using an ellipse fit of $z = a' \sqrt{1 - (x/b')^2}$. It is found that $a' = (5.743 \pm 0.002)$ cm $b' = (2.86 \pm 0.01)$ cm

$$r_{max}(\theta = 0) = \sqrt{a^2 + \frac{b^2(E_0 - E_k)}{E_k}} - a. \quad (\text{B.21})$$

Obtaining $r_{max}(\theta = \pi/2)$ proves more difficult. Filling in $\theta = \pi/2$ in the electric field expression yields:

$$E(r, \theta = \pi/2) = \frac{2b^2 E_0 \sqrt{\frac{(a^2+r^2)\left((b^2-a^2)\left(\frac{2a^2}{a^2+r^2}-1\right)+\sqrt{4a^2r^2+b^4-2b^2r^2+r^4+a^2+r^2}\right)}{\sqrt{4a^2r^2+b^4-2b^2r^2+r^4+2a^2-b^2+r^2}}}}{\sqrt[4]{4a^2r^2+b^4-2b^2r^2+r^4}\left(\sqrt{4a^2r^2+b^4-2b^2r^2+r^4}+b^2+r^2\right)}. \quad (\text{B.22})$$

Setting the above expression equal to E_k and solving for r leads to a case known as 'Casus irreducibilis'. For an irreducible degree 3 polynomial with three real roots, it has been proven that complex numbers need to be introduced to express the solution in roots of any degree, even though the solution is real [157]. Solving $E(r, \theta = \pi/2) = E_k$ for r , for example using software like Mathematica, leads to 6 solutions containing imaginary parts. Setting b close to a , it is found that one of these solutions approaches the solution of a sphere, accompanied by a very small imaginary part. For example, for $a = 3$ cm, $b = 2.99$ cm, $E_0 = 100$ kV/cm, $E_k = 32.75$ kV/cm a value of 10^{-12} cm is found for the imaginary part. These negligibly small imaginary contributions, which are found for any a and b and remain negligibly small, are a results of numerical noise in the machine number calculations in Mathematica (or other numerical software packages).

Possibly due to this 'Casus irreducibilis' issue, $r_{max}(\theta = \pi/2)$ has no solution at $a = b$, so for the reduction to a sphere. However, when b approaches a , $r_{max}(\theta = \pi/2)$ approaches the solution of a sphere. For example, taking again $a = 3$ cm, $b = 2.99$ cm, $E_0 = 100$ kV/cm, $E_k = 32.75$ kV/cm, the real part of $r_{max}(\theta = \pi/2)$ is 4.27758 cm, while the r_{max} of a sphere at $\theta = \pi/2$ is 4.29894 cm. Instead taking $b = 2.9999999$ cm (seven decimals) gives $r_{max}(\theta = \pi/2) = 4.29894$ cm for the ellipsoid. It can thus be concluded that $r_{max}(\theta = \pi/2)$ approaches the correct solution for a sphere and can be safely used, as the goal is to implement the model for an ellipsoid and not a sphere, for which simpler expressions are already known. Writing out the found solution for r_{max} at $\theta = \pi/2$ for a conducting ellipsoid gives:

$$r_{max}(\theta = \pi/2) = \frac{1}{2\sqrt{3}}\sqrt{\frac{F}{G}}, \quad (\text{B.23})$$

where F and G are given by:

$$\begin{aligned}
F = & 32 \sqrt[3]{2}(1-i\sqrt{3})a^8 E_k^4 + 12 \sqrt[3]{2}i(\sqrt{3}+i)a^2 b^6 E_k^2 (E_0^2 + 3E_k^2) \\
& + 24a^2 b^2 E_k^2 \left(\sqrt[3]{b^4 \left(3b^4 E_k \left(a^4 C_5 E_k - C_1 E_0^2 + 2C_1 E_k^2 \right) + 6a^4 E_k^3 (2a^4 C_7 E_k + C_1) - 18a^2 b^6 C_4 E_k^2 + 3a^2 b^2 C_1 E_k (E_0^2 - 4E_k^2) - b^8 C_3 \right) + C_2} \right. \\
& + 4 \sqrt[3]{2}i(\sqrt{3}+i)a^4 E_k^2) \\
& + b^4 \left(4 \left(E_0^2 - 2E_k^2 \right) \sqrt[3]{b^4 \left(12a^8 C_7 E_k^4 + 3a^4 b^4 C_5 E_k^2 - 18a^2 b^6 C_4 E_k^2 + 3a^2 C_1 C_6 E_k - b^8 C_3 - 3b^2 C_1 C_6 E_k \right) + C_2} + 2 \sqrt[3]{2}(1-i\sqrt{3})a^4 E_k^2 (4E_0^2 + 49E_k^2) \right) \\
& - 16a^4 E_k^2 \sqrt[3]{b^4 \left(12a^8 C_7 E_k^4 + 3a^4 b^4 C_5 E_k^2 - 18a^2 b^6 C_4 E_k^2 + 3a^2 C_1 C_6 E_k - b^8 C_3 - 3b^2 C_1 C_6 E_k \right) + C_2} \\
& + (1+i\sqrt{3})(256a^{12} E_k^6 - 1152a^{10} b^2 E_k^6 - 6b^6 (6a^6 E_k^4 (8E_0^2 + 49E_k^2) + C_1 C_6 E_k)) \\
& + 6a^4 b^8 C_5 E_k^2 - 36a^2 b^{10} C_4 E_k^2 + 6b^4 (4a^8 C_7 E_k^4 + a^2 C_1 C_6 E_k) - 2b^{12} C_3)^{2/3} + 2 \sqrt[3]{2}(1-i\sqrt{3})b^8 (E_0^2 + E_k^2)^2,
\end{aligned}$$

$$G = E_k^2 (a^2 - b^2) \sqrt[3]{b^4 (12a^8 C_7 E_k^4 + 3a^4 b^4 C_5 E_k^2 - 18a^2 b^6 C_4 E_k^2 + 3a^2 C_1 C_6 E_k - b^8 C_3 - 3b^2 C_1 C_6 E_k) + C_2},$$

and where $C_1, C_2, C_3, C_4, C_5, C_6$ and C_7 are defined as follows:

$$\begin{aligned}
C_1^2 = & -12a^8 E_k^4 (8E_0^2 + E_k^2) + 36a^6 b^2 E_k^4 (7E_0^2 + E_k^2) \\
& - 3a^4 b^4 E_k^2 (13E_0^4 + 72E_0^2 E_k^2 + 12E_k^4) \\
& + 6a^2 b^6 E_k^2 (7E_0^4 + 10E_0^2 E_k^2 + 2E_k^4) - 3b^8 E_0^4 (4E_0^2 + E_k^2),
\end{aligned}$$

$$C_2 = 128a^{12} E_k^6 - 576a^{10} b^2 E_k^6 - 18a^6 b^6 E_k^4 (8E_0^2 + 49E_k^2),$$

$$C_3 = 2E_0^6 - 21E_0^4 E_k^2 + 6E_0^2 E_k^4 + 2E_k^6,$$

$$C_4 = 2E_0^4 + 2E_0^2 E_k^2 + 3E_k^4,$$

$$C_5 = 5E_0^4 + 46E_0^2 E_k^2 + 122E_k^4,$$

$$C_6 = 2a^2 E_k^2 + b^2 (E_0^2 - 2E_k^2),$$

$$C_7 = 4E_0^2 + 85E_k^2.$$

Now that analytical expressions are found for $r_{max}(\theta = 0)$ and $r_{max}(\theta = \pi/2)$, the ellipse approximation for r_{max} at arbitrary θ can be applied. Noting that

the origin is placed at the tip of the ellipsoidal conductor, the equation for the ellipse where $E = E_k$ is given by:

$$\frac{(z' + a)^2}{a'^2} + \frac{x'^2}{b'^2} = 1, \quad (\text{B.24})$$

where (z', x') is a point on the ellipse $E = E_k$, a' is its major semi-axis and b' its minor semi-axis. This configuration is depicted in Figure B.4, where the grey region represents the photon absorption region. Here it is seen that $a' = a + r_{max}(\theta = 0)$, $z' = r_{max} \cos \theta$, and $x' = r_{max} \sin \theta$.

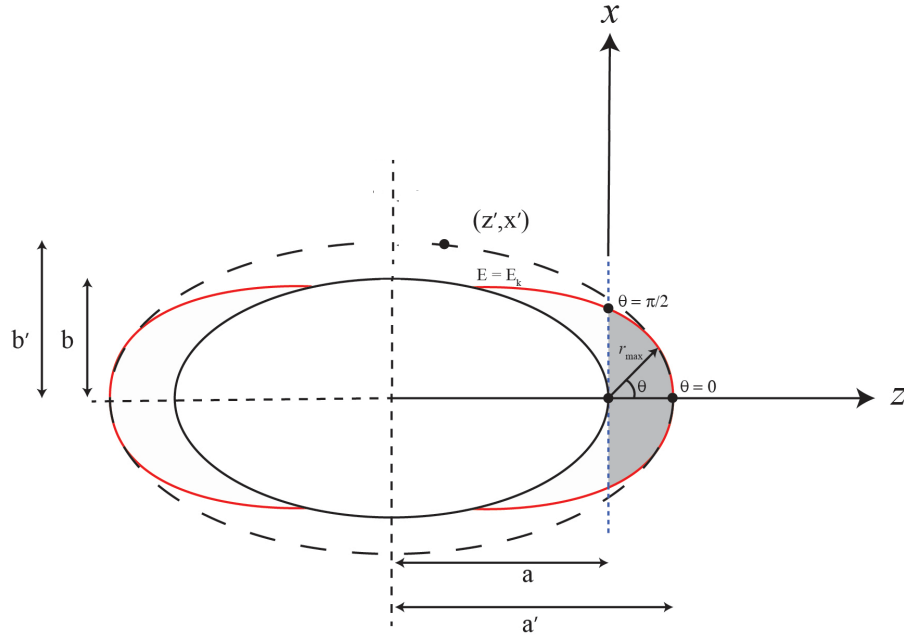


Figure B.4: The conducting ellipsoid (solid, black line), with positions of constant $E = E_k$ (solid, red line), the edge of the ionization region, approximated as an ellipse shape (dashed line) with coordinates (z', x') and semi-axes a' and b' .

Setting $z' = 0$ in equation (B.24), which corresponds to $x' = \pm r_{max}(\theta = \pi/2)$ as can be seen from Figure B.4, gives

$$\frac{a^2}{a'^2} + \frac{r_{max}(\theta = \pi/2)^2}{b'^2} = 1. \quad (\text{B.25})$$

which can be solved for the minor semi-axis b' of the ellipse $E = E_k$:

$$b' = \frac{r_{max}(\theta = \pi/2)}{\sqrt{1 - \frac{a^2}{a'^2}}}. \quad (\text{B.26})$$

Substituting the found expressions for a' , b' , z' and x' into equation (B.24) results in the final expression for $r_{max}(\theta)$ in the ellipse approximation:

$$r_{max}(\theta) = \frac{r_{max}(\theta=\pi/2) \left(\sqrt{r_{max}(\theta=0)^2 (2a+r_{max}(\theta=0))^2 \sin^2(\theta) + r_{max}(\theta=\pi/2)^2 (a+r_{max}(\theta=0))^2 \cos^2(\theta)} - ar_{max}(\theta=\pi/2) \cos(\theta) \right)}{r_{max}(\theta=0) (2a+r_{max}(\theta=0)) \sin^2(\theta) + r_{max}(\theta=\pi/2)^2 \cos^2(\theta)}. \quad (\text{B.27})$$

Looking back at Figure B.3, the ellipse fit of the data points gives $r_{max}(\theta = 0) = (5.743 - 5) \text{ cm} = 0.743 \text{ cm}$ in the z -direction, and $r_{max}(\theta = \pi/2) = 1.408 \text{ cm}$ in the x -direction. Equation (B.27) gives for the same input, $a = 5 \text{ cm}$, $b = 2 \text{ cm}$, $E_0 = 95.2 \text{ kV/cm}$ and $E_k = 32 \text{ kV/cm}$, the values of $r_{max}(\theta = 0) = 0.736 \text{ cm}$ and $r_{max}(\theta = \pi/2) = 1.397 \text{ cm}$. The discrepancy between these values is very small (relative error of about 1%) and caused by equation (B.27) being derived using the data points of $E = E_k$ at $\theta = 0$ and $\theta = \pi/2$ and basing the ellipse shape on that, while the ellipse in Figure B.3 is based on more data points. Hence, the ellipse of equation (B.27) is formulated such that the two computed r_{max} at $\theta = 0$ and $\theta = \pi/2$ lie on the ellipse, while for the fit the optimal fit does not necessarily go through these two points precisely. Equation (B.27) can also be compared to Figure B.3 for arbitrary $0 \leq \theta \leq \pi/2$. For example, $\theta = 0.9497 \text{ rad}$ gives $r_{max} = 0.928 \text{ cm}$ for the ellipse fit, and $r_{max} = 0.919 \text{ cm}$ for equation (B.27). Moreover, $\theta = 0.5120 \text{ rad}$ gives $r_{max} = 0.792 \text{ cm}$ and $r_{max} = 0.784 \text{ cm}$, respectively. We thus conclude that equation (B.27) is a fair approximation of the actual r_{max} of a conducting ellipsoid.

References

- [1] S. Nijdam, J. Teunissen, and U. Ebert, “The physics of streamer discharge phenomena,” en, *Plasma Sources Science and Technology*, vol. 29, no. 10, p. 103 001, Nov. 2020, Submitted to Plasma Sources Science and Technology, available at <https://arxiv.org/abs/2005.14588>. DOI: 10.1088/1361-6595/abaa05.
- [2] V. A. Rakov and M. A. Uman, *Lightning: physics and effects*. Cambridge university press, 2003. DOI: 10.1017/cbo9781107340886.
- [3] J. R. Dwyer and M. A. Uman, “The physics of lightning,” *Physics Reports*, vol. 534, no. 4, pp. 147–241, Jan. 2014. DOI: 10.1016/j.physrep.2013.09.004.
- [4] L. P. Babich, E. I. Bochkov, I. M. Kutsyk, T. Neubert, and O. Chanrion, “Positive streamer initiation from raindrops in thundercloud fields,” *Journal of Geophysical Research: Atmospheres*, vol. 121, no. 11, pp. 6393–6403, Jun. 2016. DOI: 10.1002/2016JD024901.
- [5] V. P. Pasko, “Recent advances in theory of transient luminous events,” *Journal of Geophysical Research: Space Physics*, vol. 115, no. A6, n/a–n/a, Jun. 2010. DOI: 10.1029/2009ja014860.
- [6] C. Ruf, N. O. Renno, J. F. Kok, E. Bandelier, M. J. Sander, S. Gross, L. Skjerve, and B. Cantor, “Emission of non-thermal microwave radiation by a martian dust storm,” *Geophysical research letters*, vol. 36, no. 13, Jul. 2009. DOI: 10.1029/2009g1038715.
- [7] C. T. Russell, T. L. Zhang, M. Delva, W. Magnes, R. J. Strangeway, and H. Y. Wei, “Lightning on venus inferred from whistler-mode waves in the ionosphere,” *Nature*, vol. 450, no. 7170, pp. 661–662, Nov. 2007. DOI: 10.1038/nature05930.
- [8] S. Rahamti, *The rainy tower*, 2021.
- [9] S. Hummel, *A red sprite*, 2020.
- [10] R. Gunn, “Electric field intensity inside of natural clouds,” *Journal of Applied Physics*, vol. 19, no. 5, pp. 481–484, May 1948. DOI: 10.1063/1.1698159.
- [11] E. R. Williams, “Large-scale charge separation in thunderclouds,” *Journal of Geophysical Research: Atmospheres*, vol. 90, no. D4, pp. 6013–6025, 1985. DOI: 10.1029/jd090id04p06013.
- [12] T. C. Marshall, M. Stolzenburg, and W. D. Rust, “Electric field measurements above mesoscale convective systems,” *Journal of Geophysical Research: Atmospheres*, vol. 101, no. D3, pp. 6979–6996, Mar. 1996. DOI: 10.1029/95jd03764.
- [13] M. Stolzenburg, T. C. Marshall, W. D. Rust, E. Bruning, D. R. MacGorman, and T. Hamlin, “Electric field values observed near lightning flash initiations,” *Geophysical Research Letters*, vol. 34, no. 4, Feb. 2007. DOI: <https://doi.org/10.1029/2006GL028777>.

- [14] S. A. Cummer, “Indirectly measured ambient electric fields for lightning initiation in fast breakdown regions,” *Geophysical Research Letters*, vol. 47, no. 4, e2019GL086089, Feb. 2020. DOI: 10.1029/2019g1086089.
- [15] A. Chilingarian, T. Karapetyan, M. Zazyan, G. Hovsepyan, B. Sargsyan, N. Nikolova, H. Angelov, J. Chum, and R. Langer, “Maximum strength of the atmospheric electric field,” *Physical Review D*, vol. 103, no. 4, p. 043021, Feb. 2021. DOI: 10.1103/physrevd.103.043021.
- [16] S. Sadighi, “Initiation of streamers from thundercloud hydrometeors and implications to lightning initiation,” 2015.
- [17] G. V. Naidis, “Conditions for inception of positive corona discharges in air,” *Journal of Physics D: Applied Physics*, vol. 38, no. 13, p. 2211, Jun. 2005. DOI: 10.1088/0022-3727/38/13/020.
- [18] N. Liu, J. R. Dwyer, and H. K. Rassoul, “Effects of pressure and humidity on positive corona inception from thundercloud hydrometeors,” *Journal of atmospheric and solar-terrestrial physics*, vol. 80, pp. 179–186, May 2012. DOI: 10.1016/j.jastp.2012.01.012.
- [19] J. M. Meek and J. D. Craggs, “Electrical breakdown of gases,” 1978.
- [20] C. Montijn and U. Ebert, “Diffusion correction to the raether–meek criterion for the avalanche-to-streamer transition,” *Journal of Physics D: Applied Physics*, vol. 39, no. 14, p. 2979, Jun. 2006. DOI: 10.1088/0022-3727/39/14/017.
- [21] A. A. Dubinova, *Modeling of streamer discharges near dielectrics*. TU Eindhoven, 2016.
- [22] R. Griffiths and C. Phelps, “A model for lightning initiation arising from positive corona streamer development,” *Journal of Geophysical Research*, vol. 81, no. 21, pp. 3671–3676, Jul. 1976. DOI: 10.1029/jc081i021p03671.
- [23] J. R. Dwyer, “A fundamental limit on electric fields in air,” *Geophysical Research Letters*, vol. 30, no. 20, Oct. 2003. DOI: 10.1029/2003g1017781.
- [24] G. Diniz, C. Rutjes, U. Ebert, and I. Ferreira, “Cold electron runaway below the friction curve,” *Journal of Geophysical Research: Atmospheres*, vol. 124, no. 1, pp. 189–198, 2019.
- [25] C. T. R. Wilson, “The electric field of a thundercloud and some of its effects,” *Proceedings of the Physical Society of London (1874-1925)*, vol. 37, no. 1, p. 32D, Jan. 1924. DOI: 10.1088/1478-7814/37/1/314.
- [26] A. Gurevich, G. Milikh, and R. Roussel-Dupre, “Runaway electron mechanism of air breakdown and preconditioning during a thunderstorm,” *Physics Letters A*, vol. 165, no. 5-6, pp. 463–468, Jun. 1992. DOI: 10.1016/0375-9601(92)90348-p.
- [27] J. R. Dwyer, “The initiation of lightning by runaway air breakdown,” *Geophysical research letters*, vol. 32, no. 20, 2005. DOI: 10.1029/2005g1023975.
- [28] D. Petersen, M. Bailey, W. H. Beasley, and J. Hallett, “A brief review of the problem of lightning initiation and a hypothesis of initial lightning leader formation,” *Journal of Geophysical Research: Atmospheres*, vol. 113, no. D17, Sep. 2008. DOI: <https://doi.org/10.1029/2007JD009036>.

- [29] P. O. Kochkin, C. V. Nguyen, A. P. J. van Deursen, and U. Ebert, “Experimental study of hard x-rays emitted from metre-scale positive discharges in air,” *Journal of Physics D: Applied Physics*, vol. 45, no. 42, p. 425 202, Oct. 2012. DOI: 10.1088/0022-3727/45/42/425202.
- [30] J. R. Dwyer, “The relativistic feedback discharge model of terrestrial gamma ray flashes,” *Journal of Geophysical Research: Space Physics*, vol. 117, no. A2, n/a–n/a, Feb. 2012. DOI: 10.1029/2011ja017160.
- [31] E. R. Williams, “The electrification of thunderstorms,” *Scientific American*, vol. 259, no. 5, pp. 88–99, Nov. 1988. DOI: 10.1038/scientificamerican1188-88.
- [32] L. B. Loeb, “The mechanisms of stepped and dart leaders in cloud-to-ground lightning strokes,” *Journal of Geophysical Research (1896-1977)*, vol. 71, no. 20, pp. 4711–4721, Oct. 1966. DOI: <https://doi.org/10.1029/JZ071i020p04711>.
- [33] J. A. Crabb and J. Latham, “Corona from colliding drops as a possible mechanism for the triggering of lightning,” *Quarterly Journal of the Royal Meteorological Society*, vol. 100, no. 424, pp. 191–202, Apr. 1974. DOI: <https://doi.org/10.1002/qj.49710042406>.
- [34] R. Griffiths, “The initiation of corona discharges from charged ice particles in a strong electric field,” *Journal of Electrostatics*, vol. 1, no. 1, pp. 3–13, Feb. 1975. DOI: 10.1016/0304-3886(75)90003-0.
- [35] D. E. Proctor, “Regions where lightning flashes began,” *Journal of Geophysical Research: Atmospheres*, vol. 96, no. D3, pp. 5099–5112, 1991. DOI: 10.1029/90jd02120.
- [36] D. Petersen, M. Bailey, J. Hallett, and W. H. Beasley, “Laboratory investigation of positive streamer discharges from simulated ice hydrometeors,” *Quarterly Journal of the Royal Meteorological Society*, vol. 132, no. 615, pp. 263–273, Jan. 2006. DOI: <https://doi.org/10.1256/qj.05.32>.
- [37] W. Rison, P. R. Krehbiel, M. G. Stock, H. E. Edens, X.-M. Shao, R. J. Thomas, M. A. Stanley, and Y. Zhang, “Observations of narrow bipolar events reveal how lightning is initiated in thunderstorms,” *Nature communications*, vol. 7, no. 1, p. 10 721, Feb. 2016, ISSN: 2041-1723. DOI: 10.1038/ncomms10721.
- [38] T. Marshall, S. Bandara, N. Karunarathne, S. Karunarathne, I. Kolmasova, R. Siedlecki, and M. Stolzenburg, “A study of lightning flash initiation prior to the first initial breakdown pulse,” *Atmospheric Research*, vol. 217, pp. 10–23, Mar. 2019. DOI: 10.1016/j.atmosres.2018.10.013.
- [39] A. Y. Kostinskiy, T. C. Marshall, and S. Maribeth, “The mechanism of the origin and development of lightning from initiating event to initial breakdown pulses (v. 2),” *Journal of Geophysical Research: Atmospheres*, vol. 125, no. 22, e2020JD033191, Jun. 2020. DOI: 10.1002/essoar.10503265.1.
- [40] D. Petersen, M. Bailey, J. Hallett, and W. Beasley, “Laboratory investigation of corona initiation by ice crystals and its importance to lightning,” *Quarterly Journal of the Royal Meteorological Society*, vol. 141, no. 689, pp. 1283–1293, Oct. 2015. DOI: <https://doi.org/10.1002/qj.2436>.

- [41] V. Mazur, C. D. Taylor, and D. A. Petersen, "Simulating electrodeless discharge from a hydrometeor array," *Journal of Geophysical Research: Atmospheres*, vol. 120, no. 20, pp. 10–879, Oct. 2015. DOI: 10.1002/2015jd023466.
- [42] A. G. Temnikov, L. L. Chernensky, A. V. Orlov, N. Y. Lysov, O. S. Belova, D. S. Zhuravkova, and T. K. Kivshar, "Artificial initiation of lightning in thunderclouds by model hydrometeor groups," *Russian Electrical Engineering*, vol. 89, no. 8, pp. 484–489, Aug. 2018. DOI: 10.3103/s1068371218080096.
- [43] D. Petersen, *The problem of lightning initiation*.
- [44] C. Rutjes, "Modeling high energy atmospheric physics and lightning inception," English, Proefschrift, Ph.D. dissertation, Department of Applied Physics, Mar. 2018, ISBN: 978-94-028-0965-7.
- [45] J. J. Lowke, "The initiation of lightning in thunderclouds: The possible influence of metastable nitrogen and oxygen molecules in initiating lightning streamers," *Journal of Geophysical Research: Atmospheres*, vol. 120, no. 8, pp. 3183–3190, Apr. 2015. DOI: 10.1002/2014jd022223.
- [46] R. Morrow and J. J. Lowke, "Streamer propagation in air," *Journal of Physics D: Applied Physics*, vol. 30, no. 4, p. 614, Feb. 1997. DOI: 10.1088/0022-3727/30/4/017.
- [47] H. Akiyama, "Streamer discharges in liquids and their applications," *IEEE Transactions on Dielectrics and Electrical Insulation*, vol. 7, no. 5, pp. 646–653, 2000. DOI: 10.1109/94.879360.
- [48] E. M. van Veldhuizen and W. R. Rutgers, "Pulsed positive corona streamer propagation and branching," *Journal of Physics D: Applied Physics*, vol. 35, no. 17, p. 2169, Aug. 2002. DOI: 10.1088/0022-3727/35/17/313.
- [49] U. Ebert, S. Nijdam, C. Li, A. Luque, T. Briels, and E. van Veldhuizen, "Review of recent results on streamer discharges and discussion of their relevance for sprites and lightning," *Journal of Geophysical Research: Space Physics*, vol. 115, no. A7, Jul. 2010. DOI: 10.1029/2009ja014867.
- [50] S. Nijdam, F. M. J. H. van de Wetering, R. Blanc, E. M. van Veldhuizen, and U. Ebert, "Probing photo-ionization: Experiments on positive streamers in pure gases and mixtures," *Journal of Physics D: Applied Physics*, vol. 43, no. 14, p. 145 204, Mar. 2010, ISSN: 1361-6463. DOI: 10.1088/0022-3727/43/14/145204.
- [51] Z. Bonaventura, A. Bourdon, S. Celestin, and V. P. Pasko, "Electric field determination in streamer discharges in air at atmospheric pressure," *Plasma Sources Science and Technology*, vol. 20, no. 3, p. 035 012, Apr. 2011, ISSN: 1361-6595. DOI: 10.1088/0963-0252/20/3/035012.
- [52] A. Shashurin, M. N. Shneider, and M. Keidar, "Measurements of streamer head potential and conductivity of streamer column in cold nonequilibrium atmospheric plasmas," *Plasma Sources Science and Technology*, vol. 21, no. 3, p. 034 006, Apr. 2012, ISSN: 1361-6595. DOI: 10.1088/0963-0252/21/3/034006.
- [53] S. Nijdam, J. Teunissen, E. Takahashi, and U. Ebert, "The role of free electrons in the guiding of positive streamers," *Plasma Sources Science and Technology*, vol. 25, no. 4, p. 044 001, Apr. 2016, ISSN: 1361-6595. DOI: 10.1088/0963-0252/25/4/044001.

- [54] D. Okano, “Time-lag properties of corona streamer discharges between impulse sphere and dc needle electrodes under atmospheric air conditions,” *Review of Scientific Instruments*, vol. 84, no. 2, p. 024 702, Feb. 2013. DOI: 10.1063/1.4791587.
- [55] Z. Wang and Y. Geng, “Study on the streamer inception characteristics under positive lightning impulse voltage,” *AIP Advances*, vol. 7, no. 11, p. 115 115, Nov. 2017. DOI: 10.1063/1.5011753.
- [56] E. M. van Veldhuizen and W. R. Rutgers, “Inception behaviour of pulsed positive corona in several gases,” *Journal of Physics D: Applied Physics*, vol. 36, no. 21, p. 2692, Oct. 2003. DOI: 10.1088/0022-3727/36/21/015.
- [57] T. Briels, E. van Veldhuizen, and U. Ebert, “Time Resolved Measurements of Streamer Inception in Air,” en, *IEEE Trans. Plasma Sci.*, vol. 36, no. 4, pp. 908–909, Aug. 2008. DOI: 10.1109/TPS.2008.920223.
- [58] J. M. Meek, “A theory of spark discharge,” *Phys. Rev.*, vol. 57, no. 8, pp. 722–728, 8 Apr. 1940. DOI: 10.1103/PhysRev.57.722.
- [59] A. Dubinova, C. Rutjes, U. Ebert, S. Buitink, O. Scholten, and G. T. N. Trinh, “Prediction of lightning inception by large ice particles and extensive air showers,” *Phys. Rev. Lett.*, vol. 115, no. 1, p. 015 002, 1 Jun. 2015. DOI: 10.1103/PhysRevLett.115.015002.
- [60] E. E. Kunhardt and Y. Tzeng, “Development of an electron avalanche and its transition into streamers,” *Physical Review A*, vol. 38, no. 3, p. 1410, Aug. 1988. DOI: 10.1103/physreva.38.1410.
- [61] S. Pancheshnyi, “Effective ionization rate in nitrogen–oxygen mixtures,” *Journal of Physics D: Applied Physics*, vol. 46, no. 15, p. 155 201, Mar. 2013. DOI: 10.1088/0022-3727/46/15/155201.
- [62] J. J. Lowke, “Theory of electrical breakdown in air—the role of metastable oxygen molecules,” *Journal of Physics D: Applied Physics*, vol. 25, no. 2, p. 202, Feb. 1992. DOI: 10.1088/0022-3727/25/2/012.
- [63] Y. Li, E. M. van Veldhuizen, G. J. Zhang, U. Ebert, and S. Nijdam, “Positive double-pulse streamers: How pulse-to-pulse delay influences initiation and propagation of subsequent discharges,” *Plasma Sources Science and Technology*, vol. 27, no. 12, p. 125 003, Dec. 2018. DOI: 10.1088/1361-6595/aaf2c6.
- [64] T. Fengbo, Z. Qiaogen, G. Bo, W. Hu, and L. Zhou, “A repetitive nanosecond pulse source for generation of large volume streamer discharge,” *Plasma Science and Technology*, vol. 10, no. 5, p. 588, Oct. 2008. DOI: 10.1088/1009-0630/10/5/13.
- [65] Z. Zhao and J. T. Li, “Integrated effect on evolution of streamer dynamics under long-term repetitive sub-microsecond pulses in high-pressure nitrogen,” *Plasma Sources Science and Technology*, vol. 28, no. 11, p. 115 019, Dec. 2019. DOI: 10.1088/1361-6595/ab556a.
- [66] J. Teunissen and U. Ebert, “3d PIC-MCC simulations of discharge inception around a sharp anode in nitrogen/oxygen mixtures,” en, *Plasma Sources Sci. Technol.*, vol. 25, no. 4, p. 044 005, Aug. 2016. DOI: 10.1088/0963-0252/25/4/044005.

- [67] J. Cross and J. Beattie, “Positive glow corona in quasi-uniform fields,” *Canadian Electrical Engineering Journal*, vol. 5, no. 3, pp. 22–32, Jul. 1980. DOI: 10.1109/ceej.1980.6591736.
- [68] T. Giao and J. Jordan, “Modes of corona discharges in air,” *IEEE Transactions on Power Apparatus and Systems*, vol. PAS-87, no. 5, pp. 1207–1215, May 1968. DOI: 10.1109/tpas.1968.292211.
- [69] S. Pancheshnyi, “Role of electronegative gas admixtures in streamer start, propagation and branching phenomena,” en, *Plasma Sources Sci. Technol.*, vol. 14, no. 4, pp. 645–653, Aug. 2005, Publisher: IOP Publishing, ISSN: 0963-0252. DOI: 10.1088/0963-0252/14/4/002.
- [70] G. Wormeester, S. Pancheshnyi, A. Luque, S. Nijdam, and U. Ebert, “Probing photo-ionization: Simulations of positive streamers in varying N₂:O₂-mixtures,” *J. Phys. D: Appl. Phys.*, vol. 43, no. 50, p. 505201, Dec. 2010, ISSN: 1361-6463. DOI: 10.1088/0022-3727/43/50/505201.
- [71] N. A. Popov, “Evolution of the negative ion composition in the afterglow of a streamer discharge in air,” en, *Plasma Phys. Rep.*, vol. 36, no. 9, pp. 812–818, Sep. 2010, ISSN: 1063-780X, 1562-6938. DOI: 10.1134/S1063780X10090084.
- [72] *Itikawa database, www.lxcat.net, retrieved on may 14, 2020.*
- [73] Y. Itikawa, “Cross Sections for Electron Collisions with Nitrogen Molecules,” *Journal of Physical and Chemical Reference Data*, vol. 35, no. 1, pp. 31–53, Dec. 2005, Publisher: American Institute of Physics, ISSN: 0047-2689. DOI: 10.1063/1.1937426.
- [74] —, “Cross Sections for Electron Collisions with Oxygen Molecules,” *Journal of Physical and Chemical Reference Data*, vol. 38, no. 1, pp. 1–20, Dec. 2008, Publisher: American Institute of Physics, ISSN: 0047-2689. DOI: 10.1063/1.3025886.
- [75] *Phelps database, www.lxcat.net, retrieved on may 14, 2020.*
- [76] I. A. Kossyi, A. Y. Kostinsky, A. A. Matveyev, and V. P. Silakov, “Kinetic scheme of the non-equilibrium discharge in nitrogen-oxygen mixtures,” *Plasma Sources Sci. Technol.*, vol. 1, no. 3, pp. 207–220, Aug. 1992, ISSN: 0963-0252, 1361-6595. DOI: 10.1088/0963-0252/1/3/011.
- [77] M. B. Zheleznyak and A. K. Mnatsakanyan, “Photoionization of nitrogen and oxygen mixtures by radiation from a gas discharge,” *Teplofizika Vysokikh Temperatur*, vol. 20, no. 3, pp. 423–428, 1982.
- [78] O. Chanrion and T. Neubert, “A pic-mcc code for simulation of streamer propagation in air,” English, *Journal of Computational Physics*, vol. 15, no. 15, pp. 7222–7245, Jul. 2008, ISSN: 0021-9991. DOI: 10.1016/j.jcp.2008.04.016.
- [79] *VIEHLAND database, www.lxcat.net, retrieved on november 18, 2019.*
- [80] *COMSOL Multiphysics® v. 5.4, www.comsol.com. COMSOL AB, stockholm, sweden.*
- [81] C. Rutjes, “Modeling high energy atmospheric physics and lightning inception,” English, Proefschrift, Ph.D. dissertation, Department of Applied Physics, Mar. 2018, ISBN: 978-94-028-0965-7.

- [82] G. J. M. Hagelaar and L. C. Pitchford, “Solving the Boltzmann equation to obtain electron transport coefficients and rate coefficients for fluid models,” en, *Plasma Sources Sci. Technol.*, vol. 14, no. 4, pp. 722–733, Oct. 2005, ISSN: 0963-0252. DOI: 10.1088/0963-0252/14/4/011.
- [83] *Bolsig- solver ver. linux 03/2016*, <http://www.bolsig.laplace.univ-tlse.fr/>.
- [84] V. Guerra and J. Loureiro, “Electron and heavy particle kinetics in a low-pressure nitrogen glow discharge,” *Plasma Sources Sci. Technol.*, vol. 6, no. 3, pp. 361–372, Aug. 1997. DOI: 10.1088/0963-0252/6/3/013.
- [85] M. Capitelli, C. M. Ferreira, B. F. Gordiets, and A. I. Osipov, *Plasma Kinetics in Atmospheric Gases*, en, ser. Springer Series on Atomic, Optical, and Plasma Physics. Berlin Heidelberg: Springer-Verlag, 2000, ISBN: 978-3-540-67416-0. DOI: 10.1007/978-3-662-04158-1.
- [86] L. J. Varnerin, “Neutralization of ions and ionization of atoms near metal surfaces,” *Phys. Rev.*, vol. 91, no. 4, pp. 859–863, 4 Aug. 1953. DOI: 10.1103/PhysRev.91.859.
- [87] U. Ebert and D. D. Sentman, “Streamers, sprites, leaders, lightning: From micro-to macroscales,” *Journal of Physics D: Applied Physics*, vol. 41, no. 23, p. 230 301, Nov. 2008. DOI: 10.1088/0022-3727/41/23/230301.
- [88] U. Ebert, C. Montijn, T. M. P. Briels, W. Hundsdorfer, B. Meulenbroek, A. Rocco, and E. M. van Veldhuizen, “The multiscale nature of streamers,” *Plasma Sources Science and Technology*, vol. 15, no. 2, S118, Apr. 2006. DOI: 10.1088/0963-0252/15/2/S14.
- [89] S. H. Nam, H. Rahaman, H. Heo, S. S. Park, J. W. Shin, J. H. So, and W. Jang, “Empirical analysis of high pressure sf 6 gas breakdown strength in a spark gap switch,” *IEEE Transactions on Dielectrics and Electrical Insulation*, vol. 16, no. 4, pp. 1106–1110, Aug. 2009. DOI: 10.1109/tdei.2009.5211862.
- [90] J. F. Kolb, R. P. Joshi, S. Xiao, and K. H. Schoenbach, “Streamers in water and other dielectric liquids,” *Journal of Physics D: Applied Physics*, vol. 41, no. 23, p. 234 007, Nov. 2008. DOI: 10.1088/0022-3727/41/23/234007.
- [91] A. Sun, C. Huo, and J. Zhuang, “Formation mechanism of streamer discharges in liquids: A review,” *High Voltage*, vol. 1, no. 2, pp. 74–80, Jul. 2016. DOI: 10.1049/hve.2016.0016.
- [92] M. Seeger, R. Smeets, J. Yan, H. Ito, M. Claessens, E. Dullni, L. Falkingham, C. M. Franck, F. Gentils, W. Hartmann, Y. Kieffel, S. Jia, G. Jones, J. Mantilla, S. Pawar, M. Rabie, P. Robin-Jouan, H. Schellekens, J. Spencer, T. Uchii, X. Li, and S. Yanabu, “Recent trends in development of high voltage circuit breakers with sf6 alternative gases,” *Plasma Physics and Technology*, vol. 4, no. 1, pp. 8–12, 2017. DOI: 10.14311/ppt.2017.1.8.
- [93] Y. Kieffel, F. Biquez, P. Ponchon, and T. Irwin, “Sf 6 alternative development for high voltage switchgears,” in *2015 IEEE power & energy society general meeting*, IEEE, 2015, pp. 1–5.
- [94] O. Melnik and M. Parrot, “Electrostatic discharge in martian dust storms,” *Journal of Geophysical Research: Space Physics*, vol. 103, no. A12, pp. 29 107–29 117, Dec. 1998. DOI: 10.1029/98ja01954.

- [95] S. Mirpour, A. Martinez, J. Teunissen, U. Ebert, and S. Nijdam, "Distribution of inception times in repetitive pulsed discharges in synthetic air," *Plasma Sources Science and Technology*, vol. 29, no. 11, p. 115 010, Nov. 2020. DOI: 10.1088/1361-6595/abb614.
- [96] A. Pedersen, T. Christen, A. Blaszczyk, and H. Boehme, "Streamer inception and propagation models for designing air insulated power devices," in *2009 IEEE Conference on Electrical Insulation and Dielectric Phenomena*, IEEE, IEEE, Aug. 2009, pp. 604–607. DOI: 10.1109/ceidp.2009.5377740.
- [97] B. Bagheri, J. Teunissen, and U. Ebert, "Simulation of positive streamers in co2 and in air: The role of photoionization or other electron sources," *Plasma Sources Science and Technology*, vol. 29, no. 12, p. 125 021, Dec. 2020. DOI: 10.1088/1361-6595/abc93e.
- [98] M. Seeger, J. Avaheden, S. Pancheshnyi, and T. Votteler, "Streamer parameters and breakdown in co2," *Journal of Physics D: Applied Physics*, vol. 50, no. 1, p. 015 207, Nov. 2016. DOI: 10.1088/1361-6463/50/1/015207.
- [99] W. Wang and A. Bogaerts, "Effective ionisation coefficients and critical breakdown electric field of co2 at elevated temperature: Effect of excited states and ion kinetics," *Plasma Sources Science and Technology*, vol. 25, no. 5, p. 055 025, Sep. 2016. DOI: 10.1088/0963-0252/25/5/055025.
- [100] H. Hokazono and H. Fujimoto, "Theoretical analysis of the co2 molecule decomposition and contaminants yield in transversely excited atmospheric co2 laser discharge," *Journal of applied physics*, vol. 62, no. 5, pp. 1585–1594, Sep. 1987. DOI: 10.1063/1.339606.
- [101] P. Haefliger and C. M. Franck, "Detailed precision and accuracy analysis of swarm parameters from a pulsed townsend experiment," *Review of Scientific instruments*, vol. 89, no. 2, p. 023 114, Feb. 2018. DOI: 10.1063/1.5002762.
- [102] L. A. Viehland and C. C. Kirkpatrick, "Relating ion/neutral reaction rate coefficients and cross-sections by accessing a database for ion transport properties," *International journal of mass spectrometry and ion processes*, vol. 149, pp. 555–571, Nov. 1995. DOI: 10.1016/0168-1176(95)04288-v.
- [103] M. McFarland, D. L. Albritton, F. C. Fehsenfeld, E. E. Ferguson, and A. L. Schmeltekopf, "Flow-drift technique for ion mobility and ion-molecule reaction rate constant measurements. iii. negative ion reactions of o- with co, no, h2, and d2," *The Journal of Chemical Physics*, vol. 59, no. 12, pp. 6629–6635, Dec. 1973. DOI: 10.1063/1.1680043.
- [104] R. Aerts, W. Somers, and A. Bogaerts, "Carbon dioxide splitting in a dielectric barrier discharge plasma: A combined experimental and computational study," *ChemSusChem*, vol. 8, no. 4, pp. 702–716, Jan. 2015. DOI: 10.1002/cssc.201402818.
- [105] V. Mazur, *Principles of Lightning Physics*, ser. 2053-2563. IOP Publishing, 2016, ISBN: 978-0-7503-1152-6. DOI: 10.1088/978-0-7503-1152-6.

- [106] M. Stolzenburg and T. C. Marshall, “Electric field and charge structure in lightning-producing clouds,” in *Lightning: Principles, Instruments and Applications: Review of Modern Lightning Research*, H. D. Betz, U. Schumann, and P. Laroche, Eds. Dordrecht: Springer Netherlands, 2009, pp. 57–82, ISBN: 978-1-4020-9079-0. DOI: 10.1007/978-1-4020-9079-0_3.
- [107] T. C. Marshall, M. P. McCarthy, and W. D. Rust, “Electric field magnitudes and lightning initiation in thunderstorms,” *Journal of Geophysical Research: Atmospheres*, vol. 100, no. D4, pp. 7097–7103, 1995. DOI: <https://doi.org/10.1029/95JD00020>.
- [108] S. Coquillat, S. Chauzy, and J.-C. Médale, “Microdischarges between ice particles,” *Journal of Geophysical Research: Atmospheres*, vol. 100, no. D7, pp. 14327–14334, 1995. DOI: <https://doi.org/10.1029/95JD00986>.
- [109] R. F. Griffiths and J. Latham, “Electrical corona from ice hydrometeors,” *Quarterly Journal of the Royal Meteorological Society*, vol. 100, no. 424, pp. 163–180, Apr. 1974. DOI: <https://doi.org/10.1002/qj.49710042404>.
- [110] Y. P. Raizer, *Gas discharge physics. Fizika gazovogo razryada*. Berlin: Springer, 1991, Translated from Russian by Vitaly I Kisin.
- [111] N. Liu, J. R. Dwyer, and H. K. Rassoul, “Effects of pressure and humidity on positive corona inception from thundercloud hydrometeors,” *Journal of Atmospheric and Solar-Terrestrial Physics*, vol. 80, pp. 179–186, 2012, ISSN: 1364-6826. DOI: <https://doi.org/10.1016/j.jastp.2012.01.012>.
- [112] G. V. Naidis, “Conditions for inception of positive corona discharges in air,” *Journal of Physics D: Applied Physics*, vol. 38, no. 13, pp. 2211–2214, Jun. 2005. DOI: 10.1088/0022-3727/38/13/020.
- [113] C. T. Phelps and R. F. Griffiths, “Dependence of positive corona streamer propagation on air pressure and water vapor content,” *Journal of Applied Physics*, vol. 47, no. 7, pp. 2929–2934, Jul. 1976. DOI: 10.1063/1.323084.
- [114] C. Phelps, “Positive streamer system intensification and its possible role in lightning initiation,” *Journal of Atmospheric and Terrestrial Physics*, vol. 36, no. 1, pp. 103–111, 1974, ISSN: 0021-9169. DOI: [https://doi.org/10.1016/0021-9169\(74\)90070-1](https://doi.org/10.1016/0021-9169(74)90070-1).
- [115] F. D’Alessandro and G. Berger, “Laboratory studies of corona emissions from air terminals,” *Journal of Physics D: Applied Physics*, vol. 32, no. 21, pp. 2785–2790, Sep. 1999. DOI: 10.1088/0022-3727/32/21/311.
- [116] R. T. Waters and W. B. Stark, “Characteristics of the stabilized glow discharge in air,” *Journal of Physics D: Applied Physics*, vol. 8, no. 4, pp. 416–426, Mar. 1975. DOI: 10.1088/0022-3727/8/4/014.
- [117] E. Nasser and M. Heiszler, “Mathematical-physical model of the streamer in nonuniform fields,” *Journal of Applied Physics*, vol. 45, no. 8, pp. 3396–3401, Aug. 1974. DOI: 10.1063/1.1663791.
- [118] W. O. Schumann, “ber das minimum der durchbruchfeldstärke bei kugelelektroden,” *Archiv f. Elektrotechnik*, vol. 12, no. 6-12, pp. 593–608, 12 Apr. 1923. DOI: 10.1007/bf01656766.

- [119] A. F. Kip, “Positive-point-to-plane discharge in air at atmospheric pressure,” *Phys. Rev.*, vol. 54, no. 2, pp. 139–146, 2 Jul. 1938. DOI: [10.1103/PhysRev.54.139](https://doi.org/10.1103/PhysRev.54.139).
- [120] H. W. Bandel, “Point-to-plane corona in dry air,” *Phys. Rev.*, vol. 84, no. 1, pp. 92–99, 1 Oct. 1951. DOI: [10.1103/PhysRev.84.92](https://doi.org/10.1103/PhysRev.84.92).
- [121] J. A. Riouset, A. Nag, and C. Palotai, “Scaling of conventional breakdown threshold: Impact for predictions of lightning and tles on earth, venus, and mars,” *Icarus*, vol. 338, p. 113 506, 2020, ISSN: 0019-1035. DOI: <https://doi.org/10.1016/j.icarus.2019.113506>.
- [122] R. Griffiths, “The initiation of corona discharges from charged ice particles in a strong electric field,” *Journal of Electrostatics*, vol. 1, no. 1, pp. 3–13, 1975, ISSN: 0304-3886. DOI: [https://doi.org/10.1016/0304-3886\(75\)90003-0](https://doi.org/10.1016/0304-3886(75)90003-0).
- [123] L. Babich, E. Bochkov, and T. Neubert, “The role of charged ice hydrometeors in lightning initiation,” *Journal of Atmospheric and Solar-Terrestrial Physics*, vol. 154, pp. 43–46, 2017, ISSN: 1364-6826. DOI: <https://doi.org/10.1016/j.jastp.2016.12.010>.
- [124] T. C. Marshall and W. P. Winn, “Measurements of charged precipitation in a new mexico thunderstorm: Lower positive charge centers,” *Journal of Geophysical Research: Oceans*, vol. 87, no. C9, pp. 7141–7157, 1982. DOI: <https://doi.org/10.1029/JC087iC09p07141>.
- [125] D. R. MacGorman, *The Electrical Nature of Storms*. New York: Oxford University Press, 1998, ISBN: 9780195073379. DOI: [10.1063/1.882670](https://doi.org/10.1063/1.882670).
- [126] A. J. Weinheimer, J. E. Dye, D. W. Breed, M. P. Spowart, J. L. Parrish, T. L. Hoglin, and T. C. Marshall, “Simultaneous measurements of the charge, size, and shape of hydrometeors in an electrified cloud,” *Journal of Geophysical Research: Atmospheres*, vol. 96, no. D11, pp. 20 809–20 829, 1991. DOI: <https://doi.org/10.1029/91JD02262>.
- [127] B. Gardiner, D. Lamb, R. L. Pitter, J. Hallett, and C. P. R. Saunders, “Measurements of initial potential gradient and particle charges in a montana summer thunderstorm,” *Journal of Geophysical Research: Atmospheres*, vol. 90, no. D4, pp. 6079–6086, 1985. DOI: <https://doi.org/10.1029/JD090iD04p06079>.
- [128] C. Köhn and U. Ebert, “Calculation of beams of positrons, neutrons, and protons associated with terrestrial gamma ray flashes,” *Journal of Geophysical Research: Atmospheres*, vol. 120, no. 4, pp. 1620–1635, Feb. 2015. DOI: <https://doi.org/10.1002/2014JD022229>.
- [129] M. B. Zhelezniak, A. K. Mnatsakanian, and S. V. Sizykh, “Photoionization of nitrogen and oxygen mixtures by radiation from a gas discharge,” *High Temperature Science*, vol. 20, no. 3, pp. 357–362, Nov. 1982.
- [130] T. L. Curtright, Z. Cao, S. Huang, J. S. Sarmiento, S. Subedi, D. A. Tarrence, and T. R. Thapaliya, “Charge densities for conducting ellipsoids,” *European Journal of Physics*, vol. 41, no. 3, p. 035 204, Apr. 2020. DOI: [10.1088/1361-6404/ab806a](https://doi.org/10.1088/1361-6404/ab806a).

- [131] C. Rutjes, U. Ebert, S. Buitink, O. Scholten, and T. N. G. Trinh, “Generation of seed electrons by extensive air showers, and the lightning inception problem including narrow bipolar events,” *Journal of Geophysical Research: Atmospheres*, vol. 124, no. 13, pp. 7255–7269, Jul. 2019. DOI: 10.1029/2018JD029040.
- [132] A. Dubinova, “Modeling of streamer discharges near dielectrics,” English, Proefschrift, Ph.D. dissertation, Department of Applied Physics, Sep. 2016, ISBN: 978-90-386-4128-7.
- [133] V. Mazur, “Lightning initiation—the most difficult issue of lightning physics,” *Principles of Lightning Physics*, 2016. DOI: 10.1088/978-0-7503-1152-6ch12.
- [134] S. Sadighi, N. Liu, J. R. Dwyer, and H. K. Rassoul, “Streamer formation and branching from model hydrometeors in subbreakdown conditions inside thunderclouds,” *Journal of Geophysical Research: Atmospheres*, vol. 120, no. 9, pp. 3660–3678, May 2015. DOI: 10.1002/2014jd022724.
- [135] X. Gao, N. Liu, F. Shi, and H. K. Rassoul, “Streamer discharge initiation from an isolated spherical hydrometeor at subbreakdown condition,” *Journal of Electrostatics*, vol. 106, p. 103457, Jul. 2020. DOI: 10.1016/j.elstat.2020.103457.
- [136] J. Wu, X. Gao, Y. Ma, and N. Liu, “Streamer initiation from column hydrometeor at weak ambient electric field,” *Plasma Research Express*, vol. 1, no. 3, p. 035009, Aug. 2019. DOI: 10.1088/2516-1067/ab37cd.
- [137] A. Mavrovic, A. Roy, A. Royer, B. Filali, F. Boone, C. Pappas, and O. Sonnentag, “Dielectric characterization of vegetation at l band using an open-ended coaxial probe,” *Geoscientific Instrumentation, Methods and Data Systems*, vol. 7, no. 3, pp. 195–208, Jul. 2018. DOI: 10.5194/gi-7-195-2018.
- [138] A. Luque, V. Ratushnaya, and U. Ebert, “Positive and negative streamers in ambient air: Modelling evolution and velocities,” *Journal of Physics D: Applied Physics*, vol. 41, no. 23, p. 234005, Nov. 2008. DOI: 10.1088/0022-3727/41/23/234005.
- [139] T. M. P. Briels, J. Kos, G. J. J. Winands, E. M. van Veldhuizen, and U. Ebert, “Positive and negative streamers in ambient air: Measuring diameter, velocity and dissipated energy,” *Journal of Physics D: Applied Physics*, vol. 41, no. 23, p. 234004, Nov. 2008. DOI: 10.1088/0022-3727/41/23/234004.
- [140] A. Sun, J. Teunissen, and U. Ebert, “The inception of pulsed discharges in air: Simulations in background fields above and below breakdown,” *Journal of Physics D: Applied Physics*, vol. 47, no. 44, p. 445205, 2014.
- [141] D. Lamb and J. Verlinde, *Physics and chemistry of clouds*. Cambridge University Press, 2011.
- [142] R. F. Griffiths and J. Latham, “A new method for the measurement of the surface electrical conductivity of ice,” *Journal of the Meteorological Society of Japan. Ser. II*, vol. 52, no. 2, pp. 238–242, 1974. DOI: 10.2151/jmsj1965.52.2_238.
- [143] C. J. Rodger, “Red sprites, upward lightning, and vlf perturbations,” *Reviews of Geophysics*, vol. 37, no. 3, pp. 317–336, Aug. 1999. DOI: 10.1029/1999rg900006.

- [144] G. Milikh, J. Valdivia, and K. Papadopoulos, "Spectrum of red sprites," *Journal of Atmospheric and Solar-Terrestrial Physics*, vol. 60, no. 7-9, pp. 907–915, May 1998. DOI: 10.1016/S1364-6826(98)00032-7.
- [145] M. Stanley, P. Krehbiel, M. Brook, C. Moore, W. Rison, and B. Abrahams, "High speed video of initial sprite development," *Geophysical Research Letters*, vol. 26, no. 20, pp. 3201–3204, Oct. 1999. DOI: 10.1029/1999gl1010673.
- [146] S. A. Cummer, N. Jaugey, J. Li, W. A. Lyons, T. E. Nelson, and E. A. Gerken, "Submillisecond imaging of sprite development and structure," *Geophysical Research Letters*, vol. 33, no. 4, 2006. DOI: 10.1029/2005gl1024969.
- [147] J. Qin, S. Celestin, and V. P. Pasko, "Formation of single and double-headed streamers in sprite-halo events," *Geophysical Research Letters*, vol. 39, no. 5, n/a–n/a, Mar. 2012. DOI: 10.1029/2012gl1051088.
- [148] S. Nijdam, J. S. Moerman, T. M. P. Briels, E. M. van Veldhuizen, and U. Ebert, "Stereo-photography of streamers in air," *Applied Physics Letters*, vol. 92, no. 10, p. 101 502, Mar. 2008. DOI: 10.1063/1.2894195.
- [149] S. Nijdam, *Experimental investigations on the physics of streamers*. Eindhoven University of Technology, 2011.
- [150] P. F. Browne, "Mechanism of gas breakdown by lasers," *Proceedings of the Physical Society (1958-1967)*, vol. 86, no. 6, p. 1323, Dec. 1965. DOI: 10.1088/0370-1328/86/6/320.
- [151] M. Thiagarajan and S. Thompson, "Optical breakdown threshold investigation of 1064 nm laser induced air plasmas," *Journal of Applied Physics*, vol. 111, no. 7, p. 073 302, Apr. 2012. DOI: 10.1063/1.3699368.
- [152] T. X. Phuoc, "Laser spark ignition: Experimental determination of laser-induced breakdown thresholds of combustion gases," *Optics Communications*, vol. 175, no. 4, pp. 419–423, 2000, ISSN: 0030-4018. DOI: [https://doi.org/10.1016/S0030-4018\(00\)00488-0](https://doi.org/10.1016/S0030-4018(00)00488-0).
- [153] C. H. Chan, C. D. Moody, and W. B. McKnight, "Significant loss mechanisms in gas breakdown at 10.6 μ ," *Journal of Applied Physics*, vol. 44, no. 3, pp. 1179–1188, Mar. 1973. DOI: 10.1063/1.1662325.
- [154] S. Harilal and B. Harilal, "Diagnostics of laser induced spark in air using fast iccd photography," 2002.
- [155] C. Dumitrache and A. P. Yalin, "Gas dynamics and vorticity generation in laser-induced breakdown of air," *Opt. Express*, vol. 28, no. 4, pp. 5835–5850, Feb. 2020. DOI: 10.1364/OE.385430.
- [156] T. V. F., N. G. V., B. D. V., K. I. D., and B. N. Yu., "Formation of wide streamers during a subnanosecond discharge in atmospheric-pressure air," *Plasma Physics Reports*, vol. 44, pp. 746–753, 2018, ISSN: 1562-6938. DOI: <https://doi.org/10.1134/S1063780X18080081>.
- [157] L. Wantzel, "Classification des nombres incommensurables d'origine algébrique," fr, *Nouvelles annales de mathématiques : journal des candidats aux écoles polytechnique et normale*, vol. 1e série, 2, pp. 117–127, 1843.

Contributions of the author

This thesis presents the original work of the author. However, teamwork is key to solving complex research problems. Hence, besides the contributions of the supervisors, committee members, and co-authors, the more specific contributions of others to this thesis are as follows:

- Chapter 2: The Monte-Carlo simulation of which the results have been discussed in this chapter, has been developed by A. Martinez, a fellow PhD-student in the SAINT-project. In close contact with A. Martinez the simulation results were compared with experimental results performed by the author. The description of the model and the discussion of results from the simulations in these chapters is largely attributed to A. Martinez together with the author. The general discussion is primarily by the author.
- Chapter 4: The mathematical model of which the results have been discussed was established by S. Peeters, a bachelor student supervised by the author, in collaboration with the author. The implementation and data analysis both have been performed by S.Peeters and the author.
- Chapter 6: The setup preparation and experiments has been performed by W. Slot, an MSc-student working under the supervision of the author. The data analysis and discussions have been implemented by W. Slot and the author.

Acknowledgements

At the end of this thesis, I would like to take some time to thank all the people without whom this project would never have been possible. First of all, my deepest gratitude goes to my supervisor, Sander Nijdam, who guided me through all scientific and social challenges. I greatly appreciate the freedom you have given me to find my own path and the guidance and support you offered along the way. You allow me to do almost everything according to my interests and passions: from lab setup automation to 3D illustrations and animations to scientific grant writing! You gave me this incredible opportunity to develop a broad professional and local network in which I have learned how to initiate collaborations and launch my ideas. Without a doubt, this is the biggest achievement of my PhD life. Thank you, Sander, my wonderful supervisor. My next thanks go to Ute Ebert. Besides your excellent scientific knowledge, you are always able to catch tiny details that almost everyone else misses. Your mix of straightforward criticism combined with heartwarming support has given me great confidence as a researcher. My special thanks go to Jannis Teunissen. You are one of the most clever, quick, and precise researchers that I have ever met. Thanks for all of your help with my project.

I also want to take a moment to thank my other committee members, Prof. Dr. J. Dwyer, Prof. Dr. M. Fullekrug, Prof. Dr. R. Brandenburg, and Prof. Dr. G. Pemen. Thank you for investing time into my project and providing such valuable feedback. I feel proud and honored that you have agreed to be on my committee. A big part of my PhD research was done in close collaboration with Andy Martinez. I remember we had a dream of publishing a paper together in one month since both experimental and numerical setups were working perfectly. However, we both understand that, as always, great achievements are not made overnight, because of the scientific challenges it took one year to complete the mission. BUT this led to what I consider a bigger achievement than a published paper: friendship. I will never forget the days and nights we worked together, especially during August 2019, to find the answers to our questions or the ideas we explored together during our trips. Thanks, my friend Andy.

Immigration is always full of challenges and difficulties. And definitely, for a fresh expat, friends to help with acclimatizing are essential. For me this person was Samaneh Tadayon Mousavi. Thank you Samaneh for all your advice and help. I also have to mention Behnaz Bagheri gave me a lot of advice during my PhD and with whom I had really useful discussions.

And then, of course, my Eindhoven colleagues. First and foremost, Siebe Dijcks.

We have started together and you helped me with many scientific as well as social matters. We planned to discover the most unknown places on the Earth and develop streamer science in those places. I am sure we will do that together sometime in the near future. I should also thank my office mates: Zahra Marvi, Saman Hasani, Patrick Meijaard, Tim Staps, Boy van Minderhout, Dmitry Shefer, and Marlous Hofmans. Thank you all.

I would like to thank all the EPG, and also other, group members in the last four years who have helped me to see myself as a researcher in the group: Ana Sobota, Job Beckers, Jan van Dijk, Diana Mihailova, Eddie van Veldhuizen, Ab Schrader, Pieter Sanders, Ravi Pater, Anne Limburg, Chris Schoutrop, Jesper Janssen, Mark van der Schans, Bart Platier, Hans Dalderop, Siddarth Kumar, Tom Huiskamp, and Maxime Gendre. Moreover, special thanks to Anita Peeters who helped me a lot with arranging the administrative tasks.

And finally, I would like to express my deep gratitude to Gerrit Kroesen. During the two years that I have served on the Applied Physics PhD council, we had several heated discussions on the well-being of PhD students and I see you endeavoring to help PhD students to have a better work-life balance. I have learned a lot from you. Over the years I have supervised several students: Britt, Hiraui, Ramon, Rik, Denise, Wouter, Simone, and Silke. Thank you all for your collaboration. Silke, I am very impressed by the work you have done during your BEP project. You even worked during Sunday afternoons and wrote a paper by yourself, great job!

My PhD project was embedded in the SAINT network, for which I feel extremely fortunate. I had this opportunity to expand my network with international fellows and colleagues. Here, I should acknowledge Marcelo Arcanjo in particular. During my secondment at AirBus, I also received much help and support from Josh Phelps and Matt Webster.

Finally, I would like to thank all my friends, particularly my dear old friends Sara, Mozhgan and Bram. Without them, my time here would not nearly have been so enjoyable.

I would never have been able to finish my thesis without my beloved wife Neda. You are my foundation. Please hold my hand forever.

Shahriar Mirpour
September 2021

Curriculum Vitae

Shahriar Mirpour was born on 25/07/1989 in Tehran, Iran. After finishing pre-university education in 2008 at Soroush in Tehran, he studied Physics Engineering: Plasma Physics at Islamic Azad University: Science and Research Branch in Tehran, Iran. He received his Master of Science diploma in Plasma Engineering from Shahid Beheshti university in 2014. During his Bachelor's and Master's studies, he worked on the application of cold plasma on cancer and wound therapies. In 2015, he continued his research as Research Assistant in the Endocrinology and Metabolism Research Centre of Tehran University of Medical Sciences. Meanwhile, He founded a start-up (Hoopad Plasma Co.) on using cold plasma for diabetic foot ulcer treatment. This project raised many national and international grants and awards.

In 2017 he started a Marie Skłodowska-Curie PhD fellowship in the group of Elementary Processes in Gas Discharges in the applied physics department of Eindhoven university of Technology (TU/e). He completed a secondment at Airbus Co. on the feasibility study of a ground-based lightning damage assessment system for airborne vehicles. During his PhD study, he won two oral presentation awards on the topic that is presented in this dissertation. In 2019-2021 he was a member of the PhD council of the Department of Applied Physics at TU/e.

List of publications and awards

Publications (Submitted and Accepted)

- S. Mirpour and S. Nijdam. "Experimental investigation on streamer inception from artificial hydrometeors." To be submitted to Geophysical Research Letters
- S. Peeters, S. Mirpour, C. Kohn, and S. Nijdam. "A Model for Positive Corona Inception from Charged Ellipsoidal Thundercloud Hydrometeors." Submitted to Journal of Geophysical Research: Atmospheres, Under Review
- S. Mirpour and S. Nijdam. "Investigating CO₂ streamer inception in repetitive pulsed discharges." Submitted to Plasma Sources Science and Technology, Under Revision
- X. Zhang, Y. Guo, S. Mirpour, Y. Li, A. Sun, and S. Nijdam. "Effects of a negative corona discharge on subsequent positive streamers" Accepted by Journal of Physics D: Applied Physics.
- S. Mirpour, A. Martinez, J. Teunissen, U. Ebert, and S. Nijdam. "Distribution of inception times in repetitive pulsed discharges in synthetic air." Plasma Sources Science and Technology 29, no. 11 (2020): 115010.
- S. Mirpour, S. Fathollah, P. Mansouri, B. Larijani, M. Ghoranneviss, M.M. Tehrani, and M.R. Amini. "Cold atmospheric plasma as an effective method to treat diabetic foot ulcers: A randomized clinical trial." Scientific Reports (2020), 10(1), 1-9.
- M.R. Amini, M.S. Hosseini, S. Fatollah, S. Mirpour, M. Ghoranneviss, B. Larijani, and M.R. Khorramizadeh. "Beneficial effects of cold atmospheric plasma on inflammatory phase of diabetic foot ulcers; a randomized clinical trial." Journal of Diabetes & Metabolic Disorders (2020), 19(2), 895-905.
- S. Mirpour, S. Piroozmand, N. Soleimani, N.J. Fazarani, H. Ghomi, H.F. Eskandari, A.M. Sharifi, S. Mirpour, M. Eftekhari, and M. Nikkhah. "Utilizing the micron sized non-thermal atmospheric pressure plasma inside the animal body for the tumor treatment application." Scientific reports (2016), 6(1), pp.1-10.

- S. Fathollah, S. Mirpour, P. Mansouri, A.R. Dehpour, M. Ghoranneviss, N. Rahimi, Z.S. Naraghi, R. Chalangari, and K.M. Chalangari. "Investigation on the effects of the atmospheric pressure plasma on wound healing in diabetic rats." *Scientific reports* (2016), 6(1), pp.1-9.
- T. Zarei, S. Mirpour, H. Nikmaram, M. Ghoranneviss, S. Mirpour, and D. Dorrnian. "Softening hard water using high frequency spark plasma discharge." *Plasma Chemistry and Plasma Processing* (2017), 37(1), 99-114.
- S. Irani, Z. Shahmirani, S.M Atyabi, and S. Mirpour. "Induction of growth arrest in colorectal cancer cells by cold plasma and gold nanoparticles." *Archives of medical science: AMS* (2015), 11(6), p.1286.
- Z. Shahmirani, S. Irani, S.M. Atyabi, S. Mirpour, S. Shadpour, M. Ghorannevis, and M.D. Joupari. "Effect of cold atmospheric pressure plasma and gold nanoparticles on cell viability." *Annual Research & Review in Biology* (2014), 3108-3118.
- S. Mirpour, H. Ghomi, S. Piroozmand, M. Nikkhah, S.H. Tavassoli, and S.Z. Azad. "The selective characterization of nonthermal atmospheric pressure plasma jet on treatment of human breast cancer and normal cells." *IEEE Transactions on Plasma Science* (2014), 42(2), 315-322.

Awards

- Student prize for the best oral presentation at ICPIG XXXIV (2019)
- Best oral presentation at 31 NVV Plasma Symposium (2019)
- 3rd place for best research in diabetic intervention at JWC award (2019)
- JWC award - Best research from a developing country (2015)